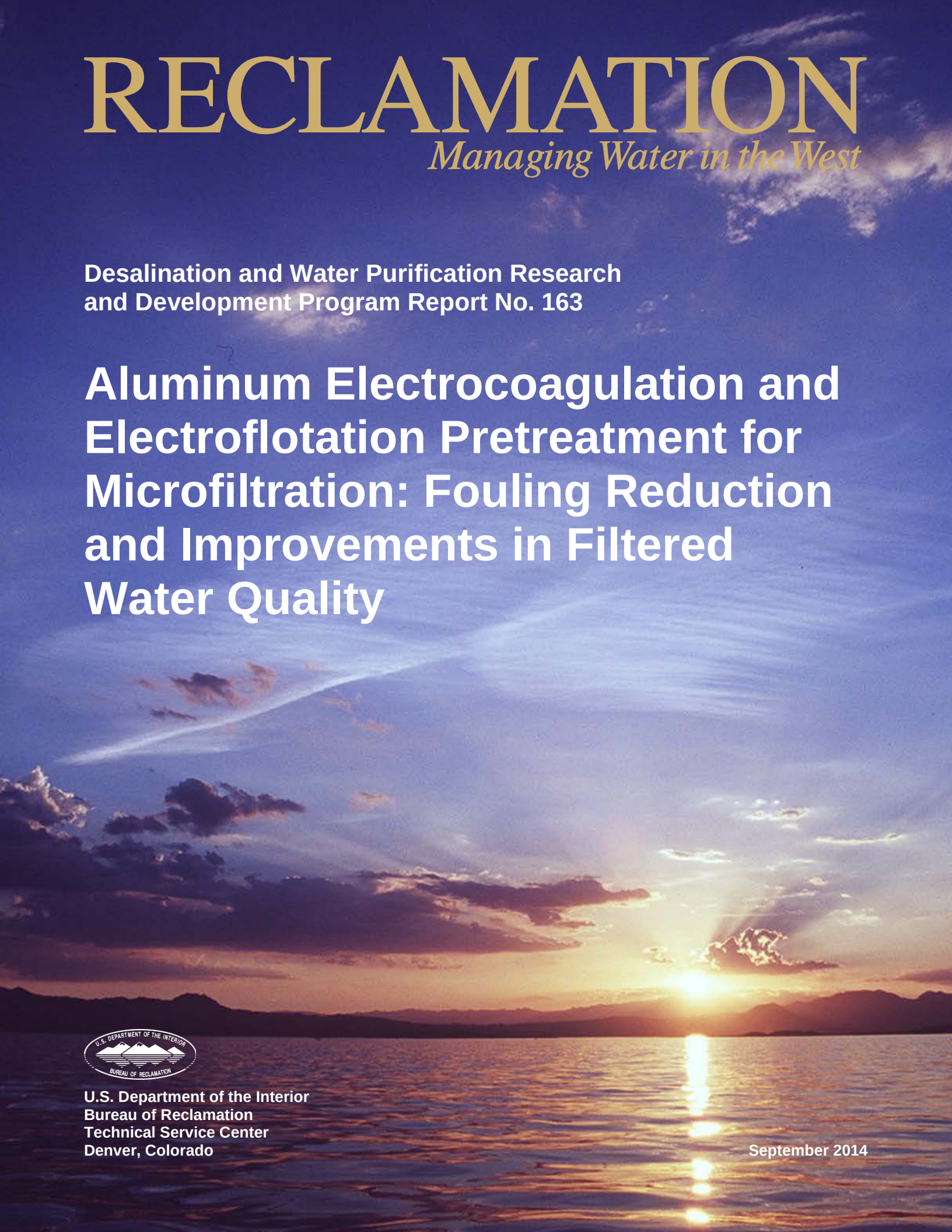

RECLAMATION

Managing Water in the West

Desalination and Water Purification Research and Development Program Report No. 163

Aluminum Electrocoagulation and Electroflotation Pretreatment for Microfiltration: Fouling Reduction and Improvements in Filtered Water Quality

U.S. Department of the Interior
Bureau of Reclamation
Technical Service Center
Denver, Colorado

September 2014

REPORT DOCUMENTATION PAGE

Form Approved
OMB No. 0704-0188

PLEASE DO NOT RETURN YOUR FORM TO THE ABOVE ADDRESS.

1. REPORT DATE *(DD-MM-YYYY)*	**2. REPORT TYPE**	**3. DATES COVERED** *(From - To)*
September 2014	Final	October 2010 – September 2014

4. TITLE AND SUBTITLE

Aluminum Electrocoagulation and Electroflotation Pretreatment for Microfiltration: Fouling Reduction and Improvements in Filtered Water Quality

5a. CONTRACT NUMBER

5b. GRANT NUMBER

5c. PROGRAM ELEMENT NUMBER

6. AUTHOR(S)

Shankar Chellam, Principal Investigator Neranga P. Gamage, Graduate Research Assistant Charan Tej Tanneru, Graduate Research Assistant Mutiara Ayu Sari, Graduate Research Assistant

5d. PROJECT NUMBER

5e. TASK NUMBER

5f. WORK UNIT NUMBER

7. PERFORMING ORGANIZATION NAME(S) AND ADDRESS(ES)

University of Houston
Department of Civil and Environmental Engineering
4800 Calhoun Road
Houston,, TX 77204-4003

8. PERFORMING ORGANIZATION REPORT NUMBER

9. SPONSORING/MONITORING AGENCY NAME(S) AND ADDRESS(ES)

Bureau of Reclamation
6th Avenue and Kipling Street
Building 67, Room 152
Denver, CO 80225
Tel: (303) 445-2248

10. SPONSOR/MONITOR'S ACRONYM(S)

Reclamation

11. SPONSOR/MONITOR'S REPORT NUMBER(S)

12. DISTRIBUTION/AVAILABILITY STATEMENT

13. SUPPLEMENTARY NOTES

Report can be downloaded from Reclamation Web site: https://www.usbr.gov/research/dwpr/DWPR_Reports.html

14. ABSTRACT

Aluminum electrocoagulation and electroflotation pretreatment of surface water from Lake Houston significantly alleviated microfiltration (MF) membrane fouling in bench-scale experiments. Electrochemical aluminum production quantitatively obeyed Faraday's law with a 3-electron transfer at nearly 100% efficiency resulting in precipitation of predominantly amorphous $Al(OH)_3$. Enmeshment of colloids in amorphous precipitates (sweep flocculation) was the predominant colloid destabilization mechanism with secondary contributions from adsorption and charge neutralization. Fouling of a commercially available polymeric microfilter following electrocoagulation pretreatment was found to (i) be lower at pH 6.4 compared with 7.5, (ii) decrease only up to an intermediate aluminum dosage, and (iii) exacerbate with increasing transmembrane pressure. Cathodic evolution of hydrogen bubbles over relatively long durations was empirically observed to induce floc flotation. Electroflotation was also employed for MF pretreatment by skimming off the surficial floc layer and drawing water from near the bottom of the electroflotation cell. This approach significantly increased MF permeate flux reducing both the cake mass and the cumulative hydraulic resistance. Nanofilter flux decline was best controlled by combined pretreatment using electroflotation – MF. Also, viruses were effectively removed by electrochemical treatment with insignificant inactivation. Sweep flocculation was the primary virus destabilization mechanism. Highly encouraging laboratory-scale results point to the need for larger-scale evaluations of a hybrid electrofiltration/electrocoagulation-MF process for drinking water treatment.

15. SUBJECT TERMS

Electrocoagulation, Electroflotation, Pretreatment, Microfiltration, Fouling, Virus removal, Surface water treatment

16. SECURITY CLASSIFICATION OF:			**17. LIMITATION OF ABSTRACT**	**18. NUMBER OF PAGES**	**19a. NAME OF RESPONSIBLE PERSON**
a. REPORT	**b. ABSTRACT**	**a. THIS PAGE**			Saied Delagah
U	U	U	SAR		**19b. TELEPHONE NUMBER** *(Include area code)* 303-445-2248

Desalination and Water Purification Research and Development Program Report No. 163

Aluminum Electrocoagulation and Electroflotation Pretreatment for Microfiltration: Fouling Reduction and Improvements in Filtered Water Quality

Prepared for the Bureau of Reclamation Under Agreement No. R10AP81218

by

Shankar Chellam, Principal Investigator
Neranga P. Gamage, Graduate Research Assistant
Charan Tej Tanneru, Graduate Research Assistant
Mutiara Ayu Sari, Graduate Research Assistant

Department of Civil and Environmental Engineering
University of Houston
Houston, TX 77204-4003

U.S. Department of the Interior
Bureau of Reclamation
Technical Service Center
Denver, Colorado

September 2014

MISSION STATEMENTS

The U.S. Department of the Interior protects America's natural resources and heritage, honors our cultures and tribal communities, and supplies the energy to power our future.

The mission of the Bureau of Reclamation is to manage, develop, and protect water and related resources in an environmentally and economically sound manner in the interest of the American public.

Disclaimer

The views, analysis, recommendations, and conclusions in this report are those of the authors and do not represent official or unofficial policies or opinions of the United States Government, and the United States takes no position with regard to any findings, conclusions, or recommendations made. As such, mention of trade names or commercial products does not constitute their endorsement by the United States Government.

Acknowledgments

The research reported herein was made possible by grants from the U.S. Bureau of Reclamation's Desalination and Water Purification Research and Development Program (Cooperative Agreement No. R10AP81218), the National Science Foundation (CBET-0966939), and the Texas Hazardous Waste Research Center. The contents do not necessarily reflect the views and policies of the sponsors nor does the mention of trade names or commercial products constitute endorsement or recommendation for use. The authors wish to express their appreciation for the advice and assistance of Mr. Saied Delagah, Dr. Katharine Dahm, Mr. Frank Leitz, and Ms. Yuliana Porras-Mendoza from the Bureau of Reclamation. We are grateful to Dr. Ying Wei and her staff at the City of Houston's East Water Purification Plant for facilitating sampling and water quality analyses. Will Payne assisted with the conduct of nanofiltration experiments. Peter Eriksson of GE Power & Water generously donated nanofiltration membrane samples.

CONTENTS

Figures

Page

Tables

Page

ACRONYMS AND ABBREVIATIONS

AFM	atomic force microscopy
ATR	attenuated total reflectance (sampling technique used with FTIR)
COD	chemical oxygen demand
DOC	dissolved organic carbon
FTIR	Fourier transform infrared spectroscopy
FWHM	full width at half-maximum (pertains to a spectrum curve)
hkℓ	Miller indices (in crystallography)
MF	microfiltration
n	compressibility index
NF	nanofiltration
NOM	natural organic matter
NTU	nephelometric turbidity units
PFU	plaque-forming units
PVDF	polyvinylidene fluoride
ROS	reactive oxygen species
SUVA	specific UV absorbance (absorbance at 254 nm for a 1-m path length divided by the DOC concentration expressed in mg/L)
UF	ultrafiltration
UV	ultraviolet light
UV_{254}	absorbance of ultraviolet light with a wavelength of 254 nm
XPS	X-ray photoelectron spectroscopy
XRD	X-ray diffraction

α^*	specific resistance of cakes
α_0^*	specific resistance at null pressure
ΔP	transmembrane pressure

METRIC CONVERSIONS

The metric equivalents for non-metric units used in the text are as follows:

Unit	Metric equivalent
1 *g* (gravitational force)	9.8 meters per second per second
1 gallon	3.8 liters
1 torr	133.3 pascals

EXECUTIVE SUMMARY

This report summarizes our findings related to surface water purification, specifically regarding:

1. Electrocoagulation and electroflotation pretreatment to reduce microfiltration (MF) membrane fouling,
2. Combining electrochemical treatment and MF for nanofiltration (NF) membrane pretreatment, and
3. Combining electrochemical treatment and MF to control viruses.

Bench-scale experiments were performed to evaluate aluminum electrochemical pretreatment for dead-end, constant-pressure MF of water from Lake Houston, Texas. Electrochemical aluminum production quantitatively obeyed Faraday's law, with a three-electron transfer at nearly 100 percent efficiency, resulting in amorphous $Al(OH)_3$ precipitation. Enmeshment of colloids (sweep flocculation) was the predominant destabilization mechanism with secondary contributions from adsorption and charge neutralization. Following electrocoagulation pretreatment of a commercially available poly(vinylidene fluoride) MF membrane, fouling was found to (i) be lower at pH 6.4 than at 7.5, (ii) decrease only at relatively low aluminum dosages, and (iii) be exacerbated with increasing transmembrane pressure. Cathodic evolution of hydrogen bubbles over relatively long durations induced floc flotation. Electroflotation was employed for MF pretreatment by skimming off the surficial floc layer and drawing water from near the bottom of the cell. This approach significantly increased MF permeate flux. Electroflotation pretreatment formed largely reversible fouling layers that may lead to more effective MF backwashing.

We also evaluated the capability of four different advanced pretreatment processes (viz. MF alone, chemical (alum) coagulation with MF, electro-coagulation with MF, and electroflotation with MF) to reduce fouling of a commercially available thin-film composite NF membrane during surface water treatment. It was empirically determined that the decline of NF productivity was best controlled by electroflotation with MF. Attenuated total reflection–Fourier transform infrared spectroscopy and X-ray photoelectron spectroscopy revealed polysaccharides and proteins as major NF foulants. Coagulation induced subtle differences in protein foulants in terms of their secondary structures, as inferred from second derivative analysis of the amide I band. For example, coagulation decreased intramolecular β structures and α helices but increased 3_{10} helices and unordered structures, indicating conformational changes of protein foulants with pretreatment type. Alcian Blue staining established the presence of acidic polysaccharides in the NF fouling layer. Similar air-water contact angles for virgin and fouled nanofilters provided further evidence that foulants were predominantly hydrophilic in nature. Fouling caused only a slight increase in surface roughness, suggesting that natural organic matter complexation with

divalent cations was relatively insignificant, leading to the deposition of a thin foulant layer. Statistically similar root-mean-squared surface roughness of fouled nanofilters suggested negligible effect of pretreatment type on foulant layer morphology.

Aluminum electrocoagulation and electroflotation removed viruses more effectively than conventional alum coagulation. Viruses were sweep flocculated during electrochemical treatment of surface water, implying that measured reductions were solely due to their removal (not inactivation).

BACKGROUND AND INTRODUCTION

The greater Houston, Texas, area is one of the fastest growing regions in the United States, increasing in population by 25 percent between 1990 and 2000 and is estimated to grow by another 45 percent by the year 2030. More water purification facilities are being designed and built to meet the increasing demands of the growing population. Of particular importance to the process of planning new drinking water treatment plants is that over 12,000 km^2 of land in and around the City of Houston has subsided more than 0.5 feet, with some areas subsiding more than 10 feet primarily due to excessive groundwater extraction. Subsidence-induced lowering of the land surface elevation has increased the frequency and severity of flooding; damaged the infrastructure, including industrial and residential buildings as well as roads and bridges; and reduced coverage of sensitive wetland ecosystems and marshes [1]. To mitigate these adverse effects, the City of Houston has been ordered to meet its entire water demand using only surface water supplies by the year 2030.

Microfiltration (MF) is an attractive choice for purifying surface waters largely because it is capable of removing large quantities of protozoa, including *Giardia*, *Cryptosporidium*, bacteria, and other microbial indicators. Hydrolyzing metal salts such as ferric chloride or aluminum sulfate are often added to feed waters to reduce microfilter fouling and improve filtered water quality [2–4]. Electro-coagulation is an attractive alternative to conventional chemical coagulation since it (i) reduces the direct handling of corrosive chemicals, (ii) does not significantly consume the natural buffering capacity (alkalinity) of the water, (iii) is thought to produce lower amounts of sludge, (iv) can be highly automated to reduce labor costs, and (v) is compact and skid-mountable and therefore can be easily employed in portable water purification units [5–9].

Electrocoagulation is the application of electricity to induce in situ electrolytic dissolution of a metal ion coagulant from a sacrificial anode. Typically aluminum or iron is chosen similar to conventional chemical coagulation. These cations undergo hydrolysis to form a variety of products that can adsorb onto colloids to neutralize their surface charge. Precipitation of hydroxide also occurs, which is capable of sweep flocculation. Note that in situ dissolution differs from

conventional chemical coagulation, in which salts such as aluminum sulfate (alum) or ferric sulfate are externally added to the water stream. Electrocoagulation has been shown to be successful for the removal of organic compounds [10, 11], heavy metals [12, 13], anions [14, 15], microorganisms [16], turbidity [17], and other physical, inorganic, and organic contaminants [5, 9, 11, 18] from municipal and industrial wastewaters and from contaminated drinking water supplies. Electrocoagulation alone has also been shown to be effective in removing oil and grease, chemical oxygen demand (COD), dyes, heavy metals, turbidity, and bacteria from drinking water and wastewaters [8, 19–25]. Electrocoagulation has also been combined with microfiltration and shown to be highly effective for synthetic waters, achieving ~ 90 percent energy savings, ~ 99 percent removals of heavy metals (Se, Pb, Zn, Cu, Cd, and As) and > 99.999 percent removal of viruses [16, 26, 27].

In some cases, hydrogen gas evolution at the cathode induces floc-flotation, especially for higher current passage times [28, 29]. This is termed electroflotation if the electrochemically treated water is drained from the bottom for downstream purification. By only filtering the particles remaining in the water column (by skimming off the floating colloids), the mass concentration of foulants is substantially reduced. Hence, in addition to enhancing filtered water quality, electrocoagulation and electroflotation pretreatment can also reduce membrane fouling, making an integrated electrochemical-MF process particularly attractive for small drinking water treatment plants [29, 30]. However, its suitability for MF pretreatment is just beginning to be evaluated [30–33].

The generation of soluble ferrous ions and the accumulation of colloidal precipitates on electrodes suggests some disadvantages of iron electrocoagulation pretreatment for MF and ultrafiltration (UF) of industrial, surface, and saline waters [26, 30–32]. Therefore, it was hypothesized that electrocoagulation performance would be improved using the other common metal-ion coagulant, namely aluminum. Limited data available from synthetic water experiments generated by other researchers suggest that substantial energy conservation is possible from aluminum electrocoagulation pretreatment to dead-end MF [33].

When the entire electrolyzed suspension is directly filtered (without intermediate solids removal) the process is referred to as electrocoagulation (or electroflocculation) [9, 33]. It is emphasized that any kind of coagulation pretreatment increases the mass loading on the membrane over what it would be with untreated raw water (because of coagulant precipitation). Along with anodic dissolution of the electrocoagulant, hydrogen bubbles are released from the cathode due to water splitting [5, 9, 34, 35]. Gas evolution during electrochemical treatment of industrial and metallurgical feed waters and wastewaters leads to a type of floc flotation that has also been termed electroflotation [9, 25, 36]. We have also reported floc flotation for longer duration of current passage and associated higher electrocoagulant concentrations during electrolysis of municipal drinking water supplies [37]. The floating layer can be easily skimmed off the top without adding

a separate step in the treatment train. In other words, electroflotation reduces the colloid concentration fed to any downstream process without increasing the treatment train's complexity, footprint, or cost. We therefore hypothesized that it would be feasible to use electroflotation pretreatment to reduce fouling in a hybrid electroflotation-MF process by decreasing the solids concentration in the MF feed water.

Another important aspect of this research is that we have considered irreversible fouling when MF membranes are backwashed. Since physical regeneration methods such as backwashing are only partially effective in controlling fouling, colloids and natural organic matter (NOM) present in the source water are sometimes also coagulated prior to MF/UF to better maintain productivity [38, 39]. Past research has largely focused on optimizing conventional coagulation conditions to best control short-term fouling during forward filtration [40–43] over and above what is possible by backwashing alone, by reducing pore penetration and increasing cake permeability. This report describes improvements in backwashing after electrochemical pretreatment. Since electroflotation pretreatment removes a portion of NOM and silica and significantly improves short-term MF flux [44], we hypothesized that it will also successfully combat irreversible fouling over extended timeframes. In general, operationally observed fouling is typically linked to adsorption of NOM [38, 45–48] or its specific components, including protein-like, carbohydrate-like, and humic substances [49, 50], and to adsorption of inorganic constituents such as silicon, iron, and aluminum [47, 50]. More detailed information on the dynamics of foulant accumulation will aid in understanding MF flux decline mechanisms.

During the course of this project, we also investigated the chemical basis of cake compression. Real-world MF/UF systems are operated at constant flux by increasing pressure to compensate for fouling [51–53]. Increasing pressure to maintain design flux as filtration progresses compresses cakes, further exacerbating fouling [52, 54]. Paradoxically, although such cake compaction is an important aspect of membrane fouling, only limited information is available on its underlying physicochemical mechanisms. Previous research has largely focused on developing empirical constitutive equations relating permeability, specific hydraulic resistance, and porosity of cakes as a function of pressure [55–57]. Filter cake permeabilities have also been related to the size and morphology of influent particles [58–60], with more compact and smaller colloids typically forming more resistant cakes. We hypothesized that in addition to the previously reported physical factors, the chemical composition of colloids and flocs in natural and coagulated waters, along with their associated specific interparticle interactions, also influences cake compression. Additionally, earlier research has mainly considered idealized systems containing model colloids (e.g. hematite, kaolin, or latex) and single NOM fractions (e.g. humic acids) suspended in ultrapure water of predetermined solution chemistry [58–63]. In this manuscript, we report results for natural water from Lake Houston, Texas, which is a source of drinking water for the City of Houston. Additionally, to our knowledge, this is

the first detailed investigation of compressibility mechanisms for electro-coagulated suspensions.

The specific resistance of cakes (α*) typically increases in a power-law fashion with increasing pressure (ΔP) [53, 54, 57–59, 64]:

$$\alpha^* = \alpha_0^* \Delta P^n \quad (1)$$

where α_0^* denotes the specific resistance at null pressure, which depends on the macroscopic morphology of the overall cake (including individual particle/ aggregate size, shape, and porosity) laid down at an asymptotically low pressure. The compressibility index *n* quantifies changes in hydraulic resistance with ΔP and depends on elastic particle deformation and reorganization following aggregate breakage (inelastic compression).

In addition to microfiltration, we also employed electrochemical treatment for nanofiltration (NF) pretreatment. NF can be implemented for removing divalent ions such as calcium and magnesium (hardness), macromolecules such as NOM and disinfection byproduct precursors, as well as aggregate and trace contaminants such as color, pesticides, and pharmaceuticals and personal care products from surface waters and shallow groundwaters [65–67]. However, in contrast to groundwater, these feed waters rapidly foul nanofilters, necessitating advanced pretreatment such as microfiltration (MF) [68–70]. Since MF alone does not remove significant amounts of NOM, it primarily only reduces colloidal fouling of downstream NF membranes in these applications. Therefore, we hypothesized that incorporating additional MF pretreatment capable of removing NOM (e.g., coagulation) will enhance NF specific fluxes in integrated membrane systems by simultaneously reducing both organic and colloidal fouling. Note that coagulation pretreatment to MF will provide the supplementary benefit of reducing MF fouling as well [71]. There is increasing interest in electrochemical coagulation due to its ability to reduce the handling of corrosive chemicals and to improve performance e.g. [9, 72]. For this reason, we evaluated both conventional chemical coagulation and electrocoagulation methods.

Detailed reports of NF foulants in dual membrane systems are available for wastewater reclamation and surface water treatment [73–76]. It is emphasized that due to the inherent heterogeneity of water supplies, additional information from geographically diverse sources would aid in the better design and implementation of integrated surface-water NF systems. Our interests in this topic arise from the mandate for the greater Houston area to completely convert to surface water by the year 2030 to combat ground subsidence while meeting the demands associated with the projected 45 percent growth in population over the same timeframe.

In addition to studying the potential of electrochemical treatment for microfilter and nanofilter fouling control, we also evaluated its ability to control viruses. Disinfection of contaminated waters to reduce enteric diseases continues to be one

of the most important aspects of drinking water purification [77]. Enteric viruses have been identified as causative agents for over 40 percent of childhood diarrhea in developing countries [78]. It has also been suggested that viruses are the etiologic agents responsible for the majority of unidentified outbreaks since they are typically more difficult to analyze than bacterial pathogens [79]. While microfiltration alone is highly efficient for the control of pathogenic protozoa and bacteria, it is not well-suited for removing viruses since they are substantially smaller than membrane pore sizes [80–84]. Although sorption onto microfilters can transiently increase virus removal [82, 85], hydrophobic, electrostatic, and other nonspecific interactions leading to their attachment onto the membrane material cannot reliably remove viruses during water purification, especially during long-term (pseudo-steady-state) operation. However, virus removal by microfiltration can be significantly improved by chemical coagulation pretreatment, with several studies demonstrating >99.99 percent or 4-log removals (as required under the Surface Water Treatment Rule) using alum or iron salts [e.g. 16, 86–88]. Alternately, electrocoagulation can also be employed for MF and UF pretreatment.

Iron electrocoagulation appears to be less promising for pretreating natural waters prior to low-pressure membrane filtration, inasmuch as chemical coagulation with $FeCl_3$ has consistently outperformed it. For example, during both UF of seawater [30] and MF of lake water [32], significantly greater fluxes were obtained following conventional chemical coagulation than were achieved following iron electrocoagulation. These are in contrast to more promising results reported using electrocoagulation for model waters devoid of NOM. Hence, it appears that experiments using synthetic waters cannot be directly used to extrapolate and predict electrocoagulation system performance for fouling control under real-world conditions. Therefore, we explicitly studied whether the excellent (>5-log) removal of viruses measured from waters devoid of NOM by iron electro-coagulation and subsequent microfiltration [16] could be extended to surface water containing NOM.

The icosahedral F-specific ssRNA coliphage MS2 was employed to facilitate comparisons with earlier results of virus removals by low-pressure membranes [e.g. 16, 81, 83, 85, 87, 88]. Its small size (approx. 30 nm) and low isoelectric point (3.9) reduce steric interactions and adsorption, allowing a conservative estimate of virus removal by microfilters. Further, it has been shown to be a conservative surrogate for the treatability of human viruses such as coxsackievirus and echovirus by coagulation [89]. Since MS2 specifically infects the gastrointestinal bacterium *Escherichia coli*, it also captures similarities of origin and release of human enteric viruses into the aquatic environment. Additionally, being similar in size, shape, and nucleic acid composition to the hepatitis A and polio viruses, MS2 is an excellent surrogate for pathogenic human enteric viruses [89–91]. Finally, bacteriophages facilitate experimentation since they are not hazardous to humans, avoid the need for animal cell lines, and are relatively easy to cultivate and dispose of.

Viruses are poorly removed by MF alone in the absence of any pretreatment [16, 82, 92–94], whereas alum coagulation followed by media filtration removes 2–4 log of influent viruses [95, 96], and enhanced coagulation with $FeCl_3$ has been shown to remove 1.75–3.0 log of animal viruses [97, 98]. These examples suggest virus removals by MF can also be increased by incorporating coagulation pretreatment. Indeed, using aluminum and iron coagulation prior to MF has been shown to remove >4-log of viruses from the feed water [16, 92, 93]. In contrast to the substantial database documenting removal of NOM and disinfection-byproduct precursors by coagulation, much less information is available on its ability to control viruses. It is noted that previous work on this topic has largely focused on optimizing coagulation conditions to maximize virus removals and to evaluate bacteriophage surrogates for human viruses rather than rigorously elucidating virus destabilization mechanisms. To date, there is very limited information available on the ability of electrocoagulation and electroflotation to remove and inactivate viruses.

CONCLUSIONS AND IMPLICATIONS

Switching the electrocoagulant from iron [32] to aluminum reduced fouling substantially, suggesting the potential suitability of aluminum electrochemical treatment for water and wastewater treatment. Inasmuch as our results are based on short-term bench-scale experiments, larger scale long-term testing at site-specific conditions is recommended before the suitability for electrocoagulation for full-scale applications can be conclusively established. In the range of experimental conditions investigated, a combination of lower pH, low pressure, and intermediate aluminum concentrations was optimal for fouling mitigation during an electrocoagulation-MF process. Fouling was reduced most for an aluminum dosage corresponding to the lowest *cumulative* cake resistance. At this dosage the conflicting effects of creating larger flocs (lower *specific* resistance) and adding more mass of foulants (higher *total* resistance) were balanced. Cake compaction increased fouling with pressure, suggesting the merits of constant-pressure operation over constant-flux mode, as is currently practiced in full-scale MF systems.

Only short-range order was discerned in X-ray diffraction patterns, demonstrating precipitation of amorphous $Al(OH)_3$ during electrocoagulation. Oxide film formation on the electrode and its subsequent corrosion is an important issue related to electrocoagulation [12]. To date, this issue can only be evaluated through site-specific long-term tests. Electrode passivation, pitting, and chemical dissolution have been implicated as causing variations in aluminum generation efficiency ranging from about 100 percent to even more than 200 percent [12, 14, 15, 19, 229]. Since the kinetics of these phenomena cannot be theoretically predicted for natural waters, empirical evaluation of the electrocoagulation-MF process is strongly recommended. It is again emphasized that bench-scale results

summarized herein need to be verified at a larger scale to obtain engineering design parameters.

Hydrogen bubbles released from the cathode (and in some cases oxygen evolution from water splitting at high anode potential) could potentially influence the floc morphology and induce flotation [10, 230]. We observed partial flotation of flocs for certain experiments, which we empirically hypothesize will become more evident at higher current densities or current passage times (corresponding to higher aluminum concentrations and longer durations of bubble formation). More work is needed to determine the conditions that stimulate electroflotation and to optimize it for MF pretreatment by skimming off the flotsam, similar to the procedure used with dissolved air flotation pretreatment for MF [231].

Substantial floc flotation occurred when electrolysis was performed for long durations (resulting in high aluminum dosages). A significant advantage of electroflotation is intermediate floc removal (without adding a separate step in the treatment train), which reduces the concentration of colloids in the water column to be removed by microfiltration. Microfiltration of pretreated waters with lower concentrations of colloids and NOM following electroflotation improved fluxes to a greater extent than electrocoagulation. Unlike chemical and electrocoagulation pretreatment, MF fluxes did not continue to decline progressively with Al overdosing in this process. This suggests the possibility of easier process control in an electroflotation-MF process. Additionally, the range of minimum aluminum solubility (~pH 6.4) coincides with the pH range for release of a large number of smaller hydrogen bubbles, which aids in flotation by increasing attachment frequency. Further, colloids in MF feed waters after electroflotation were largely reversibly bound to membrane surfaces, whereas some irreversible fouling was measured in electrocoagulation. This suggests comparatively greater MF backwashing efficiencies for electroflotation pretreatment. These characteristics make electroflotation highly suitable for low-pressure membrane pretreatment during municipal drinking water purification. It should be emphasized that more work is necessary to scale up these relatively short-term bench-scale observations to pilot scale and full scale before recommendations can be made for real-world systems.

Hydrophobic molecules primarily appeared to initiate fouling during microfiltration of untreated raw water, as infrared spectra of membrane surfaces showed that O–H and N–H bands attenuated while C–H bands remained relatively unchanged after only one filtration cycle. However, O–H, N–H, and symmetric and asymmetric $C(=O)O^-$ stretching bands significantly intensified with continued filtration/regeneration of untreated water, showing the importance of hydrophilic molecules and the role of complexation, respectively, in contributing to longer term irreversible fouling. Distinct C–H bands were detected in floated flocs after electrolysis, suggesting the sorption and subsequent removal of a substantial portion of the hydrophobic moieties present in Lake Houston water during pretreatment. Consequently, hydrophilic compounds appeared to

contribute more to irreversible fouling in pretreated waters throughout the course of filtration, as evidenced by significantly more intense O–H bands (compared to C–H bands) on the membrane surface after cycles 1 and 5. Therefore, electroflotation pretreatment reduced the accumulation of hydrophobic foulants but simultaneously increased complexation of hydrophilic foulant molecules along with any carried-over aluminum hydroxide precipitates, evidenced by the increasing Al and O concentrations detected via X-ray photoelectron spectroscopy (XPS) and by the intense $C(=O)O^-$ stretching bands in IR spectra.

Increased fouling at higher transmembrane pressures (manifested as more rapid decline of the instantaneous flux normalized by the initial flux) was attributed to cake compressibility. Electrocoagulated aggregates were similar in size to alum-coagulated flocs but more porous and branched, consistent with the incorporation of electrolytically generated hydrogen bubbles. Reduced specific resistances of the electrochemically aggregated flocs at null pressure were attributed to their lower mass fractal dimensions, which would have increased intra-floc porosity. X-ray diffractometry and electron microscopy revealed that both electro-coagulation and alum coagulation generated amorphous and gelatinous $Al(OH)_3$ flocs, which contributed marginally to elastic cake compression. Differences in the chemical state and functionalities of substances taken up by flocs generated via electrolysis and alum addition were measured using high-resolution X-ray photoelectron spectroscopy. Compared with alum coagulation, electrocoagulated flocs preferentially accumulated hydrophobic compounds with reduced uptake of moieties containing amides and carboxyl groups. Consequently, relatively weak hydrophobic interactions would have dominated the highly branched electrocoagulated flocs, making them more fragile. This hydrophobicity increased inelastic contributions to their compaction at higher pressures, arising from aggregate breakage and redistribution of fines. In contrast, greater uptake of polar compounds by alum coagulation would have induced stronger interparticle interactions, such as hydrogen bonding and complexation. These interactions, coupled to their compact morphology, would have reduced their inelastic compression. Therefore, aggregate morphology and specific interparticle interactions provided the mechanistic bases of variation in cake compressibility indices in the order electrocoagulation > alum coagulation > untreated water.

During MF of untreated surface water, irreversible fouling of a modified polyvinylidene fluoride (PVDF) membrane was largely initiated by hydrophobic molecules. Over multiple filtration/regeneration cycles, hydrophilic molecules progressively accumulated as the membrane became progressively more coated with foulants. Irreversible fouling by carbohydrate-like, protein-like, and siliceous compounds was illustrated by their long-term accumulation even after repeated physical regeneration. Electroflotation pretreatment controlled fouling by:

(i) Partitioning a fraction of NOM and siliceous compounds to the electro-coagulant, thereby reducing direct foulant interactions with the membrane;

(ii) Floc flotation, which prevents a significant fraction of coagulant-bound foulants from reaching the membrane surface [44], even though it significantly increased aluminum accumulation; and

(iii) Forming large aggregates, which decrease pore penetration [44].

Electroflotation reduced the concentration of hydrophobic molecules in the feed water but added $Al(OH)_3$, causing polar molecules to contribute strongly to irreversible fouling over all time scales after pretreatment. Polyvalent aluminum coagulant species can bridge, chelate, or electrovalently complex foulants to membranes. This activity explains why coagulation pretreatment sometimes even increases fouling [3, 102] or has only a limited effect [232], and it shows the importance of monitoring aluminum and iron [48] concentrations in source or feed waters.

Foulants can also participate in hydrogen bonding [233, 234] and hydrophobic interactions [235] with polymeric MF membranes. In addition to fingerprinting foulants [46, 47, 50, 143, 236–238] Fourier transform infrared spectroscopy (FTIR) and XPS provide clues to the nature of these chemical interactions since they are highly sensitive to perturbations in localized atomic environments that cause spectral peaks to shift, broaden, and change in intensity [152, 239, 240]. We observed numerous peak shifts of C–H, O–H, and N–H stretching vibrations and in the amide I region, indicating compositional changes as well as chemical interactions between membrane surfaces and foulant molecules. For example, in membranes fouled by untreated raw water, as compared to the virgin membrane, the C–H stretching bands blue-shifted toward higher wave numbers (3022→3025 cm^{-1} and 2980→2984 cm^{-1}), as seen in Figure 24 (presented later in the report). This shift has been attributed to hydrophobic interactions of C–H groups with nearby polar moieties such as O–H groups [241]. Additionally, for membranes fouled by raw and pretreated waters the OH and NH bands showed red shifts toward lower wave numbers, compared to both virgin membrane (3715–2600→3700–2625 cm^{-1}) and raw water (3750–2610→3700–2625 cm^{-1}), as seen in Figure 24. This change can be attributed to hydrogen bonding of O–H groups with polar moieties such as OH, C=O, and N–H [242].

Further, the amide I band in membranes filtering raw water after five cycles red-shifted compared with its position in the feed water (1654→1650 cm^{-1} and 1640→1638 cm^{-1}), as seen in Figure 25 (presented later in the report). This shift can possibly arise from hydrogen bonding of proteinaceous compounds, which lengthens peptide C=O bonds and thereby reduces their vibrational frequency [241]. Multiple interaction modes can strengthen foulant attachment and can magnify the extent of physically irreversible fouling. Such interactions will depend on the NOM molecular weight (i.e. segment chain length) and functionalities, solution chemistry, and the membrane surface composition. These variables partially explain differences in fouling with source water origin, pretreatment, and membrane material [45, 47, 71]. Although this study provides clues to chemical bonding mechanisms between foulants and membrane surfaces,

individual interfacial interactions during natural water MF could not be resolved due to severe peak overlap in IR spectra. We are currently undertaking high-resolution XPS to better resolve hydrogen bonding and hydrophobic interactions that led to foulant accumulation and flux decline during drinking water MF.

Cake compression appears to be an important mechanism during MF of (electro-) coagulated natural water since classical filtration theory quantitatively fit experimental data at any given pressure and since flocs are inherently very fragile [243]. Deconvolution of high-resolution C1s spectra revealed strong C-C/C-H peaks that contributed the highest to both electrocoagulated (52%) and alum-coagulated (43%) flocs (Figure 32; presented later in the report), demonstrating excellent uptake of hydrophobic NOM moieties, as reported earlier [147, 244, 245]. Complementarily, amides, carbonyls, and carboxyl were more abundant on alum flocs (57%) than in electrocoagulation (48%). Amides are strong hydrogen-bond donators/acceptors [246–248], acidic organic moieties facilitate complexation (e.g., bridging) [133, 135, 156], and hydrocarbon backbones mediate hydrophobic interactions [175]. Inasmuch as hydrogen bonding and complexation are stronger than hydrophobic interactions [249], alum-coagulated flocs can be expected to be more cohesive, exhibiting reduced inelastic compression. Analogously, lower concentrations of polar groups and higher concentrations of hydrophobic NOM on electrocoagulated precipitates suggest that they were subjected to weaker interparticle forces, allowing them to more easily rupture at higher pressures. Inelastic compaction would explain cake stratification during MF of coagulated suspensions [55, 250, 251]. It also provides the mechanistic basis for the very high fouling rates during constant-flux MF [51, 52, 54], since increasing pressure to maintain productivity further compresses the cake, which accelerates the rate of fouling and results in experimentally observed concave-upward or runaway pressure profiles [54].

Ineffective virus control from surface water with iron electrocoagulation pretreatment for microfiltration is attributed to NOM complexation of electro-chemically generated Fe(II), which interferes with sweep flocculation, with charge neutralization, and with ROS (reactive oxygen species)-mediated inactivation. Floc flotation was observed at higher electrocoagulant dosages due to the cathodic release of hydrogen gas. It is noted that aluminum, the other common metal-ion coagulant, exists predominantly in the insoluble trivalent oxidation state (unlike a transition metal such as iron that exists in soluble and insoluble forms). Hence, current experiments are focused on evaluating aluminum for electrocoagulation and electroflotation pretreatment of natural water before microfiltration.

When iron was employed as the electrocoagulant, significantly better virus reductions were measured in the absence of NOM than in surface water containing moderate NOM concentrations. Importantly, mechanisms of virus control in synthetic water included both removal and inactivation, whereas negligible inactivation was measured in surface water by iron. Hence, NOM

appears to inhibit inactivation by decreasing the ROS generation rate, scavenging ROS, and complexing with Fe(II), thereby reducing its interactions with capsid amino acids. Direct measurements of ROS need to be made to provide more conclusive evidence for inactivation mechanisms in the iron electrocoagulation cell. In any case, experimentation using synthetic water alone is insufficient, and virus removal/inactivation should be quantified directly using natural water before implementing iron electrocoagulation for drinking-water treatment.

Greater reductions in virus concentrations were obtained by aluminum electrocoagulation and electroflotation than by conventional aluminum sulfate coagulation. This improvement was attributed to electrophoretic migration of viruses, which increased their concentrations in the microenvironment of the sacrificial anode, where coagulant precursors are dissolved, leading to better destabilization during electrolysis. In all cases, viruses were not inactivated, implying that the measured reductions were solely due to their removal. Sweep flocculation was the primary virus destabilization mechanism. Direct evidence for the enmeshment of viruses into flocs was provided by two independent methods: quantitative elution using beef extract at elevated pH and quantitative fluorescence from labeled viruses. Atomic force microscopy (AFM) studies revealed a monotonically increasing adhesion force between viruses immobilized on AFM tips and floc surfaces with electrocoagulant dosage, which suggests that adsorption of viruses onto flocs made a secondary contribution to virus uptake. Virus sorption mechanisms include charge neutralization and hydrophobic interactions with natural organic matter removed during coagulation. These mechanisms also provided the basis for interpreting additional removal of viruses by the thick cake formed on the surface of the microfilter following electrocoagulation. Enhancements in virus removal as progressively more aluminum was electrolyzed therefore embodied contributions from (i) better encapsulation within greater amounts of fresh $Al(OH)_3$ precipitates, (ii) increased adsorption capacity due to higher available coagulant surface area, (iii) greater virus-floc binding affinity due to effective charge neutralization and hydrophobic interactions, and/or (iv) additional removal by a “dynamic membrane” if a thick cake layer of flocs is deposited.

Aluminum electrocoagulation and electroflotation outperformed conventional alum coagulation as a highly effective and facile method to remove viruses. These pretreatment processes also significantly reduce microfilter fouling [29, 37] and remove a host of other contaminants, which include (but are not limited to) suspended solids, bacteria, organic compounds, algae, and metals, from municipal and industrial wastewaters [9, 11]. Since coagulant dosage can be adjusted by simply changing the current density, rapid fluctuations in feed water quality can be easily handled. Their operational advantages coupled with their compactness make integrated electrochemical–MF processes very well suited for many practical applications, including treatment in small-scale drinking-water plants, portable units to supply potable water during emergencies, and water and wastewater treatment in military forward operating bases [5]. However, larger

scale testing and engineering cost comparisons are necessary before electrochemical processes can be recommended over conventional chemical coagulation for full-scale applications.

Two important advantages of electroflotation over electrocoagulation are that it inherently creates an additional microbial barrier (floc flotation) without adding a separate unit process and that it achieves a higher MF flux [29]. An important impediment to widespread implementation of these technologies is passivation, which reduces Faradaic coagulant dissolution due to the accumulation of corrosion products and macromolecules on electrode surfaces or formation of an oxide film [12]. On the other hand, pitting can lead to super Faradaic dissolution. In either case, unreliable coagulant dissolution is detrimental to electrochemical cell performance and necessitates system downtime for periodic electrode cleaning. Further, the kinetics of these phenomena cannot be predicted a priori during treatment of natural waters, which necessitates long-term site-specific evaluations.

OBJECTIVES AND APPROACH

Based on the literature review described in the Background and Introduction section, above, the following objectives were formulated:

- Determine performance mechanisms for electrocoagulation, electroflotation, and microfiltration by varying operating conditions such as electrocoagulant dosage, feed water pH, and transmembrane pressure,
- Quantify improvements in microfilter flux following electroflotation of surface water,
- Rigorously elucidate changes in the chemical composition of the foulant during progressive physically irreversible (i.e., non-backwashable) fouling of a commercially available modified PVDF membrane during MF of untreated and pretreated Lake Houston water,
- Elucidate physical and chemical factors contributing to the compressibility of cakes formed during dead-end MF of untreated and coagulated surface water,
- Empirically demonstrate improved permeate fluxes during constant-pressure NF of surface water following (electro)coagulation–MF pretreatment and identify major foulants,
- Determine mechanisms of virus control from natural surface water by a combined iron electrocoagulation–microfiltration process, and
- Empirically demonstrate enhanced virus removals from surface water in a hybrid aluminum electrochemical–MF process and systematically elucidate the underlying destabilization/removal mechanisms.

As explained above, we are particularly interested in mitigating membrane (both MF and NF) fouling during surface water treatment. In all cases, Lake Houston was used as a representative surface water source. Morphological aspects of aluminum precipitates were probed using X-ray diffraction. We used both optical microscopy and an electrical sensing zone device to characterize floc size distributions prior to constant-pressure MF. Electroflotation was also compared with raw-water MF (i.e. no pretreatment) and electrocoagulation pretreatment in the dead-end mode in a range of aluminum dosages and pressures at pH 6.4. Experimental flux profiles were interpreted using cake filtration theory as well as the fractal dimension, average size, zeta (ζ) potential, and elemental composition of the aggregates in the microfilter feed water.

For backwashing, we evaluated operational improvements in flux over five filtration/regeneration cycles (i.e., reductions in reversible and irreversible fouling) achieved by electroflotation pretreatment. Foulants present in the raw water and the mechanisms by which they were removed during electroflotation pretreatment were identified using attenuated total reflectance–FTIR spectroscopy (ATR-FTIR) and XPS. In addition to chemical fingerprinting, foulant complexation on membrane surfaces was probed through intensity changes in $C(=O)O^-$ stretching vibrations region of IR spectra. Instantaneous MF flux profiles were measured over a range of pressures for raw Lake Houston water without pretreatment and after alum and electrocoagulation at two aluminum dosages. Insights into elastic compaction were obtained by identifying precipitate phases using powder X-ray diffraction (XRD), microscopy, and modeling transient flux decline profiles. Physical parameters of colloids measured included size distribution, ζ potential, and fractal dimension. XPS was used to characterize the elemental composition of colloids, their chemical state and functionalities, and changes in spectral peak location and area induced by variations in electron density of their microenvironment following electrocoagulation and alum coagulation. Note that functionality refers to the functional groups present in organic molecules. This information was used to obtain insights into specific interparticle interactions in (electro)coagulated flocs and their effects on inelastic compression.

For surface-water NF, we compared conventional alum coagulation and electrolytic aluminum addition as MF pretreatment alternatives. (See Figure 1 for a schematic of various dual-membrane systems evaluated.) To our knowledge, this is the first systematic and rigorous investigation of these integrated membrane systems. Virgin and fouled NF membranes were extensively characterized in terms of hydrophobicity, surface morphology (scanning electron microscopy and AFM), and organic functionalities and elemental composition (ATR-FTIR spectroscopy and XPS, respectively) to identify dominant foulants and fouling mechanisms. We also used Alcian Blue staining to detect acidic polysaccharides, which typically represent transparent exopolymers of biological origin.

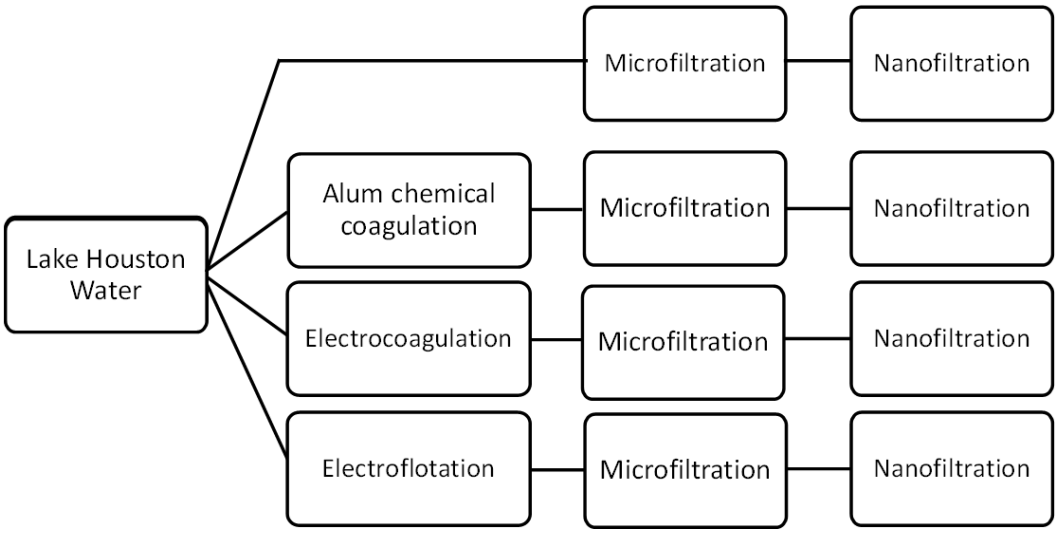

Figure 1. Schematic representation of NF pretreatment alternatives and integrated membrane systems evaluated.

To investigate virus removal, our raw-water results were compared to experimental results obtained using synthetic water and conventional iron chemical coagulation (with $FeCl_3$) to empirically demonstrate the role of NOM in inhibiting virus control during electrocoagulation. Virus removals were evaluated over a range of iron dosages (0–13 mg/L) and at pH 6.4 and 7.5. AFM was used to quantify the adhesion forces between viruses covalently immobilized on AFM tips and surfaces of electrochemically generated flocs at different aluminum dosages. Direct evidence of virus enmeshment and sweep flocculation was presented using fluorescence microscopy and quantitative elution from flocs at high pH. The MS2 coliphage was used since it is a conservative surrogate for the removal of human viruses by coagulation [98] and is commonly employed in environmental studies [16, 97, 99].

During the course of this project, the following peer-reviewed papers were published in archival journals:

1. Gamage, N.P., and S. Chellam (2011). Aluminum Electrocoagulation Pretreatment Reduces Fouling during Surface Water Microfiltration. *Journal of Membrane Science*, **379** (1–2) 97–105.
2. Gamage, N.P., J. Rimer, and S. Chellam, (2012). Improvements in Permeate Flux by Aluminum Electroflotation Pretreatment during Constant Pressure Microfiltration of Surface Water. *Journal of Membrane Science*, **411–412** 45–53.
3. Tanneru, C.T., and S. Chellam, (2012). Mechanisms of Virus Control during Iron Electrocoagulation – Microfiltration of Surface Water. *Water Research*, **46**, 2111–2120.
4. Sari, M.A., and S. Chellam (2013). Surface Water Nanofiltration Incorporating (Electro)Coagulation — Microfiltration Pretreatment: Fouling

Control and Membrane Characterization, *Journal of Membrane Science*, **437**, 249–256.

5. Tanneru, C.T., J.D. Rimer, and S. Chellam (2013). Sweep Flocculation and Adsorption of Viruses on Aluminum Flocs during Electrochemical Treatment Prior to Surface Water Microfiltration. *Environmental Science and Technology*, **47** (9), 4612–4618
6. Gamage, N.P., and S. Chellam (2014). Mechanisms of Physically Irreversible Fouling during Surface Water Microfiltration and Mitigation by Aluminum Electroflotation Pretreatment. *Environmental Science and Technology*, **48** (2), 1148–1157.
7. Gamage, N.P., and S. Chellam (2014). Physicochemical mechanisms of cake compression during (electro)coagulation–microfiltration of surface water. ***Submitted for peer-review prior to possible publication.***

This project report summarizes all the findings reported in the above-mentioned journal publications.

EXPERIMENTS

Source Water

Several discrete water samples were collected over the course of the entire project as summarized in this section. The sample employed for the first set of electro-coagulation experiments was collected from the Lake Houston Canal at the City of Houston's East Water Purification Plant on December 14, 2009. This sample was stored at 4 °C in a walk-in, temperature-controlled room to reduce potential deteriorations in water quality. It could be characterized as being near neutral pH, turbid, soft, with low alkalinity and conductivity, and having high natural organic matter concentrations (Table 1). The values given in Table 1 represent the average and the standard deviation for 31 to 45 analyses of the single water sample conducted over a 9-month time frame between December 18, 2009, and September 3, 2010, during which all experiments were performed.

For the electroflotation experiments and tests evaluating backwashing irreversibility and cake compressibility, water was collected from the Lake Houston Canal at the City of Houston's East Water Purification Plant on January 25, 2011, and also stored at 4 °C. Its water quality, representing 25 to 30 measurements of the stored raw water over the period of experimentation between January 25, 2011, and September 15, 2011, is summarized in Table 2.

The ζ potential of these natural colloids summarized in Table 2 was –17±2 mV. The iron concentration (0.07±0.03 mg/L) was very low compared with aluminum (0.21±0.04 mg/L) and silicon (2.5±0.3 mg/L). Proteins and carbohydrates were measured as 0.24 mg/L and 0.75 mg/L, respectively, by colorimetry [100]. The

pH was reduced to 6.4 using 0.1-*N* HCl before microfiltering the untreated raw water. Total Si concentrations were 2.5±0.3 mg/L, respectively. Sulfate, nitrate, and nitrite concentrations in the raw water were 8 mg/L, 0.168 mg/L, and <0.01 mg/L respectively.

Table 1. Summary of Water-Quality Parameters for the Sample Collected on December 14, 2009

Parameter	Units	Value
pH	- - -	7.4 ± 0.14
Turbidity	NTU*	24.9 ± 2.4
Total hardness	mg/L as $CaCO_3$	41.5 ± 1.2
Calcium hardness	mg/L as $CaCO_3$	34.0 ± 1.2
Alkalinity	mg/L as $CaCO_3$	39.4 ± 1.6
Conductivity	µS/cm	169.7 ± 2.68
Dissolved Organic Carbon	mg/L	7.97 ± 0.50
UV_{254} **	cm^{-1}	0.345 ± 0.018

* NTU = nephelometric turbidity units.
** UV_{254} = absorbance of ultraviolet light with a wavelength of 254 nm.

Table 2. Summary of Water-Quality Parameters for the Sample Collected on January 25, 2011

Parameter	Units	Value
pH	- - -	7.6 ± 0.19
Turbidity	NTU	14.7 ± 1.5
Total hardness	mg/L as $CaCO_3$	51 ± 3
Calcium hardness	mg/L as $CaCO_3$	48 ± 3
Alkalinity	mg/L as $CaCO_3$	71 ± 2
Conductivity	µS/cm	328 ± 13
Dissolved Organic Carbon	mg/L	4.9 ± 0.50
UV_{254}	cm^{-1}	0.143 ± 0.005

For NF experiments, a 25-gallon sample was collected from the Lake Houston canal at the East Water Purification Plant in January 2012 and stored in the dark at 4 °C over the course of experimentation (Table 3).

Water quality parameters for the sample employed to evaluate virus control by iron electrocoagulation are given in Table 4. Experiments were also conducted with synthetic water, prepared by adding 3 m*M* $NaHCO_3$ and 1 m*M* $CaCl_2$ to deionized water (and in some cases Suwanee River Humic Acid was also added). Similar data for the water sample used for aluminum electrocoagulation experiments is also provided in Table 4.

In all cases, the coefficient of variation for all monitored water-quality parameters was 5 percent or less, allowing the comparison of results from various experiments performed using the respective samples.

Table 3. Summary of Water-Quality Parameters for the Sample Collected in January 2012

Parameter	Units	Value
pH	- - -	7.9 ± 0.16
Turbidity	NTU	18.8 ± 1.0
Total hardness	mg/L as $CaCO_3$	67 ± 3.3
Calcium hardness	mg/L as $CaCO_3$	56.1 ± 2.05
Alkalinity	mg/L as $CaCO_3$	85.7 ± 3.2
Conductivity	µS/cm	394.4 ± 14.9
Dissolved Organic Carbon	mg/L	6.9 ± 0.33
UV_{254}	cm^{-1}	0.170 ± 0.009

Table 4. Summary of Water-Quality Parameters for the Sample Collected for Virus Electrocoagulation Tests

Parameter	Units	Iron	Aluminum
pH	- - -	7.5	7.7 ± 0.2
Turbidity	NTU	8	15 ± 2
Total hardness	mg/L as $CaCO_3$	60	53 ± 3
Alkalinity	mg/L as $CaCO_3$	57	70 ± 3
Conductivity	µS/cm	288	322 ± 13
Dissolved Organic Carbon	mg/L	4.9	5.2 ± 0.6
UV_{254}	cm^{-1}	0.165	0.145 ± 0.005

Electrocoagulation

Each experiment consisted of electrochemically coagulating 450 mL of water at room temperature in a cylindrical Perspex cell at pH values of 6.4 or 7.5 maintained to a precision of ± 0.2 pH units. A single 15-cm-long aluminum rod (Alfa Aesar Puratronic® grade, 99.9965% as Al) served as the anode, which was surrounded by a porous, cylindrical grade-316 stainless steel cathode. The inside and the outside surfaces of the cathode were wetted thoroughly. The anodic active surface area was 12.5 cm^2, corresponding to 10 cm of the rod being submerged in water. As predicted by Faraday's Law (Equation 2), different aluminum concentrations can be generated by varying either the current or the generation time:

$$m = \frac{26.98\, I\, t}{zF} \tag{2}$$

where m is the mass in grams of Al generated at a specific current (I, amperes) over a time interval (t, seconds), z is the number of electrons transferred per Al atom, 26.98 g M^{-1} is the atomic weight of Al, and F is Faraday's constant (96,486 C Eq^{-1}). In our experiments, the current density was kept constant at 20 mA/cm^2 with cell voltage between 7 and 8 V. Different Al dosages in the range 2–30 mg/L were generated by operating the unit for different times in batch mode.

Electrocoagulation was carried out in two steps: electrolysis and flocculation. It is emphasized that, in accordance with the most common application of coagulation pretreatment for MF during water/wastewater treatment, a separate sedimentation step was not employed. During electrolysis, the solution was rapidly mixed with a magnetic stirrer to enhance mass transfer of aluminum away from the anode. The suspension was then slowly mixed for 2 minutes to flocculate the destabilized particles. Since deposit accumulation around the anode can cause problems with electrochemical dissolution, the anode was mechanically scrubbed with a waterproof silicon paper sanding sheet (100 grit, McMaster-Carr) before each experiment (and its diameter was measured) in order to maintain the aluminum generation efficiency. As reported earlier [12, 19], electrocoagulation increased the water pH, especially given the low buffering capacity of the source water. Empirically, we observed a greater pH increase with longer electrolysis duration—e.g., when the initial source water pH was 7.5, the pH after electrolysis increased to 7.8 for a 10-mg/L aluminum dose and to 8.0 for a 30-mg/L aluminum dose. Figure 2 is a photograph of our electrochemical cell.

Figure 2. Photograph of the custom-designed, plexi-glass electrochemical cell employed in all experiments.

The perforated stainless steel cathode is also visible. Note that the spigot is placed at the bottom of the cell so as to not transfer the floating flocs.

Microfiltration

Constant-pressure, unstirred dead-end filtration experiments were conducted using a commercially available cell, with 4.1 cm^2 of effective filtration area (Millipore Model 8010). Modified PVDF membranes rated at 0.22 µm (Millipore GVWP02500) were used. The system was pressurized by compressed air, and the feed pressure was maintained at predetermined values in the range 13–166 kPa (2–24 psig) using a precision regulator (Omega PRG101-60). The length of tubing and number of fittings were kept to a minimum in order to more accurately monitor the time trace of permeate flux. First, 100 mL of ultrapure water was passed through the system to rinse the membrane of any preservatives and

evaluate its resistance prior to filtering 150 mL of the electrocoagulated suspension. The Darcy resistance (R_m) of the membranes employed in this study was $5.38 \pm 0.42 \times 10^{10}$ m^{-1}.

A transducer (Omega PX303-050G5V) and a digital balance (Fisher Scientific Ohaus Navigator N1H110) were used to monitor the pressure and cumulative mass, respectively, of the permeate water during filtration. Data were acquired at a frequency of 1 Hz for the first 2.5 cm^3/cm^2, 0.2 Hz between 2.5 and 5 cm^3/cm^2, and 0.1 Hz for > 5 cm^3/cm^2 of water filtered per area of membrane using a computerized data acquisition system programmed in LabVIEW (National Instruments). The cumulative permeate volume per unit membrane area data acquired over time was exponentially smoothed using a damping factor of 0.3 prior to numerical differentiation to obtain the instantaneous flux. Following filtration, the cake was weighed after drying to a constant weight for 16 h at 35 °C.

To obtain sufficient volume of water for NF experiments, constant-pressure, unstirred dead-end microfiltration experiments were conducted using a 300-mL stainless steel cell and nylon membranes rated at 0.45 μm with 17.3 cm^2 effective area (Millipore HNWP04700). Approximately 8 L of permeate was collected for each type of pretreatment (electrocoagulation, electroflotation, chemical coagulation) for subsequent NF. Lake Houston water was also simply microfiltered without any type of coagulation, to serve as a negative control for NF fouling comparisons.

Backwashing

Fouled membranes were physically regenerated using a three-step procedure. In the first step, the membrane was carefully removed from the cell, and its surface was rinsed with a jet of Nanopure™ water to dislodge the loosely adhered cake layer (simulating fast flushing). Separately the filtration cell was also rinsed with Nanopure water. Secondly, similar to earlier work [50, 101, 102], the remaining thin gel-like layer was gently wiped with a fine tissue, and the membrane was replaced upside-down in the cell. Thirdly, 100 mL of Nanopure water was passed through the upside-down membrane (representing backwashing) at 17 kPa. The entire filtration and regeneration procedure constitutes one cycle and was repeated five times for untreated and electrofloated water. Finally, the membrane orientation was reversed to the original direction and the clean-water flux was again recorded to quantify the progressive buildup of irreversible fouling. Control experiments using Nanopure water revealed that this regeneration procedure did not affect the virgin membrane permeability over five cycles. After cycles 1 and 5, membranes were immersed in 25 mL of HCl (pH 2) and kept in a reciprocating shaker (220 rpm) for 200 minutes at 40 °C. This process was repeated using NaOH (pH 12). Dissolved organic carbon (DOC) and Al removed from the membranes were measured to estimate the mass of NOM and Al accumulated during fouling.

Nanofiltration

Bench-scale crossflow NF experiments were performed using a stainless steel cell (Osmonics SEPA-CF) fitted with a 19 cm × 14 cm flat sheet (155 cm^2 effective area) of a commercially available thin-film composite membrane (GE Osmonics DL) including feed and permeate spacers. This membrane consists of four layers including a ~0.2-mm-thick polyester reinforcing fabric, a ~0.05-mm-thick microporous polysulfone support, a ~0.2-μm-thick polyamide active layer, and a proprietary ultrathin skin. We have measured the molecular weight cutoff of this membrane to be 268 g/*M*, corresponding to an approximate mean pore size of 1.46 nm [103].

The feed water was delivered by a positive displacement gear pump (Cole-Parmer head model 73004-02 and drive model 75211-10). The recovery was accurately controlled at 80 percent with a flow meter (Fischer & Porter 1450NIA/7506) and a high-precision needle valve (Swagelok 316 JWS) in the concentrate stream. The system was operated in batch recycle mode by continuously returning permeate and concentrate flows to the feed tank (except during sampling) [104]. Pressures and temperature were monitored using analog transducers (Omega PX603 and TJ120 CPSS 116G, respectively). Additionally, permeate and concentrate flows were measured with digital balances (Fisher Scientific Ohaus Navigator N1H110) connected via LabView (National Instruments, v. 8.5) to a personal computer. Membrane setting was achieved by passing 5 m*M* NaCl solution for 24 h at 470 kPa. Pretreated surface water was then filtered at a constant pressure of 470 kPa, corresponding to an initial clean membrane flux of 29.9 ± 2.9 L/m^2-h, and a Darcy resistance of $5.83\times10^{13} \pm 5.68\times10^{12}$ m^{-1}. Experiments were conducted at room temperature (24 °C) for a minimum of 170 hours at 80 percent recovery. Due to flux decline, adjustments were periodically made to the back pressure valve to maintain constant pressure and recovery.

Two-sided, two-sample *t*-tests revealed no differences (at the 0.05 significance level) between experimentally measured and theoretically predicted retentate DOC concentrations, UV absorbance at 254 nm, and conductivity at steady-state. Additionally, very similar instantaneous NF fluxes were measured when the entire electroflotation–MF–NF experiment was repeated. These observations, coupled to the consistency of the raw-water quality, demonstrate the accuracy of our experimental protocols and instrumental analyses.

Floc Physical Characteristics

Effective size distributions of coagulated suspensions and colloids in the raw water were obtained using an electrical sensing zone device (Beckman Coulter Multisizer III) within 30 minutes of electrocoagulation. Particles in the 2–240 μm size range were detected using 100- and 400-μm-diameter apertures, which were calibrated using highly monodispersed polystyrene latex beads (certified by the

National Institute of Standards and Technology) of size 10 μm and 43 μm, respectively. Particle size distributions were obtained with a current of 3,200 μA and a gain of 1 after 100-fold dilution with prefiltered 2-percent NaCl solution containing 20 percent glycerin. Adding glycerin increased the viscosity of the background electrolyte, thereby reducing clogging and floc breakage when flocs passed through the aperture. One milliliter of the suspension was drawn and each run was completed in 20 s. The entire suspension was gently stirred during the analysis period in order to avoid settling. Resulting size distributions from the two different apertures were merged using MULTISIZER/Z2 AccuComp® software provided with the instrument. The average of triplicate analysis of each sample is reported herein. (See "Characteristics of Flocs Formed at Different Aluminum Dosages," below.)

Flocs were also observed under an optical microscope (CTR4000 from Leica Microsystems Wetzlar GmbH, Germany) to visualize their sizes and shapes. Electrocoagulated water samples, 0.2 mL each, were placed on glass slides using a manual pipette; the tip of the pipette had been cut to 5 mm diameter and excess water was carefully removed with a tissue paper. Phase contrast images were obtained using a 10× objective with 1.6× enhanced magnification. RGB images with a resolution of 1,280×1,024 pixels were obtained with a high-speed digital camera (S-PRI from AOS Technologies AG, Switzerland) using AOS Imaging Studio (v. 3.2.5) software. The microscope was calibrated using a graduated microscale where the scale for images obtained under the aforementioned settings was 1.2±0.2 μm/pixel. Images were processed and particle sizes analyzed using MATLAB R2009b software with the image processing toolbox. The RGB image was converted to a 256-gray-level image after image enhancement (brightness, contrast adjustment, and histogram correction) and then histogram-based thresholding was applied to differentiate dark and bright pixels in order to differentiate the background from the particles. The connected components in the resulting binary image were labeled, and the inbuilt function *regionprops* was used to calculate the equivalent diameters of the connected regions. Size distributions were calculated using the equivalent diameter data obtained in terms of pixels and converted to micrometers later.

The projected area of the flocs was determined as the difference between the total floc area and the total area of voids, and the characteristic length was the diameter of the smallest circle that would completely encircle a single aggregate. 2D fractal dimensions $d_{f,2D}$ were obtained by digitally analyzing the images (ImageJ Version 1.45S) with the box counting technique [105]:

$$d_{f,2D} = \lim_{L \to 0} -\frac{\log(N)}{\log(L)} \tag{3}$$

where N is the minimum number of square boxes required to completely cover the aggregate and L is the box size. The fractal dimension was obtained as the slope of the log-log plot of the number of squares versus the corresponding resolutions of the square boxes.

Mass fractal dimensions of the electrocoagulated and electrofloated aggregates ($d_{f,3D}$) were measured using static light scattering (Brookhaven Instruments BI-200SM) equipped with an He-Ne laser (wavelength, $\lambda = 632.8$ nm) and a BI-9000AT correlator. Scattered intensities were recorded at angles θ between 14° and 75°, which was determined to be the linear fractal range during preliminary experimentation. The disturbance from dust was minimized by using the built-in statistical dust rejection function and setting a light rejection ratio of 3.0. To reduce multiple scattering, sedimentation, and excessive count rates, flocs were broken (assuming self-similarity at all length scales) by applying high shear and diluted in 25-percent glycerol (1 mL sample + 19 mL 25% glycerol) prior to analysis to increase the viscosity (i.e., to delay floc sedimentation). The scattered intensity (I) was corrected for the refractive index (n) and background scattering. Data were collected as a function of the scattering vector, $q = (4\pi n/\lambda) \sin \theta/2$, to probe length scales (q^{-1}) between 39 and 290 nm. Background correction was made by measuring intensities arising from the 25-percent glycerol liquid medium used for dilution immediately before each analysis.

The fractal dimension of aggregates was calculated using Rayleigh-Gans-Debye theory ($I \alpha q^{-d_{f,3D}}$) [106, 107], which is applicable when $R_a^{-1} << q << R_p^{-1}$ for dilute suspensions of uniform primary particles with low refractive index (where R_a and R_p are the radii of the aggregate and the primary particle, respectively). The exponent in the Rayleigh-Gans-Debye theory does not strictly correspond to the fractal dimension [105] when applied to aggregates formed from polydispersed natural colloidal suspensions typical of surface waters [107–109]; however, the scattering exponents are representative of fractal dimensions [107], and those reported herein are an average of at least three separate static light-scattering measurements from each sample.

Microscopy

Scanning electron micrographs of clean and fouled membranes were obtained with a field-emission scanning electron microscope (Carl Zeiss LEO 1525) after sputter coating the oven-dried samples (16 h at 35 °C) with a 10-nm layer of gold. Electron-dispersive spectra (EDS) of sputter-coated filter cakes were acquired with 15-keV primary beam voltage on a Jeol JSM 6330F microprobe using an Oxford Instruments ISIS 300 EDS detector.

Surface Charge

The electrophoretic mobility of electrocoagulated suspensions was measured using the electrophoretic light-scattering technique (Nicomp 380 ZLS from Particle Sizing Systems, Santa Barbara, CA). An He-Ne laser with a wavelength of 632.8 nm, an electrode spacing of 0.4 cm, and a field strength of 10 V/cm were employed for all measurements. Colloidal silica suspensions (Snowtex 50 from Nissan Chemicals, Houston, TX) were used for calibration. The Smoluchowski

equation was used to convert electrophoretic mobility to zeta potential. Each sample was run in two replicates of 60 seconds duration each.

Powder X-Ray Diffractometry

The polymorphs of precipitates produced during aluminum electrocoagulation were identified using an XRD system (Siemens D5000) equipped with a graphite monochromator. The flocs were collected after filtration and dried for 1 day at ambient temperature because drying at higher temperatures can lead to experimental artifacts such as increased crystallinity [110]. The flocs were then powdered and dispersed in isopropyl alcohol. The alcohol was then evaporated in order to make a thin uniform coat on the zero-background quartz sample holder. Diffraction patterns were collected using Cu Kα radiation (1.54056 Å) at 40 kV and 30 mA in the 2Θ scan range from 5° to 60° with steps of 0.04° 2Θ/s. A quartz standard was measured initially for calibration purposes. The Joint Committee for Powder Diffraction Studies database was used to interpret the diffraction patterns and identify the peaks.

X-Ray Photoelectron Spectroscopy

Measurements of the fouled and clean membranes were performed using a PHI 5700 X-ray photoelectron spectrometer equipped with a monochromatic Al Kα X-ray source (hν = 1,486.7 eV) incident at 90° relative to the axis of a hemispherical energy analyzer. Since the samples were insulating, analysis was done by turning on the neutralizer. Survey spectra in the range 0–1,400 eV were recorded for 5 minutes at 187.85 eV bandpass energy on a spot diameter of 1.1 mm. High-resolution spectra were obtained for photoelectrons emitted from C 1s, Al 2p, and O 1s at a 45° take-off angle. All spectra were collected at room temperature with a base pressure of 1×10^{-8} torr. Electron binding energies were calibrated with respect to the C 1s line at 284.8 eV. PHI Multipak software (v. 5.0 A) was used for data acquisition and analysis. The high-resolution data was first analyzed by background subtraction using the Shirley routine and nonlinear fitting to mixed Gaussian-Lorentzian functions. Atomic compositions were derived from the survey spectra. Peak areas were obtained after subtraction of the integrated baseline and corrected for sensitivity factors. More than three analyses were performed at different regions on each membrane to account for potential non-homogeneities. Results were interpreted using the National Institute of Standards and Technology X-ray Photoelectron Spectroscopy Database 20, Version 3.5.

ATR-FTIR

Spectra were collected using a Nicolet iS10 FTIR spectrometer ATR accessory with a Ge reflection element (45° incidence angle), equipped with a mid-infrared Ever-Glo source, a KBr/Ge beam splitter, and a fast-recovery deuterated

triglycine sulfate detector. Each reported spectrum is an average of five spectra, each consisting of 512 coadded scans at 2 cm^{-1} resolution, 16 cm^{-1} phase resolution, 20-kHz low-pass filter, a zero-filling factor of 2 using a Blackman Harris four-step apodization, and Mertz phase correction. Spectra were obtained for (1) source water, (2) "pure" electrocoagulant precipitates generated in Nanopure water (control experiment), (3 and 4) flocs floated to the surface and those suspended in the water column after electrochemical pretreatment of Lake Houston water, (5) wetted virgin membrane, and (6 and 7) irreversibly fouled membranes after cycles 1 and 5. Solids were vacuum-dried for 1 h and the moist paste was pressed uniformly on the Ge crystal with maximum contact, whereas membranes were analyzed as they were. Spectral processing including baseline correction and subtraction was performed using OMNIC (v. 8.3) software. Second derivatives were employed to enhance resolution.

Aluminum Measurement

. Water samples were collected before and after electrocoagulation and acidified to pH 2 using 11.5-*N* HCl (final concentration 2%) to redissolve aluminum precipitates before instrumental analysis. Total aluminum concentrations were analyzed using flame atomic absorption spectroscopy (Perkin-Elmer Flame AA-AAnalyst 300) according to Standard Method 3111. The instrument was calibrated in the range 0–50 mg/L using 1,000-mg/L Al stock solution with 2-percent HCl (High Purity Standards) prior to each set of measurements. Given the importance of accurate aluminum measurements to this study, concentrations covering the entire range of dosages were independently verified using inductively coupled plasma–mass spectrometry. The two analytical techniques agreed within 95 percent confidence, demonstrating the accuracy of our aluminum measurements.

Iron Measurement

Total iron was measured using atomic absorption spectroscopy (Perkin-Elmer AAnalyst 300) after acidifying the samples to pH < 2 using HNO_3. Ferrous iron in electrocoagulated waters was determined by chelating it to 1,10 phenanthroline after adding HCl to bring the pH to 4 and buffering with acetate. The resulting reddish-orange complex was quantified by light absorption at 510 nm using a spectrophotometer (Hach Co., Loveland, CO). The difference between total iron and ferrous iron concentrations gave the ferric iron concentration.

Nanofilter Contact Angle

Approximately 3 µL of ultrapure water was gently placed on dried virgin and fouled membrane surfaces, and the contact angle was recorded using a goniometer (Dataphysics OCA 15EC) fitted with a camera. The sessile drop technique applied

to the entrance and exit regions (three replicates each) of the specimens gave very similar contact angles. Therefore, the average of the equilibrium right and left angles (total of 12 measurements) from different locations, allowing for ~15 seconds droplet spreading, is reported.

Staining for Acidic Polysaccharides

NF membrane samples were cut into 1-cm squares and stained with ~2 mL of 1-percent Alcian Blue 8 GX in a 3-percent acetic acid buffer solution at pH 2.5 (Fluka, Sigma Aldrich). After a contact time of 5 minutes, the excess stain was removed by rinsing with ultrapure water, and the membrane was viewed under an optical microscope with 20× magnification (Olympus BX51). The entire procedure was completed rapidly (<15 minutes) to avoid potential degradation of the active layer of the nanofilter at low pH.

Virus Growth and Enumeration

The double-top agar layer technique was employed for MS2 (ATCC 15597-B1) propagation using *Escherichia coli* (ATCC 15597) as the host. *E. coli* was first cultured overnight (18–24 h) in tryptic soy broth (TSB; Difco, Detroit, MI) at 37 °C. Later, the cultured TSB was added to a fresh TSB and grown to a mid-log phase for 3–6 hours also at 37 °C. MS2 stock was serially diluted in phosphate buffered saline (composition 137 m*M* NaCl, 2.7 m*M* KCl, 4.3 m*M* $Na_2HPO_4 \cdot 7H_2O$, and 1.4 m*M* KH_2PO_4; pH 7.5). Next, *E. coli* suspension (0.9 mL) and phage dilution (0.1 mL) were mixed in 3 mL 0.5-percent soft overlay agar and poured onto pre-solidified 1.5-percent trypticase soy agar plates (Difco, Detroit, MI). The plates were incubated at 37 °C for 24 h. Plaques numbering from 20 to 300 were counted, and MS2 concentrations are reported as plaque-forming units per milliliter (PFU/mL). For filtration experiments, 1 mL of purified virus stock was added to 450 mL of feed surface water to obtain a feed concentration of $O(10^7–10^8)$ PFU/mL. All the natural water samples were centrifuged at 5,000 *g* for 20 minutes to remove any debris before plating and propagation.

Recently, quantitative real-time polymerase chain reaction is gaining prominence for virus enumeration to calculate log-removals in water treatment unit processes to reduce potential issues associated with virus aggregation [e.g., 88, 111, 112]. In our experiments, MS2 concentrations in feed waters measured using the plaque assay were very close to the calculated value based on the stock titer, suggesting limited phage aggregation. Additionally, since the plaque assay continues to be routinely employed in environmental engineering [e.g., 89, 113, 114], it was used in this research as well.

RESULTS AND DISCUSSION

Electrocoagulation Pretreatment to Microfiltration

Aluminum Generation Accurately Follows Faraday's Law with Three-Electron Transfer

Aluminum concentrations from multiple experiments performed on different days corresponding to various current-passage times are shown in Figure 3. Note that the straight line in Figure 3 is the purely theoretical prediction using Faraday's law obtained for a three-electron transfer ($z = 3$ in Equation 2). As observed, experimental data agree closely with Faraday's law predictions, the relative percent difference varying between only 1 to 6 percent for the entire range of concentrations employed. The extremely accurate predictions of Faraday's law demonstrate the in situ electrochemical generation of aluminum cations with the characteristic +3 oxidation state of group-13 elements at near 100-percent efficiency.

The three-electron transfer inferred from Figure 3 suggests the following major electrochemical reactions:

Anode:	$Al^0\ (s) = Al^{3+} + 3e^-$
Hydrolysis:	$Al^{3+} + 3H_2O = Al(OH)_3\ (s) + 3H^+$
Cathode:	$3H_2O + 3e^- = 3OH^- + 1.5H_2$
Overall:	$Al^0\ (s) + 3H_2O = Al(OH)_3\ (s) + 1.5H_2$

Hydrolysis of Al(III) cations produces protons, reducing the pH in the anodic microenvironment. Note that hydroxide anions generated at the cathode neutralize these protons in the bulk solution, thereby preserving the natural buffering capacity of the source water. This process is in contrast to conventional chemical coagulation wherein iron or aluminum hydrolysis consumes alkalinity (Brønsted acid behavior), necessitating the external addition of a base to neutralize the protons released. Therefore, electrocoagulation achieves a substantial operational advantage, especially for treating low-alkalinity waters such as those of Lake Houston. Other studies have attributed large differences between Faraday's law predictions of electrolytic Al generation and experimental values to pH changes in the electrode microenvironments or to electrode corrosion [12, 15, 19].

Electrochemically generated Al(III) ions can also produce other charged monomeric, dimeric, and polymeric hydroxo-metal complexes such as $Al(OH)^{2+}$, $Al(OH)_2^+$, $Al(OH)_4^-$, $[Al_2(OH)_2]^{4+}$, $[Al_3(OH)_4]^{5+}$, $[Al_{13}O_4(OH)_{24}]^{7+}$, etc., that are surface-active [115, 116]. The atomic structure of $Al(OH)_3$ precipitates was also probed using XRD.

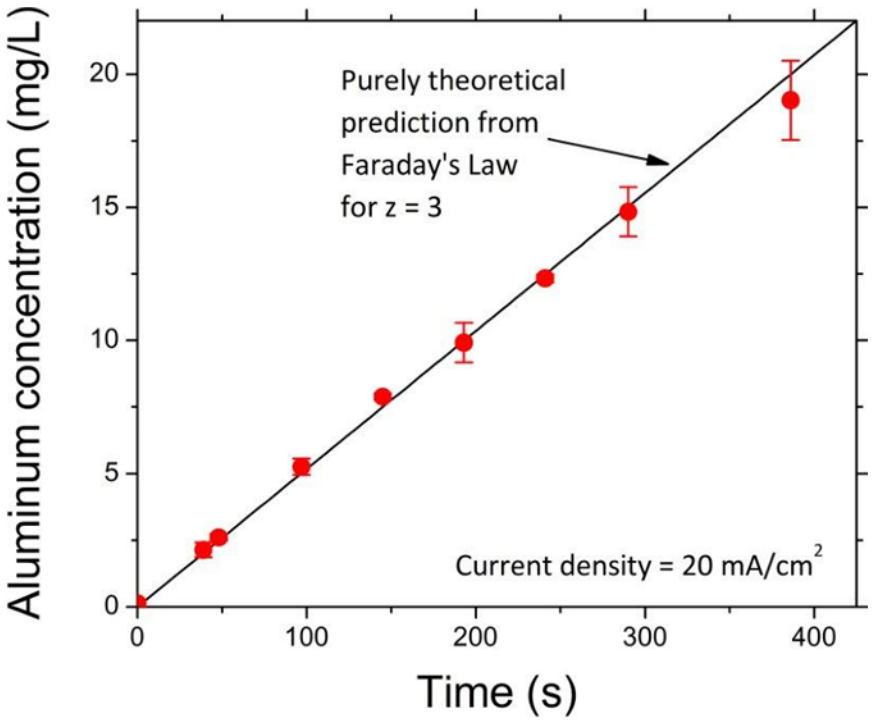

Figure 3. Near 100-percent efficiency of aluminum (Al^{+3}) generation during electrocoagulation of Lake Houston water.

Applied voltage between 7 and 8 V and current density of 20 mA/cm^2.

Electrocoagulation Produces Amorphous Aluminum Hydroxide Precipitates

Aluminum polymorphs formed in situ depend on electrode materials and the source-water composition [117, 118]. Hence, X-ray diffractograms of electro-coagulated samples of natural water were obtained in this research. As summarized in Figure 4, the diffractograms did not show any strong peaks, demonstrating the absence of any crystalline precipitates. This pattern is similar to those of fresh precipitates obtained during alum coagulation of surface water [119] and during electrocoagulation of textile wastewaters [120]. Note that the two clearly visible peaks correspond to silica present in the natural water, which was verified by electron dispersive spectroscopy. Weak signals corresponding to the principal peak of boehmite (020 plane) were also discerned, suggesting the primary species was amorphous $Al(OH)_3$ but that small amounts of the oxyhydroxide AlO(OH) were also present. Note that boehmite is an aluminium oxide hydroxide (γ-AlO(OH)) mineral. Residual water intercalated between the boehmite layers as well as natural organic matter and other constituents disallowed the resolution of the secondary AlO(OH) peaks from the background. Additionally, the weak signal was shifted approximately 1°2θ toward smaller angles, potentially due to high interlayer spacing caused by the lack of long-range order and by the structural distortion of boehmite. Also as seen in Figure 4, the diffractogram of electrocoagulated aluminum precipitates in ultrapure water showed very shallow and broad principal and secondary peaks, which were

stronger than those observed with natural water. Hence, the $Al(OH)_3$ precipitates were amorphous in nature, and small amounts of very fine boehmite grains were present.

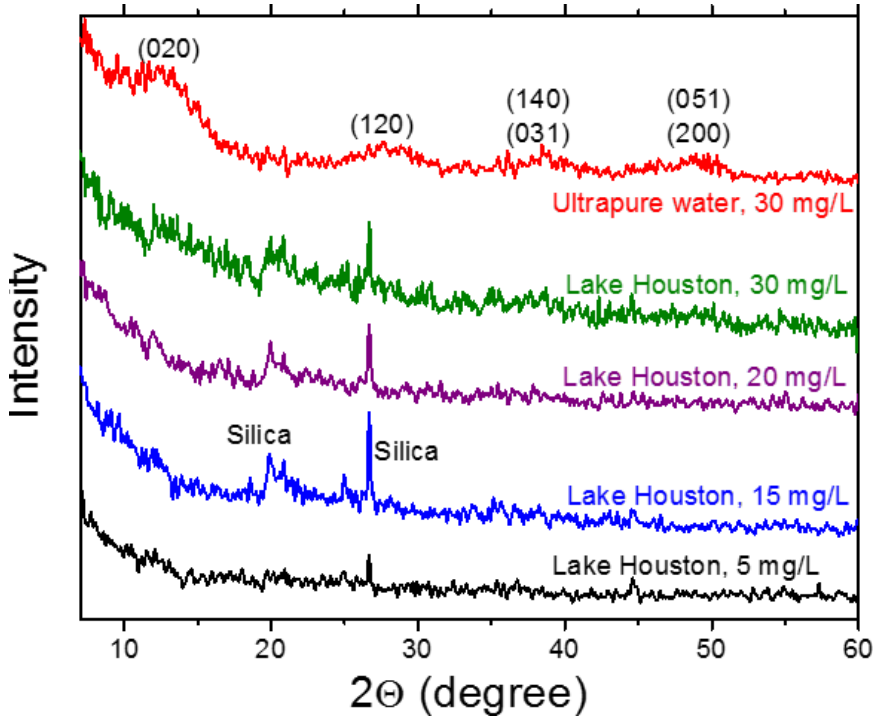

Figure 4. XRD analysis of flocs formed by electrocoagulation of natural and ultrapure waters at different aluminum dosages.

The different scans correspond to various mass concentrations of aluminum coagulant shown next to the individual spectra.

Electron micrographs of $Al(OH)_3$ precipitates formed in ultrapure and natural waters (Figure 5) support this observation, as they reveal no order or habit. In all cases, the aggregates appeared to be largely amorphous and gelatinous masses of various sizes and shapes. The formation of such poorly crystalline precipitates in the presence of natural organic matter is consistent with literature reports of how organic acids compete with hydroxyl ions to form polymorphic amorphous $Al(OH)_3$ [121, 122]. The slightly better definition of the precipitates formed in ultrapure water suggests the role of NOM and other natural water chemical constituents in influencing aluminum precipitation or in adding to the background signal. Note that we dried our samples at room temperature to more closely capture the actual morphology and structure of the fresh precipitates. Drying at higher temperatures (e.g., 105 °C) can increase the order-forming crystalline minerals such as bayerite [25].

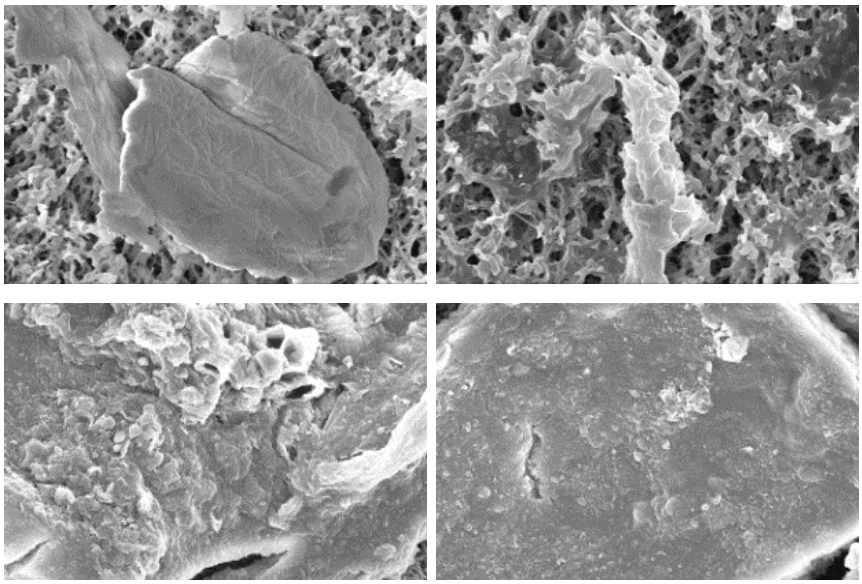

Figure 5. Scanning electron micrographs of $Al(OH)_3$ precipitates.
Precipitates formed in ultrapure water are shown in the top two images, and those formed in natural water at 15 mg/L Al are shown below.

Effect of Aluminum Dosage on Fouling

The relative permeate flux increased with aluminum dosage up to an intermediate value (15–20 mg/L for pH 7.5 and 10 mg/L for pH 6.4) and then reduced when the dose was increased further, as shown in Figure 6 for a low applied pressure of 13.8 kPa. In other words, fouling was alleviated only up to an intermediate value of aluminum dosage, beyond which higher coagulant dosages worsened fouling. Similar observations have been reported for crossflow MF of iron electro-coagulated kaolin suspensions [123] and for dead-end MF of alum-coagulated humic acids [63] and aluminum electrocoagulated silica suspensions [33]. The variations in relative flux with aluminum concentrations were less pronounced at higher pressures, which was attributed to cake compression.

As seen in Figure 6, the cumulative volume filtered (V) fits very well to the classical cake filtration model [2–4]:

$$\frac{t}{V/A_m} = \frac{\mu R_m}{\Delta P} + \frac{\mu \alpha^* c_b}{2\Delta P}\left(\frac{V}{A_m}\right) \tag{4}$$

where A_m is the membrane area, μ is the absolute water viscosity, c_b is the bulk solids concentration, α* is the specific cake resistance on a mass basis, and ΔP is the transmembrane pressure. Also, a thick cake layer of $Al(OH)_3$ flocs, which appeared to have completely enveloped all particles in the raw water, can be seen in the two lower electron micrographs in Figure 5.

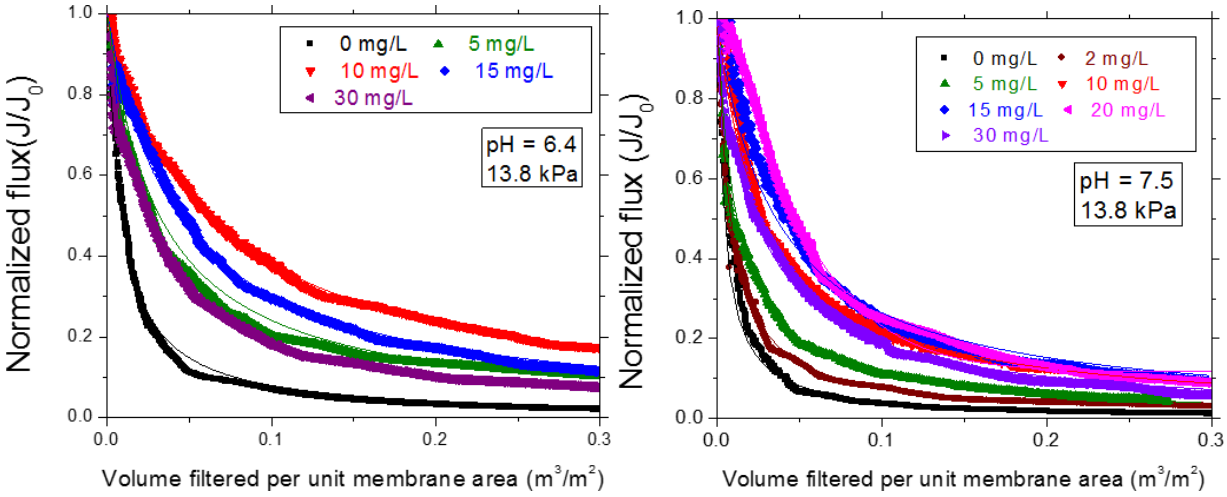

Figure 6. Improvements in relative permeate flux only up to an intermediate value of aluminum dosage at a constant transmembrane pressure for both pH values investigated.

The symbols denote experimental data, and the curves are model fits to Equation 3.

Excellent model fits and visual observations therefore demonstrate that surface deposits played the predominant role leading to flux decline and that cake filtration was the governing fouling mechanism for the entire range of experimental parameters investigated. The absence of a distinct pore-blocking phase is probably due to the higher particle concentration in the current water sample compared with those analyzed for our earlier work [32]. The increased particle concentration is evidenced by the doubling of the feed water turbidity (~25 NTU versus 13 NTU) and by the more efficient precipitation of $Al(OH)_3$ (rather than soluble Fe(II) generation).

As shown in Figure 7, specific cake resistances decrease rapidly with coagulant addition at a fixed transmembrane pressure, the raw water forming the least permeable deposits. Further, as can be expected, higher aluminum concentrations increased the total cake mass for both pH values investigated, as shown in the inset of Figure 7. The conflicting effects of increasing aluminum dosage which on one hand decreased *specific* cake resistance but simultaneously augmented the total loading of colloidal foulants caused the *cumulative* cake resistance to be minimal at an intermediate aluminum concentration (the optimal dose). Note that *optimal* refers to lowest cake resistance and highest relative flux. Floc properties, including size distributions and zeta potential, were measured to mechanistically understand underlying causes of the observed fouling profiles and trends in the cake resistance, as described below.

Characteristics of Flocs Formed at Different Aluminum Dosages

Figure 8 shows volume-based floc size distributions measured using an electrical sensing zone device (Coulter Counter) following electrocoagulation at various aluminum dosages at pH 6.4.

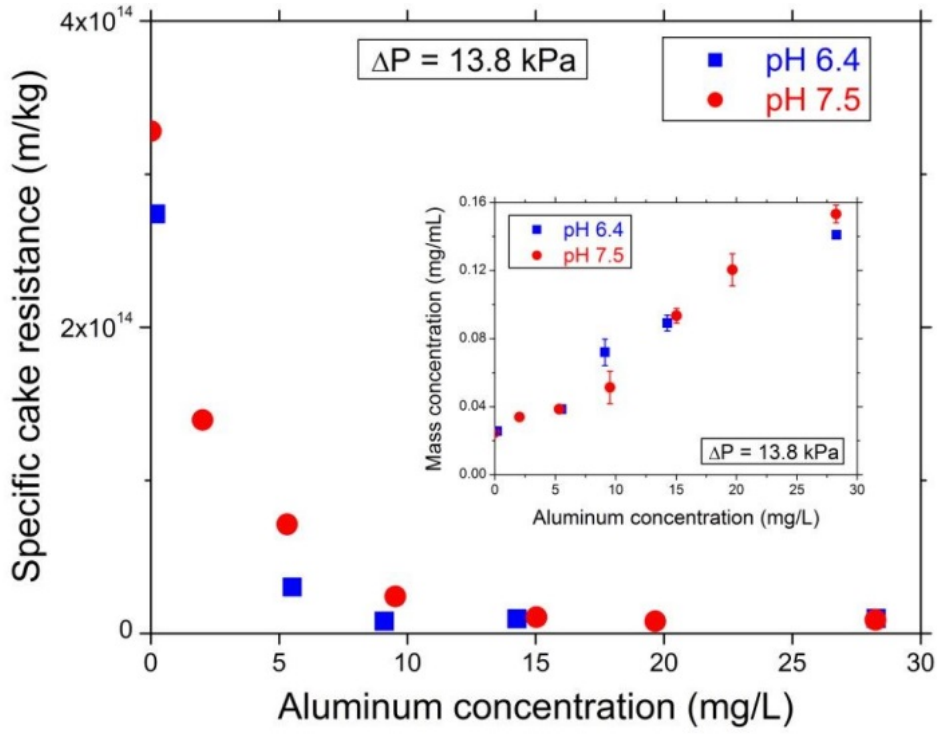

Figure 7. Effects of increasing aluminum electrocoagulant dosage: declining specific resistances at a fixed transmembrane pressure of 83 kPa and increasing total mass of solids in the feed water (inset).

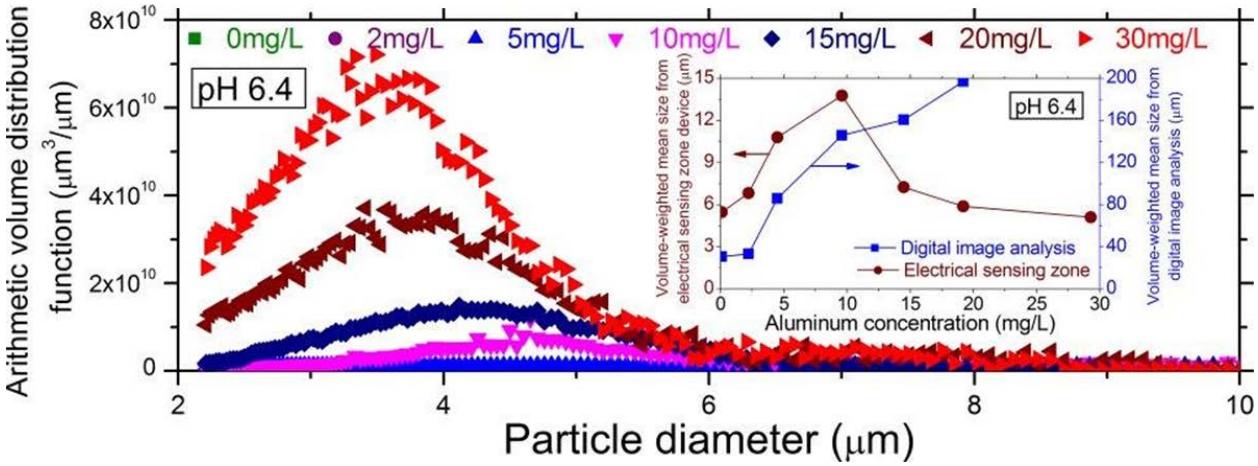

Figure 8. Particle size distributions at different aluminum dosages obtained using an electrical sensing zone device.

The inset summarizes volume-averaged mean diameters obtained from the Coulter Counter and digital analysis of optical micrographs.

As expected, the cumulative floc volume increased monotonically with aluminum dosage, mirroring the observed trend in mass illustrated in the inset of Figure 7. Also as can be seen in Figure 8, the volume distributions shifted to the left, corresponding to smaller sizes as the coagulant dose increased progressively

beyond 10 (optimal dose) to 15, 20, and 30 mg/L. Note that size distributions for lower dosages (0, 2, and 5 mg/L) aren't discernable in Figure 8, due to the significantly lower floc volumes generated. Arithmetic average diameters calculated from these data increased from the raw water (5.5 μm) to the optimal dose of 10 mg/L (13.8 μm) but decreased as more aluminum was added (5.1 μm at 30 mg/L Al), indicating that larger flocs were breaking up as they passed through the instrument's aperture. The flocs were viewed via optical microscopy to avoid this potential artifact and to better determine the actual floc size. As can be seen qualitatively in Figure 9, which shows representative images for the raw water and electrocoagulated suspensions, both particle size and concentration appeared to increase with aluminum concentration. These images were also used to digitally calculate volume-weighted average particle sizes which are summarized in the inset of Figure 8. In contrast to the average diameters calculated with the electrical sensing zone instrument, sizes calculated from digital analysis of microscopic images increased monotonically with aluminum dosage. Further, the average diameter from image analysis was always significantly greater than that measured with the Coulter Counter (e.g., 146.1 and 13.8 μm, respectively, at 10 mg Al/L). Both of these observations are consistent with our earlier hypothesis of floc breakage while passing through the aperture of the electrical sensing zone device. Hence, the formation of larger particles during electrocoagulation pretreatment as more aluminum was added at a fixed pH reduces specific cake resistances during constant-pressure MF.

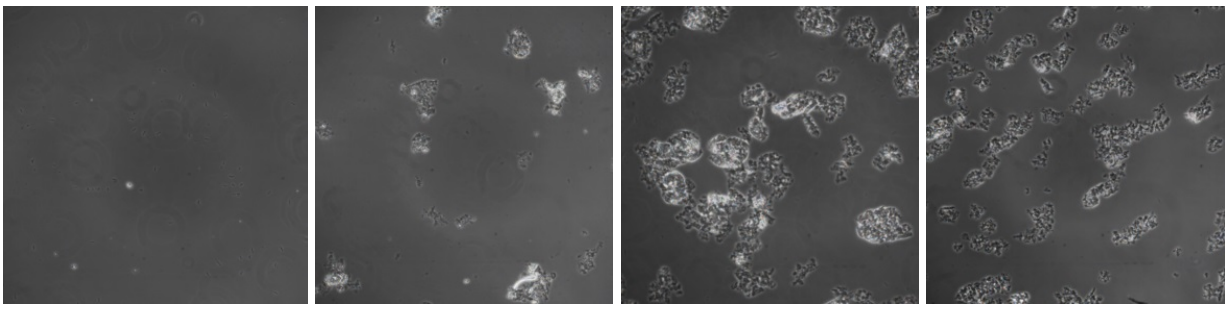

Figure 9. Optical images of flocs formed by electrocoagulation at different aluminum dosages.

As illustrated in Figure 10, zeta potentials of flocs increased (→ 0) with aluminum dose at a constant pH similar to the trends reported earlier for electro-coagulation and chemical coagulation using alum and polyaluminum chloride [17, 124]. Adsorption of hydrolyzed aluminum species onto natural colloidal material will increase the zeta potential of negatively charged flocs [115, 116]. The greater degree of protonation of adsorbed NOM functional groups at lower pH resulted in less negative zeta potentials at pH 6.4 compared with those at pH 7.5. The higher rate of surface charge neutralization with increasing aluminum dosage at pH 6.4 is also consistent with the predominant positively charged species at that pH ($Al(OH)_2^+$), whereas at pH 7.5 the dominant species is negatively charged ($Al(OH)_4^-$). Interestingly, negative floc zeta potentials were measured at the optimal coagulant dosage for fouling control at both pH values. Hence, charge neutralization wasn't the major destabilization mechanism but only played a

secondary role to enmeshment and sweep flocculation during electrocoagulation. In contrast, alum destabilized humic acids in synthetic waters through complexation and charge neutralization, resulting in the lowest fouling when the ζ potential was ~ 0 mV [63]. This result demonstrates the effects of different destabilization mechanisms in natural and synthetic waters, possibly dependent on the method of aluminum addition and on the colloid and NOM compositions and concentrations. Importantly, the pH value of 6.4 also approximately corresponds to the minimum aluminum solubility and the optimum pH for alum coagulation [115].

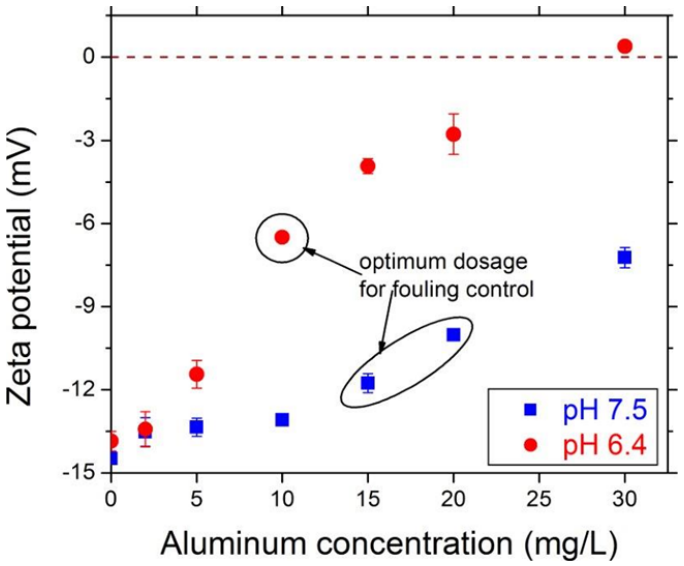

Figure 10. Progressive charge neutralization by increasing aluminum dosage at pH 6.4 and 7.5.

Fouling Worsened with Increasing Transmembrane Pressures

As reported earlier in other MF studies [e.g., 125], fouling worsened at higher pressures (or initial fluxes) at fixed pH and aluminum dosage in our experiments. These results are summarized in Figure 11, which depicts relative flux profiles corresponding to the optimal aluminum dosage for both pH values investigated.

An inverse relationship between normalized fluxes and filtration pressures is consistent with cake compaction, with lower permeabilities of surface deposits measured at higher pressures. As shown in Figure 12, specific cake resistances increased in a power-law manner with pressure for a given aluminum dose.

Compressibility indices generally increased with aluminum dosage, increasing from 0.39 for the raw water to 0.49, 0.61, and 0.68 for aluminum dosages of 5, 10, and 15 mg/L, respectively, at pH 6.4 (Figure 12). A similar trend was also observed at pH 7.5 for electrocoagulated suspensions, with compressibility indices increasing from 0.32 to 0.68 as the aluminum dose increased from 2 to 20 mg/L. This correlation suggests there was a higher degree of transport of fines, floc breakage, and colloid rearrangement as pressure increased, all of which contributed to the overall cake compaction. As expected, the raw-water compressibility index was similar at pH 6.4 and 7.5, but higher than the index for

waters with low aluminum doses at pH 7.5. Compressibility indices in this study varied between 0.3 and 0.8, which is the same range measured during iron electro-coagulation of other natural waters [32, 57, 126], and cakes formed in this research can be classified as being moderately to highly compactible.

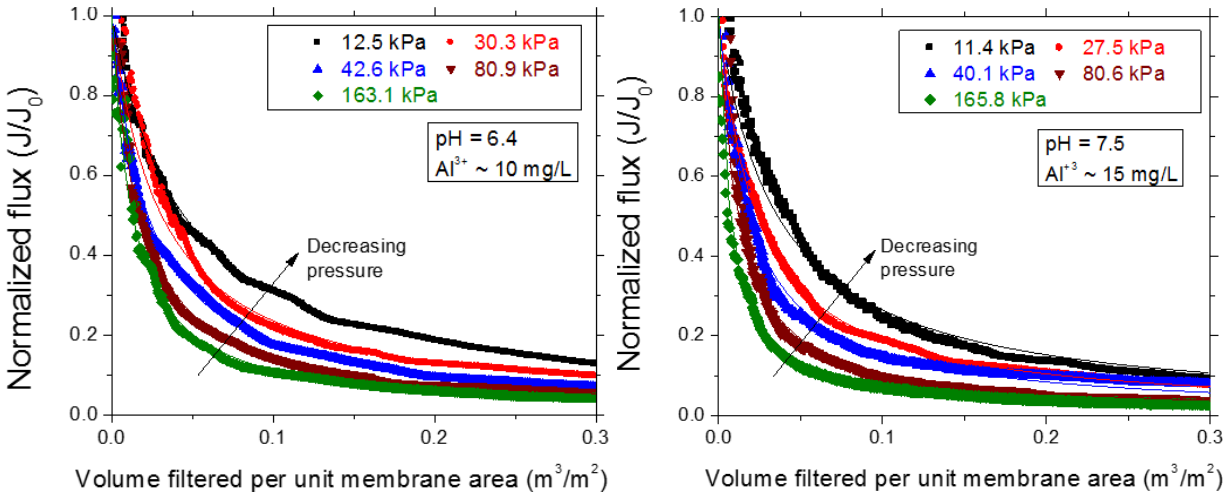

Figure 11. Evidence of cake compaction with lower normalized fluxes observed with increasing pressures at fixed pH and aluminum dose.

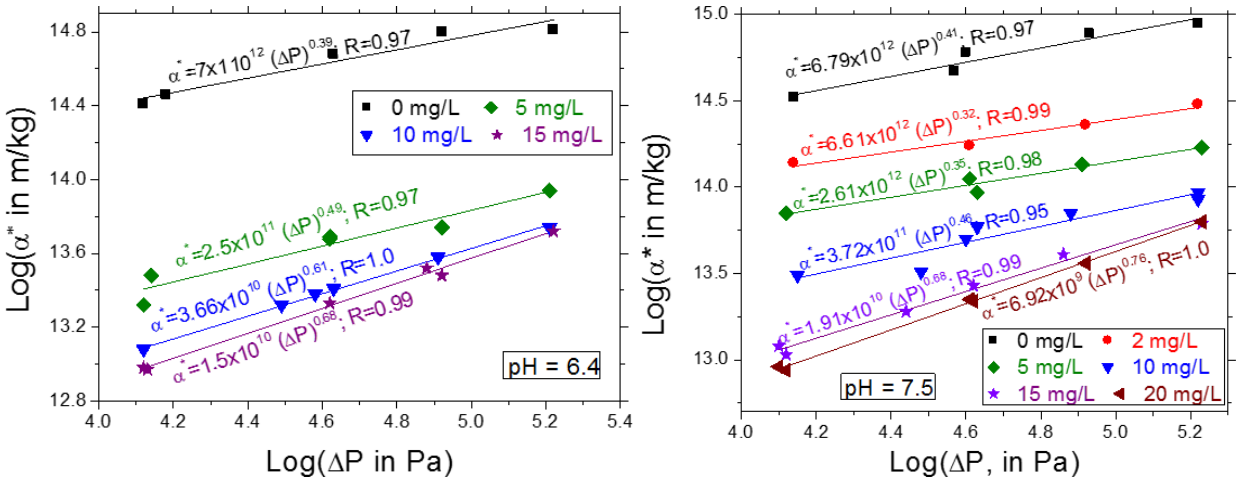

Figure 12. Power law compressibility of colloidal deposits formed on the membrane surface at different coagulant (Al) dosages and pH.

Cake compaction will induce more rapid fouling (pressure increase rate) during constant-flux MF of coagulated suspensions, as is often practiced in full-scale systems [127]. The rapid pressure buildup can only be partially compensated by more frequent backwashing or chemically enhanced backwashes. Therefore, constant flux operation can be expected to eventually reduce the intervals between chemical cleanings, increasing both capital costs (additional membrane area) and operational costs (more cleaning chemicals). Increased fouling in the constant-flux mode has already been reported in the literature even for incompressible

silica particles and untreated surface waters [127, 128]. This finding strongly suggests the benefits of operating microfilters at constant pressure following electrocoagulation pretreatment, especially for higher coagulant concentrations, which correspond to higher compressibility indices. It is also expected to apply qualitatively to membrane bioreactors, since microbial flocs are also compressible. However, since microorganisms exhibit different compression behavior than inorganic particles and flocs (straight-line rather than power-law), separate experiments are necessary to quantitatively assess bioreactor fouling under constant-flux versus constant-pressure operation.

Higher Fluxes Were Observed at a Lower Feed-Water pH

For a given coagulant dosage, fouling was substantially reduced at the lower pH investigated at a low transmembrane pressure, as shown in Figure 13. Improved fluxes at pH 6.4 compared with pH 7.5 were attributed to the formation of more permeable cakes near the pH for minimum aluminum solubility. For example, for the data presented in Figure 13, the specific resistance at 13.8 kPa decreased from 2.9×10^{13} to 9.4×10^{12} as the pH was reduced from 7.5 to 6.4. The lower pH also corresponds to more efficient charge neutralization by $Al(OH)_2^+$. Cake compaction at higher filtration pressures manifests as very similar relative flux profiles regardless of the pH. (See inset of Figure 13.) Note that these results are in contrast to those for iron electrocoagulation, in which sharper fouling was measured at pH 6.4 due to electrolytic generation of soluble Fe^{+2} that formed smaller flocs [32].

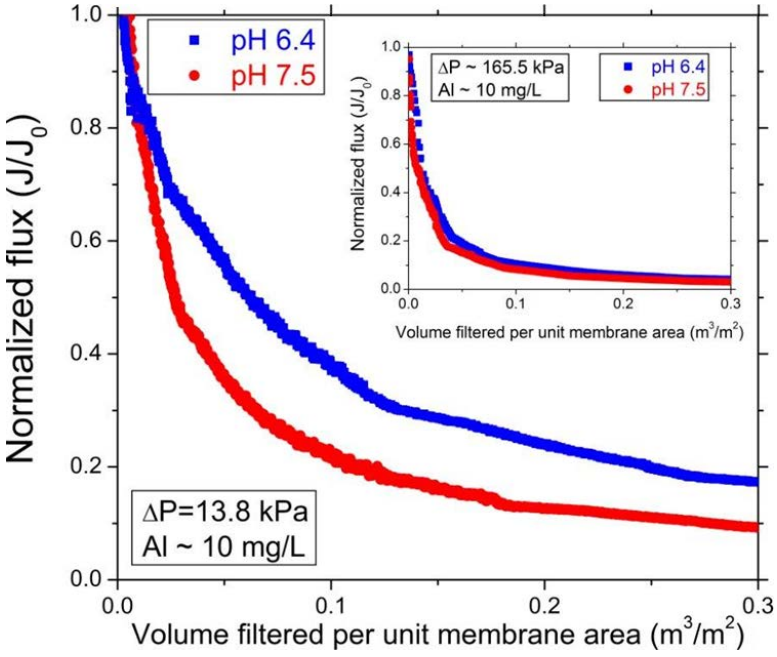

Figure 13. Improved normalized fluxes at pH 6.4 compared with pH 7.5 at a low transmembrane pressure.

At higher pressures, the pH effect is negligible (inset).

Electroflotation Pretreatment to Microfiltration

Elemental Composition of Raw and Pretreated MF Feed Waters

The composition of colloids in the MF feed waters obtained through XPS survey scans and high-resolution core-line spectra are summarized in Table 5. As expected, Al and O dominated in electrochemically "treated" Nanopure water due to $Al(OH)_3$ precipitation, with adventitious carbon contributing about 13 percent to the elemental composition. Note that since samples were dehydrated prior to spectroscopy, "O" refers to solid-phase oxygen rather than to oxygen contained in liquid water.

Table 5. Percentage Atomic Concentrations of Elements in Untreated Raw Water and Electrochemically Treated Suspensions

Sample	C 1s	N 1s	O 1s	Al 2p	Ca 2p	Si 2p	O/Al ratio	C/Al ratio	C/N ratio
Nanopure water (10 mg/L Al)	13.1	- - -	66.7	19.6	- - -	- - -	3.4	0.67	- - -
Raw water (no Al)	51.8	4.9	37.1	0.83	0.42	3.6	44.7	62.4	10.57
Electrocoagulation (10 mg/L Al)	33.3	3.2	50.6	8.8	0.38	2.77	5.9	3.8	10.40
Electroflotation (10 mg/L Al)	27.4	1.6	57.8	12.4	0.30	0.4	4.7	2.2	17.13

The elements C, N, and O in untreated raw water are attributed predominantly to NOM and microorganisms [129, 130]. As expected, the contribution of Al was low, which was verified by the City of Houston. Approximately 4 percent Si was detected, a portion of which was assigned to crystalline SiO_2 (since a sharp peak was detected at $2\Theta = 26.6°$ in the X-ray diffractogram), potentially from quartz and diatoms. (See Figure 21a, later in the report.) Crystalline silica and amorphous silica both are often detected in natural waters [131, 132]. Low amounts of Ca probably arise from $CaSO_4/CaCO_3$ in the shells of microfauna. Trace signatures of Na, Mg, P, S, etc., typical of surface water, were also observed but are not shown in Table 5. Coagulant precipitation in pretreated natural waters increased the Al signal in electrocoagulated and electrofloated aggregates. In these waters, strong C, N, and O signals are again assigned predominantly to NOM and microorganisms (with some degree of adventitious carbon). As can be expected, the C/N ratio was conserved during electro-coagulation (10.4 versus 10.6 for untreated raw water) since the absence of a sedimentation step did not cause NOM removal. In contrast, floc flotation removed a portion of NOM and decreased both C and N; however, there was a net increase in the C/N ratio to 17.1, as the N signal decreased more than the C signal (attributed to adventitious carbon).

Potential chemical functionalities were investigated in more detail using background-subtracted high-resolution O 1s, C 1s, and Al 2p spectra of pretreated

samples, which were curve-fitted using Gaussian/Lorentzian functions (Figure 14). High relative concentrations of Al and O in solids formed in Nanopure water, corresponding to an O/Al ratio → 3 (Table 5), indicate the presence of $Al(OH)_3$, which was confirmed by high-resolution analysis of Al 2p and O 1s spectra. First, the Al 2p peak was located at 74.55 eV, the value reported for Al in pure $Al(OH)_3$ [133]. Secondly, the –OH component of the O 1s peak at 532.2 eV composed 89 percent of O (the remaining 11 percent corresponding to adventitious water at 533.6 eV). Thus, this –OH component accounted for 59.4 of the 66.7 percent oxygen reported in Table 5. This was three times the atomic percentage reported for Al (19.6), resulting in a stoichiometric Al:OH ratio of 1:3, thereby proving the dominance of $Al(OH)_3$ rather than oxides or oxy-hydroxides [133, 134]. Further, X-ray diffraction analysis confirmed the amorphous nature of these precipitates, as reported earlier [37, 121].

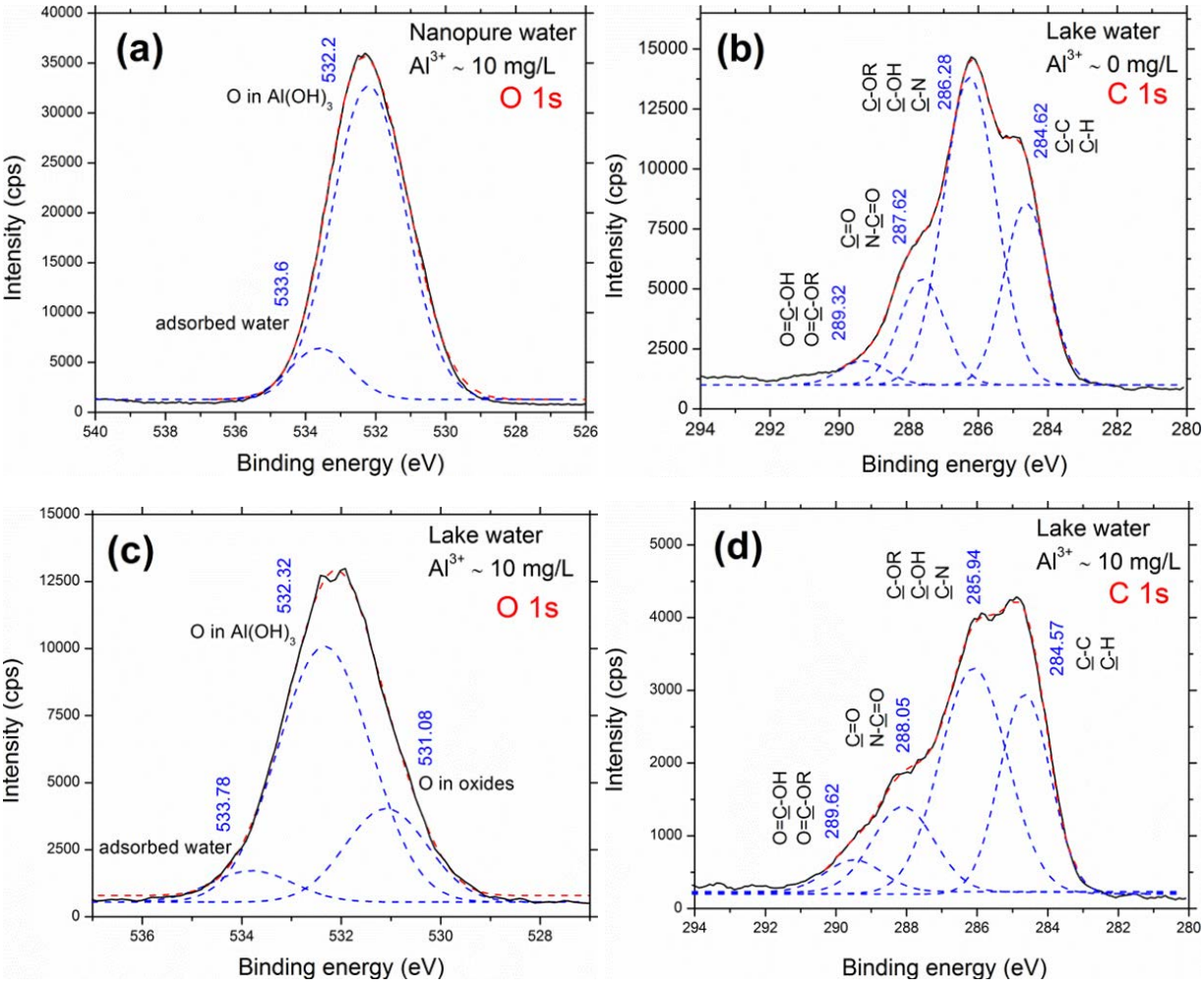

Figure 14. High-resolution XPS spectra of flocs formed during electroflotation.

Panel (a) is for oxygen in precipitates formed in Nanopure water; (b) carbon in untreated raw water; (c) oxygen in pretreated raw water flocs; and (d) carbon in pretreated raw water flocs.

Natural organic and inorganic sources of oxygen increased the O/Al ratio in aggregates formed during electrocoagulation and electroflotation of surface water (5.9 and 4.7 respectively). These values are markedly higher than that of $Al(OH)_3$ formed in Nanopure water (O/Al = 3.4). The O 1s peak (Figure 14c) was decomposed into:

(i) A peak at 531.08 eV primarily due to bulk hydroxyl groups from $Al(OH)_3$ but also possibly from O–(C, H), including hydroxide, acetal, and hemiacetal;

(ii) Contributions from inorganic oxides such as Al_2O_3 and SiO_2 as well as carbonyl moieties (O=C in NOM) as in carboxylate, ester, or amide at 532.32 eV; and

(iii) Adventitious water and/or esters at 533.78 eV.

These indicate the presence of carbohydrates, humic and fulvic acids, proteins and other components present in NOM [130]. The high O/Al ratio in untreated raw water (≈ 45) is due to the predominance of O from NOM and the very low Al concentration (only 0.12 mg/L measured through inductively coupled plasma mass spectrometry).

The C 1s core level peak in electrochemically treated waters was resolved to four components (Figure 14d):

(i) Aromatic and aliphatic C–C or C–H at 284.57 eV;

(ii) A peak at 285.94 eV attributed to alcohols, ethers, or amines;

(iii) Carbonyl or amide groups at 288.05 eV; and

(iv) Carboxylates, carboxyl acids, or carbamates at 289.62 eV.

The ~0.5-eV peak shifts for treated waters compared with raw water reveals changes to the electronic environment of C in the presence of $Al(OH)_3$ indicating NOM sorption on flocs [135].

In summary, XPS revealed that:

(i) Amorphous $Al(OH)_3$ and NOM are the major MF foulants in feed waters after both electrocoagulation and electroflotation pretreatment,

(ii) Electroflotation removed a fraction of the NOM by sorption/ enmeshment onto $Al(OH)_3$, and

(iii) There was no evidence of NOM oxidation during electrolysis since the relative intensities of the C 1s peaks at 285.94, 288.05, and 289.62 eV (corresponding to O=C and O–C) remained constant.

Colloid Destabilization

The magnitude of the ζ potential decreased (i.e., became less negative) with an increasing Al dose up to an intermediate value (20 mg/L in Figure 15), but maintained a relatively constant positive charge at higher dosages [17, 37]. As reported earlier for conventional chemical coagulation [2], charge neutralization

of colloids occurs at an optimum Al dose corresponding to the lowest fouling, due to the adsorption of $Al(OH)^{2+}$ (the dominant hydrolysis species at pH 6.4). Note that we obtained a different result for electrocoagulation of Lake Houston water [37], for which we reported sweep flocculation as the dominant destabilization mechanism. Hence, surface properties or concentrations of natural colloids appear to have changed over time in the source water. This points the need for frequent empirical evaluation of the optimal electrocoagulant dose, similar to jar testing for conventional chemical coagulation. Figure 15 illustrates that, over the range of electrocoagulant dosages studied, particles were destabilized through a combination of double-layer compression, charge neutralization, and sweep flocculation.

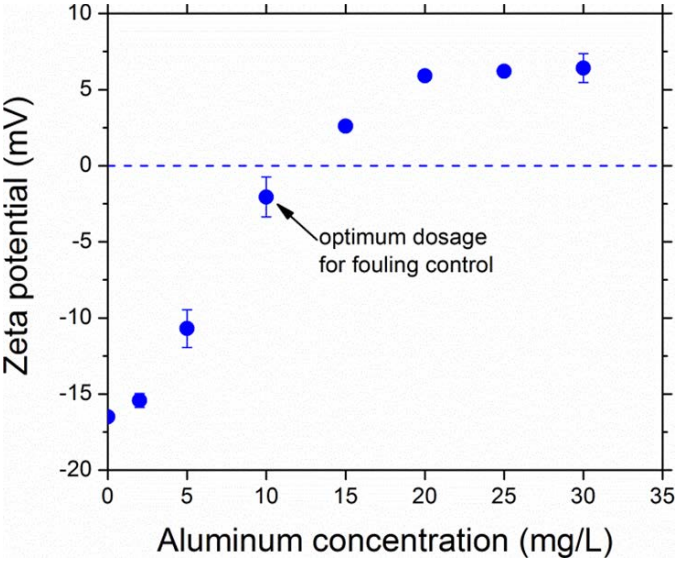

Figure 15. Floc surface charge was near neutral at the optimum electro-coagulant dose.

Particle Size

Optical images of raw-water colloids and flocs formed in electrocoagulation and electroflotation were used to calculate the particles' area-weighted effective diameter. As summarized in Figure 16, the mean particle size in electrofloated MF-feed suspensions increased up to an intermediate aluminum dosage (10 mg/L) and remained relatively constant for Al ≥ 10 mg/L. In contrast, floc sizes increased monotonically with electrocoagulant dose. Also, MF feed waters following electrocoagulation and electroflotation pretreatment were similar in size and mass concentration for low doses (≤ 5 mg/L) before significant bubble formation. Greater aluminum dosages, corresponding to longer durations of electrolysis, facilitated floc flotation, which reduced the size (and mass concentration) of colloids in the MF feed water pretreated with electroflotation compared with electrocoagulation. Note that smaller colloids also experience a lower collision frequency with hydrogen bubbles. Hence, under our experimental conditions the saturation hydrogen concentration was exceeded, a sufficient number hydrogen bubbles necessary for floatation were released from the

cathode, and the threshold aggregate size for an adequate number of collisions was obtained for dosages greater than ~5 mg Al/L.

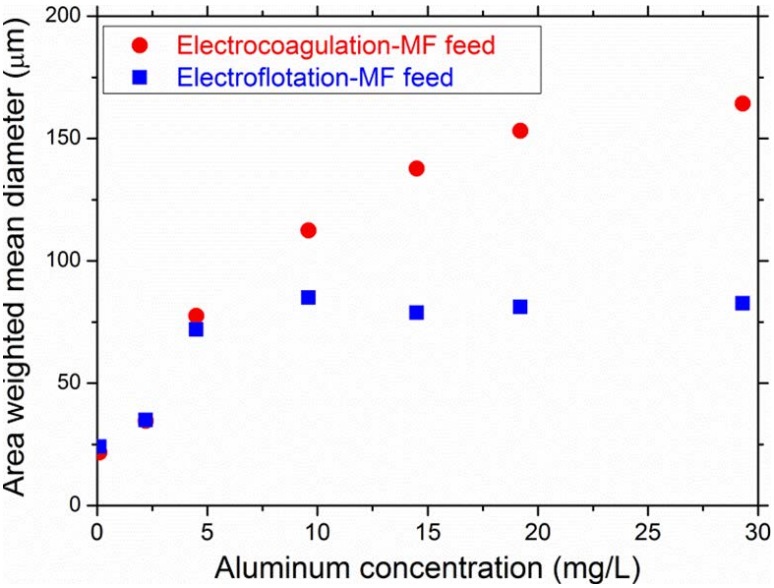

Figure 16. Area weighted mean particle diameters of electrocoagulated and electrofloated flocs measured with light microscopy.

Fractal Dimensions/Scattering Exponents

Three trends can be observed in Figure 17, which summarizes the scattering exponents (fractal dimensions) of the pretreated colloids in MF feed waters. First, as expected, the 3D fractal dimensions measured by static light scattering were always higher than the corresponding 2D values measured by box counting. Secondly, fractal dimensions of electrocoagulated and electrofloated flocs were almost identical (both $d_{f,2D}$ and $d_{f,3D}$), revealing that the structure of the colloidal foulants reaching the membrane surface was similar for any given set of pretreatment conditions. Finally, more loosely packed aggregates were formed, evidenced by decreasing $d_{f,2D}$ and $d_{f,3D}$ [58] with increasing Al dose up to ~15 mg/L, after which fractal dimensions remained relatively constant. Reductions in the fractal dimension with increasing addition of aluminum (0–15 mg/L) is attributed to progressive neutralization of the colloidal surface charge (as shown in Figure 15) and increasing attachment efficiency. Higher Al dosages (≥15 mg/L) did not significantly influence aggregate morphology because sweep flocculation dominated and the ζ potentials remained constant. Mass fractal dimensions ($d_{f,3D}$) changed from 2.6 to 2.0, which agrees with values reported for polydispersed suspensions [108, 136]. The values at the upper end of this range correspond to particle-particle and particle-cluster interactions with a high-energy barrier before effective charge neutralization. Cluster-cluster interactions dominated aggregation for higher dosages during sweep flocculation [108].

In summary, the surface charge and structure of colloidal aggregates in electro-coagulated and electrofloated waters were similar. The removal of larger floating aggregates during electroflotation pretreatment resulted in smaller colloids in MF

feed waters and decreased mass loading to the microfilter. The O/Al ratio of 4.7 in in the effluent from electroflotation was closer to the stoichiometric value of 3 in $Al(OH)_3$ compared withthan was the ratio in the electrocoagulation effluent (5.9), suggesting the relative dominance of $Al(OH)_3$ colloids following electroflotation pretreatment. Moreover, the C/Al ratio was lower in following electroflotation, indicating that flocs in the effluent of this pretreatment process were enriched in Al relative to NOM. These physicochemical differences in the microfilter feed water following electrocoagulation and electroflotation can be expected to cause dissimilar fouling, which is reported next.

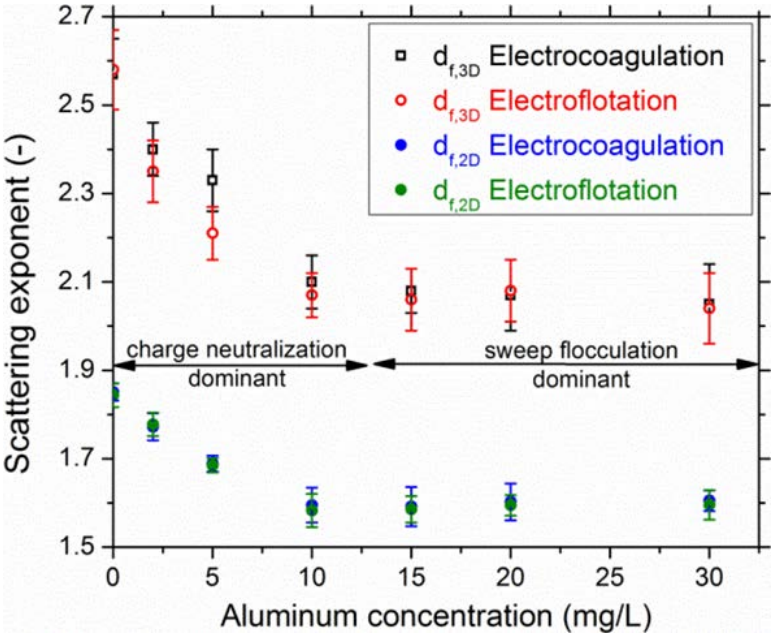

Figure 17. 2D and 3D fractal dimensions decrease with increasing electro-coagulant dosage.

Improvements in Microfilter Flux Following Electroflotation Pretreatment

As shown in Figure 18a, the untreated surface water severely fouled the microfilter, causing more than 90 percent reduction in flux by the time 100 L/m^2 had been filtered (i.e., within 20 minutes). Electroflotation pretreatment significantly improved fluxes with increased Al dosage up to 10 mg/L. Interestingly, increasing Al dosage beyond the optimal value reduced the flux and yielded overlapping, virtually identical profiles for all higher Al concentrations evaluated (15, 20, and 30 mg/L). The flux improvement with increasing Al dose up to the optimal value is due to the combined effects of (i) increasing particle size (Figure 16), (ii) formation of more permeable aggregates (Figure 17), and (iii) reduced cake mass (to be discussed in the following section). The overlapping of all flux profiles for Al $\geq$ 15 mg/L is attributed to very similar feed water characteristics, including aggregate size, fractal dimension, and cake mass. Raw-water fouling profiles exhibited an initial intermediate blocking period followed by cake filtration as revealed by empirical fits to constant-pressure blocking laws [137–139]. In contrast, the entire fouling profiles for pretreated

waters were quantitatively modeled solely by cake filtration, potentially due to the higher mass loading and larger sizes of feed water colloids [137]. Figure 18b shows that fouling was exacerbated by increasing the transmembrane pressure for pretreatment at the optimal dosage due to compaction of the aggregated natural colloidal materials composing the cake [37, 137].

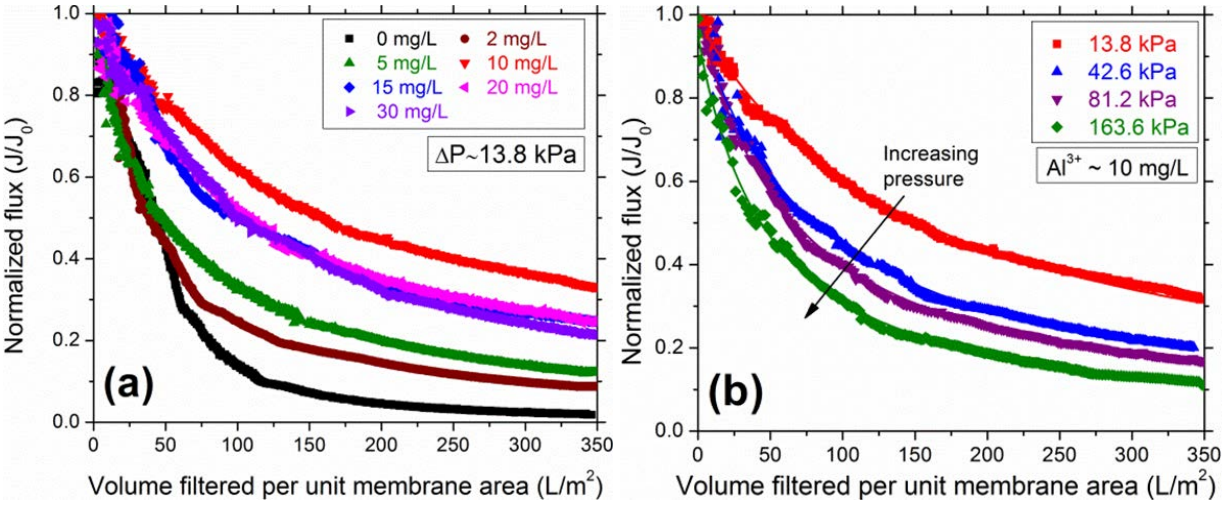

Figure 18. Effects of aluminum dosage and increasing pressure on relative permeate flux during microfiltration following electroflotation pretreatment.

(a) At a constant transmembrane pressure of 13.8 kPa, flux improves only up to an intermediate Al dosage (10 mg/L) and declines at higher dosages. (b) At the optimal Al dosage of 10 mg/L, fouling worsens with increasing pressure.

Comparison of Electroflotation and Electrocoagulation Pretreatment

Effects of Operating Conditions on Flux Profiles

Representative flux profiles comparing electrocoagulation and electroflotation are presented in Figure 19. Under our experimental conditions, the two pretreatment techniques both worked optimally to control MF fouling at the same Al dosage (10 mg/L). Both pretreatment methods resulted in nearly identical permeate fluxes below the optimal Al dosage (e.g., Figure 19a). This is a direct consequence of their similar effluent water characteristics prior to significant bubble formation during electrolysis, as reported in the earlier section “Elemental Composition of Raw and Pretreated MF Feed Waters.” Importantly, electroflotation pretreatment resulted in higher fluxes at or beyond the optimal Al dosage, once the threshold number of bubbles was released (Figure 19b, c, and d). The properties of the membrane cake layer were analyzed in more detail to mechanistically understand why electroflotation outperformed electrocoagulation. Note that electrocoagulation was obtained simply by gently and thoroughly mixing the entire suspension and using it as the feed water. In contrast, for electroflotation, the feed water was taken out from the bottom of the cell, thereby avoiding filtration of the floated flocs.

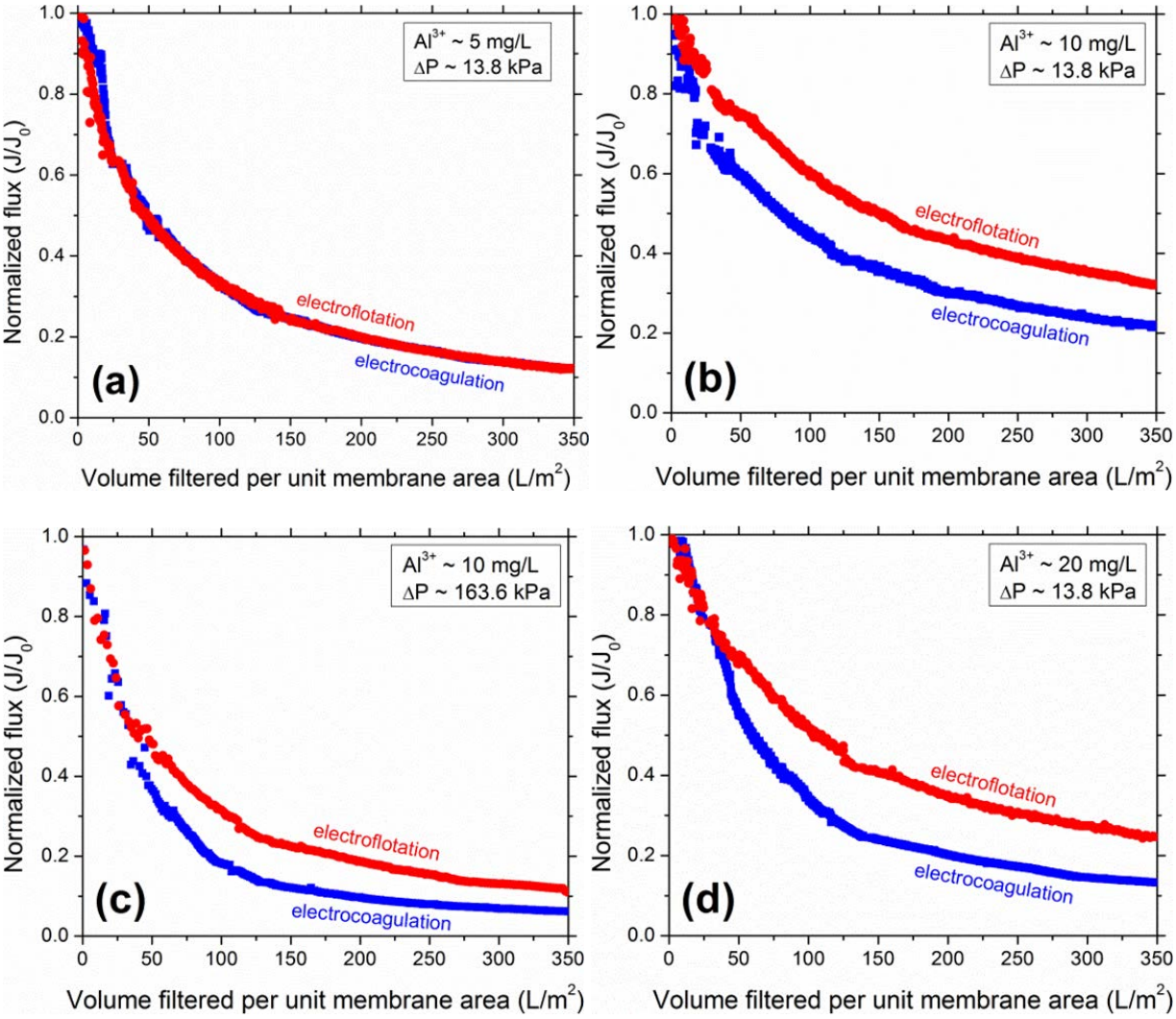

Figure 19. Comparison of instantaneous normalized fluxes following electrocoagulation and electroflotation pretreatment at different operating conditions.

(a) 13.8 kPa, 5 mg Al/L; (b) 13.8 kPa, 10 mg Al/L; (c) 163.6 kPa, 10 mg Al/L; and (d) 13.8 kPa, 20 mg Al/L.

Cake Resistances and Compression

Increasing transmembrane pressure caused greater fouling due to cake compaction [37, 137, 140], as observed in Figure 18b and in the corresponding profiles in Figures 19b and c . The compressibility index increased from raw water (0.48), to electroflotation pretreatment (0.59), and to electrocoagulated colloids (0.74). This trend suggests a higher extent of aggregate breakage and the rearrangement of primary particles for electrocoagulation pretreatment than for electroflotation, presumably due to the higher floc size.

Similar fouling profiles for less-than-optimal Al dosages (0, 2, and 5 mg/L in Figure 19a) translated to statistically similar total and specific cake resistances for both pretreatment processes (Figure 20). Under these conditions, bubble

formation was insignificant and the associated particle removal by flotation was negligible. This resulted in nearly identical cumulative cake masses (three overlapping data points in the lower right inset in Figure 20). Hence, the corresponding specific cake resistances were also indistinguishable between electrocoagulation and electroflotation (upper left inset in Figure 20). Higher fluxes measured for electroflotation pretreatment at Al ≥ 10 mg/L (e.g. Figures 19b, c, and d) implied lower cumulative cake resistances for this pretreatment method. Longer electrolysis durations facilitated particle removal by flotation, and hydrogen bubble evolution significantly reduced total mass loading onto the microfilter. As seen in the lower right inset of Figure 20, the cake mass increased monotonically with dose for electrocoagulation, whereas it reached a relatively constant and lower value for electroflotation beyond the optimal dosage. Even though electroflotation with Al ≥ 10 mg/L reduced cake mass, it increased the specific resistance relative to electrocoagulation, since it produced smaller particles (Figure 16). Conversely, the formation of larger particles and associated lower specific resistances by electrocoagulation was counteracted by the disproportionately higher mass of colloidal matter filtered by the membrane (i.e., higher cumulative resistance).

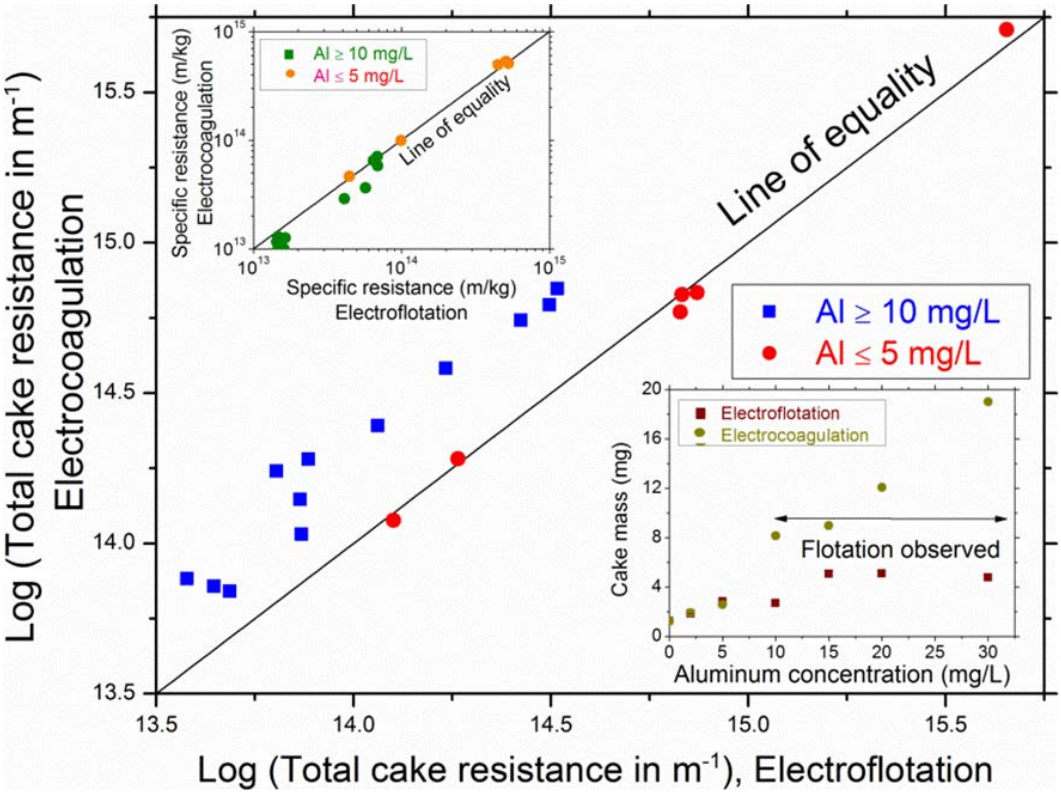

Figure 20. Comparison of electrocoagulation and electroflotation in terms of total cake resistance, specific cake resistance, and cake mass.

Scanning electron micrographs of membranes fouled with raw water (Figure 21a) revealed that natural colloidal matter was highly heterogeneous. Diatoms were observed, which contributed to the Si signal obtained in both XRD and XPS

measurements. (See section above, “Elemental Composition of Raw and Pretreated MF Feed Waters.”) Electrocoagulation pretreatment produced a thick cake layer of amorphous $Al(OH)_3$ flocs, which appeared to have enveloped the particles present in raw water (Figure 21b). In contrast, a very thin cake layer was visualized for electroflotation pretreatment, which also easily peeled off following the dehydration that was necessary for electron microscopy (Figure 21c).

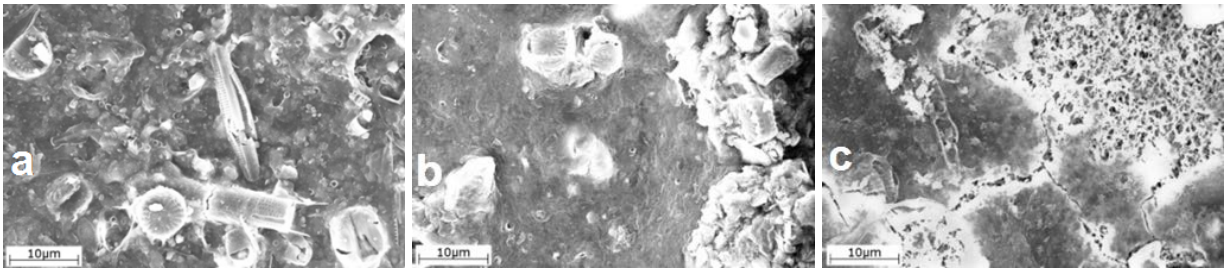

Figure 21. Scanning electron micrographs of fouled membranes.

Membranes are represented: (a) after filtering 150 mL of untreated Lake Houston water, (b) after filtering 150 mL of 10 mg/L electrocoagulated water, and (c) after filtering 150 mL of 10 mg/L electrofloated water.

Evidence of a slightly higher degree of irreversible fouling after electro-coagulation pretreatment

XPS was performed on clean membranes and on membranes that were used to filter waters pretreated by electrocoagulation and electroflotation (Table 6). Note that XPS was conducted on the fouled membranes only after removing the cake, which easily peeled off following overnight drying at a low temperature of 35 °C.

Table 6. Relative Percentage Elemental Concentrations Detected in Clean Membranes and Fouled Membranes after Removing the Cake Layer

Membrane	C 1s	N 1s	O 1s	F 1s	Al 2p	Si 2p	O/Al ratio	C/Al ratio
Clean	57.7	- - -	13.5	28.8	- - -	- - -	- - -	- - -
Fouled following electrocoagulation	50.7	1.6	22.5	21.2	3.4	0.61	6.2	14.9
Fouled following electroflotation	48.7	- - -	18.9	29.2	3.1	- - -	6.1	15.7

In all cases, the major components were C, O, and F where F and a majority of C were attributed to the PVDF polymer constituting the filters. The increasing oxygen fraction in fouled membranes after both types of pretreatment was attributed to $Al(OH)_3$ and NOM. The appearance of N and Si only in membranes that filtered electrocoagulated water suggests that NOM and silica contributed to irreversible fouling. Notably, the absence of N and Si in membranes after electro-flotation indicates that this pretreatment technique effectively reduced irreversible organic and silica fouling. As revealed in Figure 21c, the exposed membrane (after the cake easily peeled off after low-temperature sample dehydration) resembled the clean membrane, which suggests largely reversible binding

between the colloids and the membrane after electroflotation. A greater degree of irreversible fouling after electrocoagulation is attributed to the higher NOM concentrations. Since electroflotation removed a fraction of the NOM present in the raw water (due to the intermediate particle removal/flotation step) the cake was bound less strongly to the membrane, thus facilitating its removal. Even though more $Al(OH)_3$ relative to NOM was transferred to MF in electroflotation, Table 6 reveals that the O/Al ratio and the amount of Al present on the membrane were conserved in both pretreatment processes. The remaining Al is attributed to colloidal $Al(OH)_3$ irreversibly bound to the fouled membranes after filtration of pretreated waters.

Irreversible Fouling Mechanisms During Membrane Backwashing

Foulants Accumulated with Repeated Filtration/Regeneration Cycling and (Ir)Reversible Fouling Was Reduced by Electroflotation Pretreatment

Flux Profiles

Instantaneous flux profiles over five filtration/regeneration cycles for MF of raw and electrofloated Lake Houston water are shown in Figures 22a and b, respectively, from which two major trends are discerned. First, electroflotation well controlled flux decline during forward filtration; e.g., the loss in productivity was only 58 percent during the first cycle (J/J_o from 1 to 0.42 in Figure 22b), compared with a 93-percent decrease for raw water (J/J_o from 1 to 0.07 in Figure 22a). We have recently shown this effect of electroflotation to be due to the formation of larger flocs with low fractal dimension and relatively low colloidal mass loading to MF, which decreases pore penetration and cumulative and specific cake resistances [44]. Therefore, it will not be discussed further herein. Secondly, productivity progressively declined with cycling, suggesting an increasing irreversible accumulation of foulants, which is the focus of this manuscript. The overall permeability after regeneration decreased more drastically for membranes filtering the untreated water, for which 80 percent of the virgin membrane flux was recovered after cycle 1 but only 47 percent after cycle 5. Importantly, electroflotation pretreatment enhanced physical regeneration, resulting in recovery of 93 percent of the virgin membrane flux after cycle 1 and 69 percent after cycle 5 (Figure 22b).

Foulant Elemental Concentrations

XPS survey scans detected negligible amounts of fluorine in the feed waters (0.04 percent in raw water and none in electrofloated water). However, as depicted in Figures 23a and b, a strong F signal was detected from all membranes, indicating that the foulant layer after regeneration was thinner than the XPS sampling depth (~1–25 nm) [142]. It is emphasized this figure represents the thickness of the

foulant layer following physical regeneration, not that of the cake formed during forward filtration. Therefore, XPS profiled the entire foulant layer after physical regeneration in all cases. Moreover, the coefficient of variation for atomic concentrations at different locations was < 20 percent for all elements, demonstrating relatively uniform foulant deposition throughout the membrane surface. The attenuation of the F signal upon foulant deposition was used to calculate and correct for virgin membrane contributions to C and O atomic concentrations on fouled membrane surfaces. Adjustments were not necessary for N, Si, and Al, as they were absent from the virgin membrane.

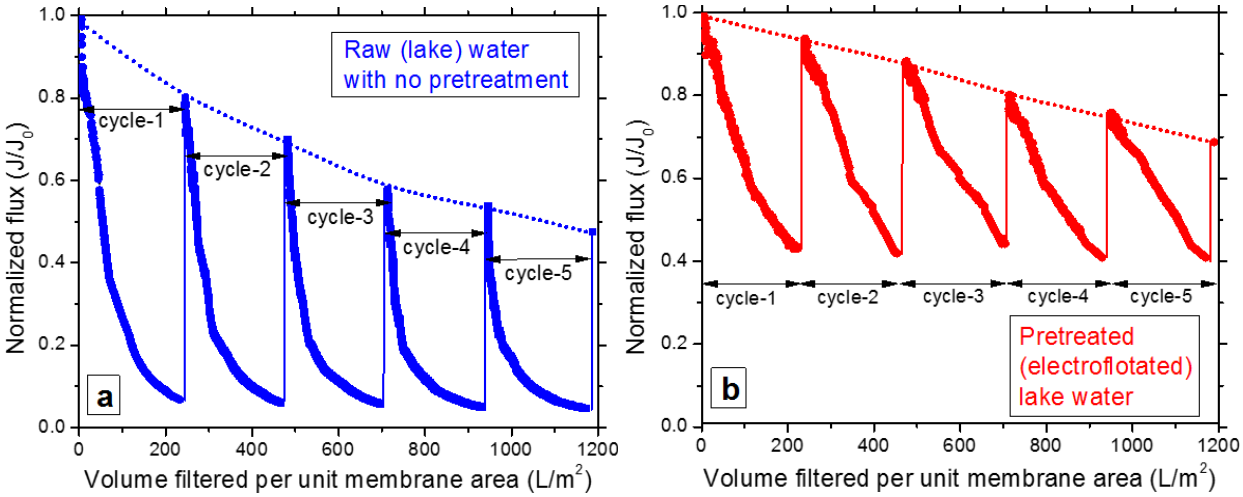

Figure 22. Instantaneous flux profiles over five filtration and hydraulic regeneration cycles for (a) raw (untreated) water and (b) pretreated (electrofloated) Lake Houston water.

The dotted line denotes irreversible fouling. Initial flux J_0 = 910±15 L m^{-2} hr^{-1}.

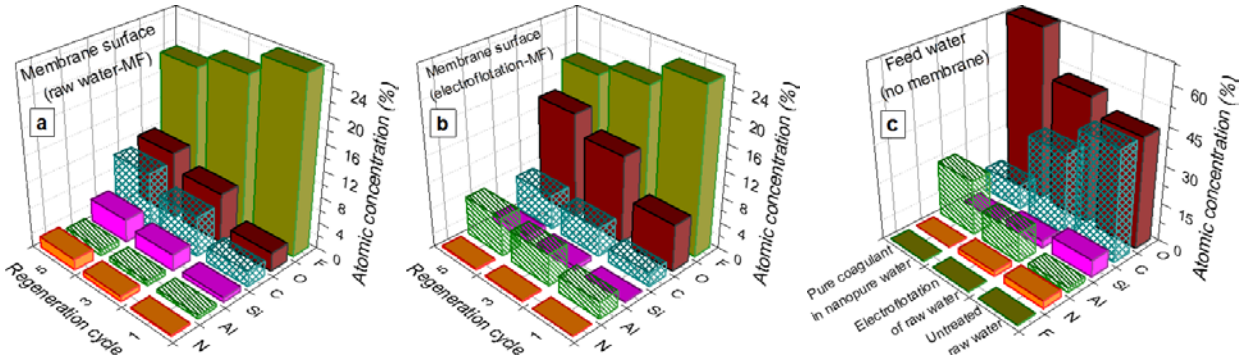

Figure 23. Atomic concentrations on microfilter surfaces compared to concentrations in MF feed water.

(a) Increasing Al, O, C, N, and Si and decreasing F on the microfilter surface over multiple filtration and regeneration cycles for raw Lake Houston water. (b) Reduced C, N, and Si and concomitant increase of Al and O on the membrane surface following electroflotation pretreatment compared with membranes fouled with raw water. C and O data were adjusted using the attenuation of the F-signal [141]. (c) Concentrations of MF feed water constituents after vacuum drying at 40 °C (raw and after electroflotation) and "pure" coagulant formed by electrolyzing Nanopure water. Note that order in which elements are presented is different in (c) than in (a) and (b) to enhance the readability.

C, O, N, Si, and Al progressively accumulated on the membrane surface with repeated cycling for both untreated and pretreated feed waters, as seen in Figures 23a and b, respectively. For raw-water MF, the dominant irreversible elemental foulants were O and C, followed by Si, N, and Al (Figure 23a), whereas for pretreated waters O, Al, and C were dominant, and Si and N played only minor roles (Figure 23b). Also as seen in Figures 23a and b, introducing pretreatment increased the irreversible accumulation of Al and O but decreased C, N, and Si concentrations on membrane surfaces, compared with the results of filtering untreated raw water. The marked increase in Al and O atomic concentrations on regenerated membrane surfaces that had filtered pretreated water, compared with those that filtered untreated water, signifies the accumulation of $Al(OH)_{3(s)}$ generated during electroflotation pretreatment (O was approximately 3× higher than Al on pretreated membranes [44]). Similar results had been reported earlier for polyaluminum chloride coagulation [102]. This contribution from $Al(OH)_{3(s)}$ was confirmed by analyzing Al in the solutions used to clean the membranes, which showed >10× greater Al accumulation after cycle 5 for the membranes used with electroflotation pretreatment (0.012 mg/cm^2) compared to those used with untreated raw water (0.001 mg/cm^2). Further, pretreatment shifted the particle size distribution of the raw-water colloids towards greater sizes. Hence, significant improvements in flux after physical regeneration, despite considerable accumulation of coagulant, are attributed to reduced pore penetration following electroflotation pretreatment [44].

Si and N atomic concentrations were below detection limits for “pure” coagulant generated in Nanopure water but increased to 2.90 and 2.02 percent, respectively in electrochemically treated natural water flocs (Figure 23c). Adventitious C contributed 9.68 percent to precipitates generated by electrolyzing Nanopure water. C atomic concentration increased to 32.76 percent in flocs formed in Lake Houston water. These increases signify sorption of siliceous, nitrogenous, and carbonaceous foulants from the source water onto electrochemically generated flocs during pretreatment. Hence, the depletion of Si, N, and C from irreversibly fouled membranes filtering pretreated waters can be explained by their removal during electroflotation, which reduced their feed water concentrations and, subsequently, reduced fouling. For membranes filtering untreated water, surface DOC concentrations determined by analyzing chemical cleaning solutions were 0.011 mg/cm^2 after cycle 1 and 0.068 mg/cm^2 after cycle 5. These reduced to 0.007 mg/cm^2 and 0.038 mg/cm^2, respectively, for membranes filtering electro-floated water, confirming carbon removal during pretreatment. Therefore, the reduction of irreversible fouling by electroflotation pretreatment can be explained by reduced penetration of foulants into membrane pores and by foulant removal by floc flotation before MF (in spite of coagulant accumulation on the membrane). Foulant sorption during electroflotation is discussed below in more detail, in the section “Foulant Removal from Source Water During Electrochemical Pretreatment.”

Foulant Functional Groups

An FTIR spectrum of the untreated source water revealed that the bands for amide I (1700–1600 cm^{-1}) and amide II (1570–1545 cm^{-1}) were weaker than those of carbohydrate-like and siliceous compounds (3750–3300 and 1200–900 cm^{-1}). XPS also measured a lower atomic concentration of N than of Si (Figure 23c). Further, colorimetry revealed lower concentrations of proteins (0.53 mg/L) than carbohydrates (1.17 mg/L). Hence, protein-like substances were less abundant than carbohydrate-like and siliceous substances in Lake Houston water.

IR spectra of membrane surfaces after cycles 1 and 5 revealed that the following band intensities increased from cycle 1 to cycle 5 for membranes irreversibly fouled by raw water:

- Carbohydrates (νO–H, 3750–3300 cm^{-1}; νC–O–C/νC–O, 1200–900 cm^{-1}; νC–O–C, 820–750 cm^{-1}),
- Proteins/amino sugars (νN–H, 3400–3050 cm^{-1}; νC=O/δNH_2, 1650 cm^{-1}; δN–H/νC–N, 1540 cm^{-1}; νC–O–C, 1036 cm^{-1}),
- Humic acids (νC–H, 3050–2800 cm^{-1}; νC=C–C, 1510–1450 cm^{-1}; $\nu(C{=}O)O^-$, 1700–1300 cm^{-1}; νC=O, 1730 cm^{-1}), and
- Silica (νSi–O–H, 3750–3300 cm^{-1}; νSi–O–Si, 1100 cm^{-1}, 800 cm^{-1}, and 780 cm^{-1})

Therefore, as shown previously for a single cycle [45–47, 143], carbohydrate-like, proteinaceous, humic, and siliceous compounds were major irreversible foulants over multiple filtration/regeneration cycles as well. The irreversible accumulation of organic foulants over multiple cycles during MF of raw water was also confirmed by analyzing chemical cleaning solutions (six-fold increase from 0.011±0.005 mg DOC/cm^2 after cycle 1 to 0.068 ± 0.01 mg DOC/cm^2 after cycle 5). For membranes used with electroflotation pretreatment, regions corresponding to O–H (3650–3200 cm^{-1}) and Al–O (850–680 cm^{-1}) stretching vibrations significantly intensified even after cycle 1 compared with the virgin membrane or with membranes fouled by the raw water. The intensity further increased for cycle 5. Analysis of chemical cleaning solutions also showed irreversible Al accumulation over multiple cycles (five-fold increase from 0.002±0.001 mg/cm^2 after cycle 1 to 0.010±0.002 mg/cm^2 after cycle 5). Hence, IR spectra, chemical cleaning, and XPS (Figure 23b) all demonstrate progressive $Al(OH)_{3(s)}$ coagulant accumulation on membranes filtering pretreated water.

Irreversible Fouling During Direct MF of Lake Houston Water (No Pretreatment)

FTIR spectra of membranes filtering untreated and pretreated waters were analyzed in more detail to rigorously identify changes in foulant composition with successive filtration/regeneration. Only spectra from membranes filtering

untreated water are discussed in this section. Spectra for membranes used with electroflotation pretreatment are discussed in the next section.

Hydrophobic Molecules Contribute More to Fouling During Early Stages of Filtration

As seen in Figure 24, the O–H/N–H band at 3650–3300 cm^{-1} was attenuated while the C–H bands maintained their intensity even after cycle 1 (dotted blue line) compared with the virgin membrane (green line). Hence, fouling appears to have been initiated by irreversible binding of less polar (more hydrophobic) compounds, since the O–H/N–H band is an indicator of hydrophilicity [144].

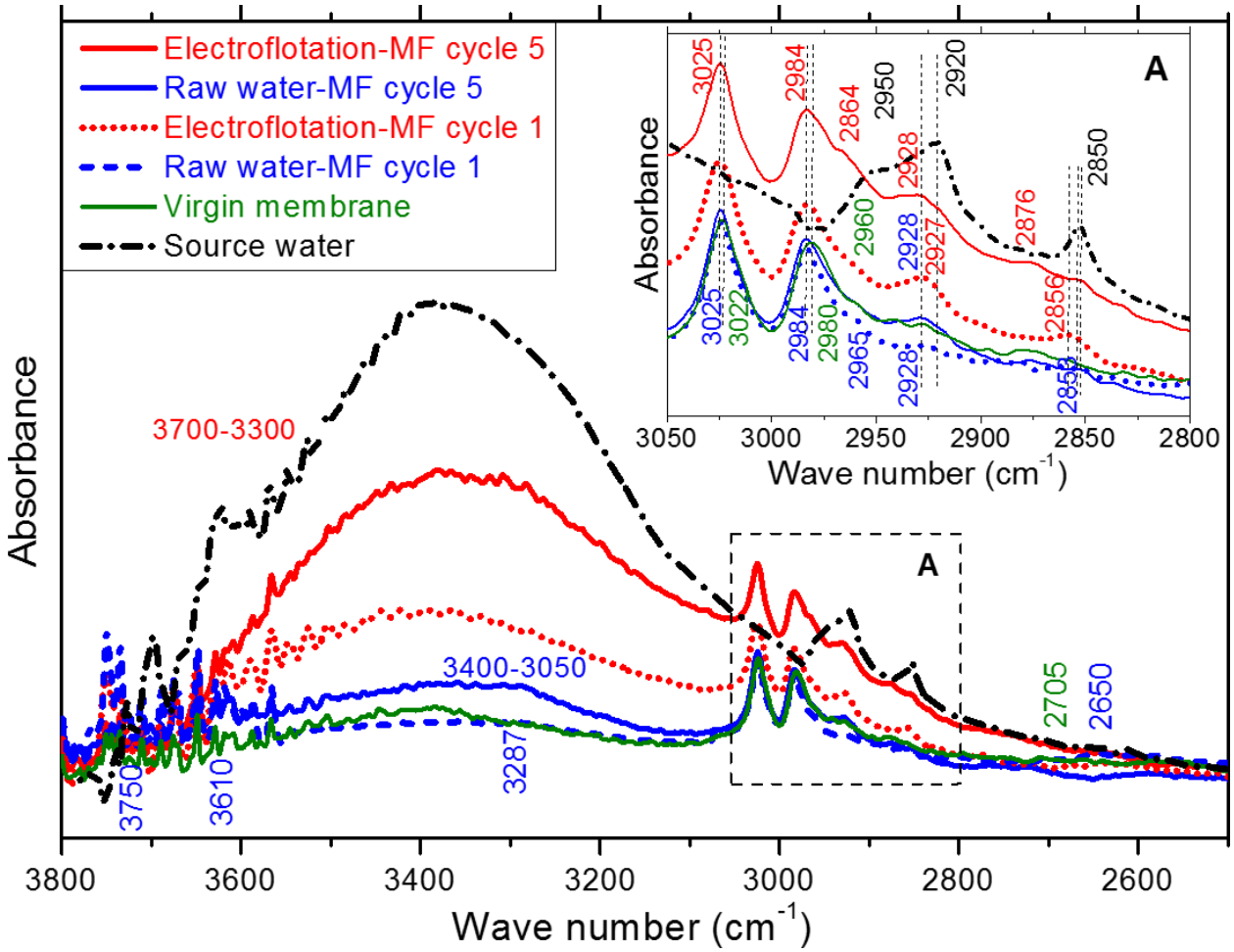

Figure 24. ATR-FTIR spectra of virgin and fouled membranes and untreated Lake Houston water, corresponding to C–H, O–H, and N–H stretching vibrations.

The dashed black line shows the source-water spectrum. All other lines are spectra taken from MF membranes that were either unused (virgin), run for one cycle, or run for five cycles either with pretreatment (electroflotation) or with no pretreatment (raw water). Peaks corresponding to hydrogen bonding: vO-H/vN-H 3760–2625 cm^{-1}. Peaks related to interactions of hydrophobic molecules: vC-H 3050–2800 cm^{-1}.

The spectrum of the wetted virgin membrane surface was subtracted from the spectra of irreversibly fouled membranes to obtain the difference spectra shown in Figure 25. The amide I band (1620–1680 cm^{-1}) after cycle 1 was very weak in the membrane surface difference spectrum (dashed blue line in Figure 25). However, it significantly intensified over extended timeframes, achieving after five cycles (solid blue line in Figure 25) an intensity similar to that measured in untreated Lake Houston water (dotted black line in Figure 25). The occurrence of N–H vibrations (3400–3050 cm^{-1}) more intense than O–H vibrations (3750–3300 cm^{-1}) signifies substantial irreversible binding of protein-like substances with progressive filtration/ regeneration. In contrast, largely reversible binding of carbohydrate-like compounds to the membrane is inferred since they appear to have been effectively removed during regeneration, as evidenced by the substantial weakness of bands for O–H (3750–3300 cm^{-1}) and C–O–C/C–O (1150–970 cm^{-1}) in the membrane difference spectrum, compared with those for the raw water. This weakness may be due to weaker interactions of these bulky molecules [145] with the membrane as a result of steric hindrances. Hence, protein-like substances appear to have accumulated on the membrane to a greater extent than carbohydrate-like substances with respect to their feed-water concentrations. Therefore, as reported recently during UF of natural surface water [49] and model solutions of sodium alginate and bovine serum albumin [146], protein-like substances seem to have played an important role in irreversible fouling of MF membranes, in spite of their lower feed-water concentration. However, since carbohydrates are typically more abundant than proteins in surface water, they are expected to contribute more to fouling on an absolute basis [50].

Hydrophilic Molecules and NOM Complexation Determine Fouling after Repeated Filtration/Regeneration

In contrast to cycle 1, the O–H/N–H band significantly intensified after cycle 5, becoming even more intense than the C–H bands. Figure 23a also shows increasing O, N, and Si from cycle 1 to cycle 5, suggesting the accumulation of relatively more hydrophilic foulants and siliceous compounds as filtration progressed.

Since NOM-carboxyl groups in surface waters are partially protonated at environmental pH values [144, 147], organic acids in Lake Houston are capable of both inner-sphere and outer-sphere complexation. As expected, the intensity of the 1600–1300 cm^{-1} $C(=O)O^-$ stretching region substantially changed in the difference spectrum of fouled membranes after cycle 5 compared with that of the raw water (Figure 25). The carbonyl band at 1730 cm^{-1} considerably attenuated, whereas both symmetric (1425 cm^{-1}) and asymmetric (1600–1500 cm^{-1}) stretching $C(=O)O^-$ bands simultaneously intensified with respect to the raw-water spectrum, indicating deprotonation of carboxylic groups during foulant-membrane interactions [148, 149]. An increasing $\nu_{as}C(=O)O^-$: $\nu_sC(=O)O^-$ intensity ratio in Figure 25 is symptomatic of ligand exchange interactions of carboxylic groups with metals in untreated water [150]. Hence, polyvalent cations

appear to have mediated bridging [151] and/or chelation [152] between NOM-COOH groups and the fouled membrane surface. Further evidence for bridging/chelation was provided by the separation distance between symmetric and asymmetric stretching bands [150, 152] ($\Delta\nu = \nu_{as}C(=O)O^- - \nu_sC(=O)O^-$) being in the range 75–230 cm^{-1}. Outer-sphere complexation should have also contributed to these observed peak changes since the overall surface charge of colloids was negative [150] (ζ potential = –17 ± 2 mV).

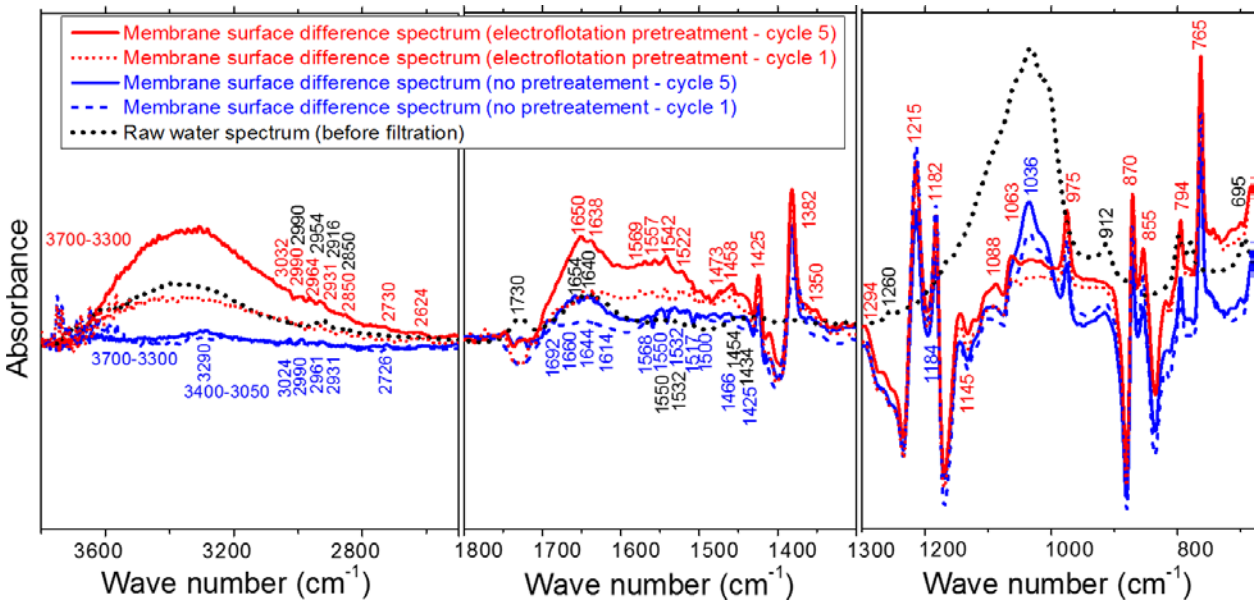

Figure 25. Difference spectra of irreversibly fouled surfaces of membranes used to filter untreated raw water or electroflotation-pretreated water.

The dotted black line shows the source-water spectrum. All other lines are spectra taken from fouled MF membranes that were run for either one or five cycles either with electroflotation or with no pretreatment. Peaks corresponding to complexation interactions: $\nu_{as}(C=O)O^-$ 1650–1500 cm^{-1}, $\nu_s(C=O)O^-$ 1500–1400 cm^{-1}, vC=O 1730 cm^{-1}. Peaks corresponding to hydrogen bonding: vC=O/δNH2 1680–1620 cm^{-1}, δN-H/vC-N 1550–1520 cm^{-1}.

Iron concentrations were very low in the source water, and Fe 2p and Ca 2p signals were absent on fouled membranes. In contrast, aluminum was present in the source water, and the Al 2p signal was observed both in the raw water (Figure 23c) and on irreversibly fouled membranes. Aluminum exhibits greater affinity to organic ligands than calcium [153], and its atomic concentrations on fouled membrane surfaces increased with cycling (Figure 23a). Additionally, calcium was detected in the cake layer spectra [44] but not on surfaces of hydraulically regenerated membranes, suggesting that it was associated with reversible fouling alone through charge neutralization and NOM aggregation rather than through cation bridging [154]. Therefore foulant-membrane bridging is attributed largely to aluminum [153].

Importantly, these spectral changes corresponding to foulant complexation were significantly lower in the difference spectrum of the membrane after cycle 1.

Therefore, these complexes appear to have been formed primarily between foulants in the source water and irreversibly bound foulants on the membrane surface at longer timeframes. This observation may explain the major role of acidic NOM fraction [46, 155] and metal-organic complexes [50] in fouling reported earlier [46]. Bands in this spectral region (1650–1350 cm^{-1}) could also signify minor contributions from non-carboxylic moieties comprising amide II (1570–1545 cm^{-1}), aromatic C=C stretching (1620–1580 cm^{-1}), and C–H deformation (1460–1378 cm^{-1}). Mechanisms of fouling following electroflotation pretreatment of Lake Houston water are discussed next.

Irreversible MF Fouling in Electroflotation-Pretreated Water

Irreversible Accumulation of Both Hydrophilic and Hydrophobic Molecules over the Entire Duration of Filtration

After cycle 1 using pretreated water, both C–H (3050–2800 cm^{-1}) and O–H/N–H (3650–3100 cm^{-1}) bands on the membrane surface intensified compared to the virgin membrane (Figures 24 and 25). Hence, unlike the pattern seen in filtration of untreated source water, fouling appears to have been initiated by both hydrophilic and hydrophobic molecules after electroflotation. Further, more polar foulants, including the $Al(OH)_3$ coagulant and non-proteinaceous organic compounds, accumulated early in the process, as evidenced by the more prominent increase of O–H than of C–H vibrations and by the lack of N and Si detections after cycle 1 (Figure 23b).

Additionally, C–H bands intensified to a smaller extent than O–H bands from cycle 1 to cycle 5 (Figure 24). Therefore, as was the case for untreated water, hydrophilic molecules appear to have accumulated more than hydrophobic foulants with successive filtration/regeneration over longer timeframes. The increased role of hydrophilic foulants during all stages of filtration in pretreated waters is attributed to the efficient removal of hydrophobic molecules by electro-flotation (see next section) and the introduction of hydrophilic $Al(OH)_3$ precipitates. Importantly, higher regenerated fluxes were obtained after every cycle with electroflotation pretreatment even though more coagulant irreversibly accumulated on the membrane.

Mechanisms of irreversible Al accumulation were investigated by electrolyzing Nanopure water at pH 6.4±0.2 to generate the same 10 mg/L Al concentration used for pretreatment of Lake Houston water. Next, the suspension consisting of the "pure" coagulant in Nanopure water was microfiltered and hydraulically regenerated. New asymmetric (1580 cm^{-1}) and symmetric (1470, 1438, 1418 cm^{-1}) $C(=O)O^-$ vibrations appeared in the FTIR spectrum for the membrane fouled by the pure coagulant. The asymmetric vibration was stronger than the symmetric stretching band, indicating ligand exchange interactions [150, 152] between the coagulant and the membrane surface. High-resolution XPS also provided evidence for direct covalent/electrovalent interactions between the pure coagulant and the virgin membrane surface. O 1s component peaks corresponding to

$Al(OH)_{3(s)}$ shifted to lower binding energies (O-I, 530.7→530.4, and O-II, 532→531.8 eV), whereas that of the membrane shifted to higher binding energies (C(=O)OH/C(=O)OR, 531.4→531.8, and C–OR/C–OH, 532.4→532.9 eV). These are attributed to inner or outer sphere complexation of the coagulant [156] with the membrane. Hence, both FTIR and-high resolution XPS provided complementary evidence for coagulant complexation with carboxylate/carboxyl groups on the membrane surface.

Coagulant-Mediated Complexation of Foulants with the Membrane

Asymmetric (1650–1500 cm^{-1}) and symmetric (1500–1400 cm^{-1}) carboxylate stretching bands were significantly intensified in the difference spectrum of the irreversibly fouled microfilter operating on electroflotated water after cycle 1 and cycle 5 (Figure 25). Again, the $\nu_{as}C(=O)O^-$: $\nu_sC(=O)O^-$ intensity ratio increased compared to the raw water spectrum, indicating that flocs complexed with carboxylic/carboxylate groups on the virgin/fouled membrane surface. Further evidence for bridging/ chelation was provided by the separation distance between symmetric and asymmetric $C(=O)O^-$ stretching bands [150, 152] being in the range 120–220 cm^{-1}. Large changes in intensity compared with raw water, even after cycle 1, demonstrate the importance of complexation of acidic functional groups to fouling initiation following pretreatment, unlike initial fouling during MF of untreated water. This complexation could arise from bridging of freely suspended or coagulated foulants mediated by dissolved aluminum hydrolysis products, or from bridging/chelation of the fresh $Al(OH)_3$ precipitates with carboxylic moieties on the virgin membrane surface. As shown in Figure 25, these bands further intensified after cycle 5, demonstrating continued complexation of carboxylic/phenolic groups with fouled membrane components over longer timeframes. The contribution of amide bands to these peak changes is minimal, since only negligible amounts of nitrogen were detected on the membrane surface (Figure 23b). Since electroflotation pretreatment increased the efficiency of hydraulic regeneration (higher flux at the beginning of each cycle compared to untreated water), it appears that complexation predominantly contributed to coagulant accumulation on “inert” areas of the membrane surface with negligible pore penetration.

Changes in the elemental composition and chemical functionalities of irreversibly fouled microfilters operating on pretreated feed waters were rigorously linked to foulant transfer from the raw water to the electrochemically generated coagulant precipitates, as described next.

Foulant Removal from Source Water during Electrochemical Pretreatment

Direct evidence that electroflotation pretreatment decreased concentrations of potential foulants in the feed water and subsequently on the membrane surface (Figure 25) is provided by FTIR (Figure 26) and XPS (Figure 23c) spectra of

electrochemically generated flocs in the MF feed water. Figure 26 shows ATR-FTIR spectra of flocs floated to the water surface (purple line) and unfloated flocs still suspended in the water column (red line), which formed during electrolysis of Lake Houston water. Spectra of untreated surface water (blue line), and "pure" electrocoagulant generated in Nanopure water (green line) are also superposed in Figure 26 to clarify the removal of organic acids, carbohydrates, proteins, and siliceous compounds during electroflotation.

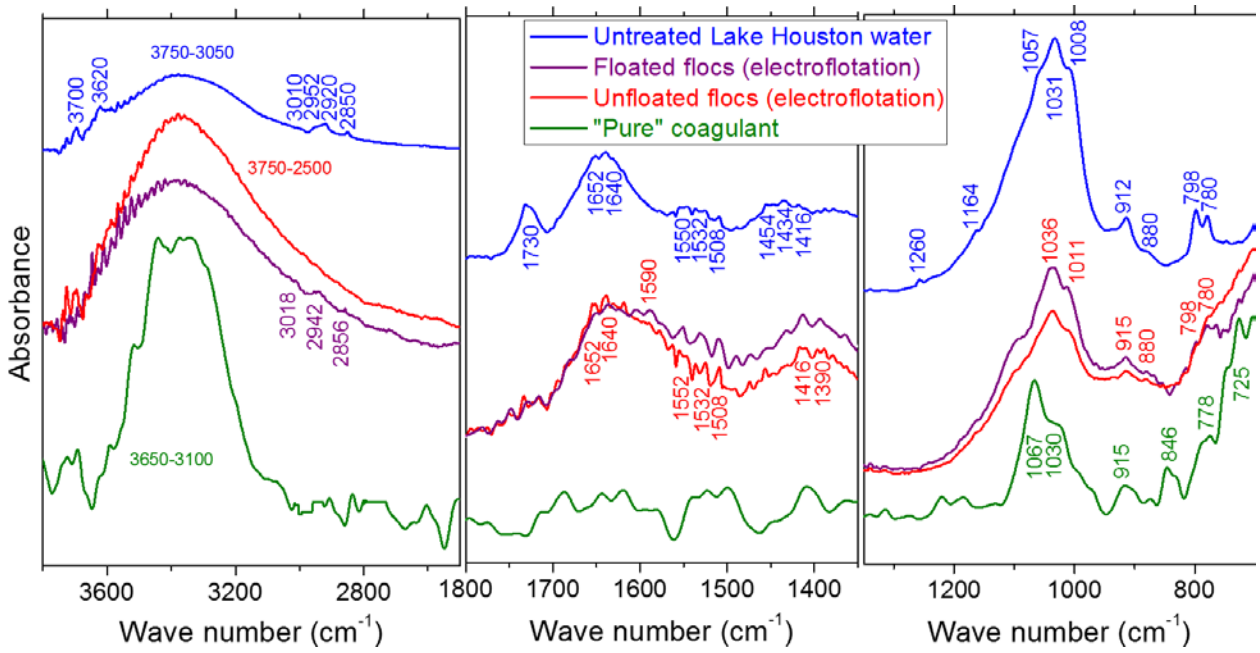

Figure 26. ATR-FTIR spectra of different MF feed suspensions.

The spectrum of the electrofloated flocs collected at the top of the water surface during pretreatment is also shown.

The carbonyl peak of C(=O)OH groups (1730 cm^{-1}) significantly attenuated and the peaks for $\nu_s C(=O)O^-$ (1416 and 1390 cm^{-1}) and $\nu_{as} C(=O)O^-$ (1550, 1532, and 1508 cm^{-1}) intensified in both floated and unfloated flocs, compared to the raw-water spectrum. Additionally, compared to the "pure" coagulant spectrum, symmetric (1480–1350 cm^{-1}) and asymmetric (1600–1500 cm^{-1}) COO^- stretching bands have emerged in the spectrum of electrofloated natural water, indicating NOM-coagulant complexation [135, 148, 157] and demonstrating effective removal of acidic organic molecules from the source water by electroflotation. The C–O, C–O–C, and Si–O bands (1260–840 cm^{-1}) were significantly broader in pretreated Lake Houston water than in the untreated source water (1200–950 cm^{-1}) and the "pure" coagulant (1120–950 cm^{-1}). Similarly, the O–H peak also broadened from 3750–2750 cm^{-1} in the source water and 3640–3125 cm^{-1} in the "pure" coagulant spectra to 3750–2500 cm^{-1} in the spectrum of the electrofloated natural water. This broadening is due to reduced symmetry [157] of these moieties arising from the uptake of carbohydrate-like and siliceous compounds by $Al(OH)_{3(s)}$. Electrochemical treatment of surface water resulted in the appearance

of amide I and amide II bands in the spectra of both floated and unfloated flocs coincident with the appearance of N signals in XPS spectra (Figure 23c). Additionally, the O–H/N–H stretching band broadened compared to its range in the Nanopure water coagulant spectrum (3640–3125 cm^{-1}→3750–3050 cm^{-1}), denoting the effective sorptive removal of proteinaceous compounds. These results show the sorption of carbonaceous, nitrogenous, and siliceous foulants onto $Al(OH)_{3(s)}$ precipitates, and they complement the XPS results (Figure 23c).

Hydrophobic compounds were also removed by electrocoagulation of natural water, as evidenced by increased intensity in the 3050–2800 cm^{-1} region corresponding to C–H stretching bands compared with the spectrum for "pure" coagulant in Nanopure water in Figure 26. Bands at 3018, 2942, and 2856 cm^{-1} were common to raw water and floated flocs, suggesting efficient transfer of hydrophobic molecules to $Al(OH)_3$ precipitates that rose to the top of the electrochemical cell, reducing their carryover to MF and subsequent sorption onto the membrane, thereby increasing flux. This pattern also suggests that hydrogen bubbles were drawn to floc surfaces due to their increased hydrophobicity [158] following sorption of natural water constituents, thereby contributing to floc flotation. In contrast, C–H bands were not distinctly visible in spectra for the unfloated flocs that continued to be suspended in the water column, suggesting that their surfaces were relatively more hydrophilic. The intensification of the O–H/N–H band in the flocs formed in natural water relative to the same band in untreated raw water is due to the contribution from O–H vibrations of $Al(OH)_3$ precipitates (as seen in the significant hydroxyl peak in the "pure" coagulant spectrum). These comparisons demonstrate that electroflotation pretreatment removed several classes of potential foulants present in the surface water, including acidic organic compounds (e.g., fulvic acids), hydrophilic organics (protein-like and carbohydrate-like substances), hydrophobic molecules (e.g., humic substances), and siliceous compounds, thereby reducing their membrane surface concentrations and ultimately controlling fouling.

Substantial amounts of proteins (0.011 mg/mg Al), carbohydrates (0.035 mg/mg Al), and silicon [159] (0.001 mg/mg Al) were found to be sorbed on electrofloated flocs by dissolving the flocs at high pH [160]. Additionally, DOC and specific UV absorbance (SUVA) were reduced by 47 and 20 percent, respectively following electroflotation and MF. In contrast, MF alone reduced DOC and SUVA by only 8 and 2 percent, respectively. These bulk measurements validate FTIR results and show the transfer of foulants from raw water to the flocs, which are removed from the MF feed water by flotation, thereby reducing fouling.

Insights into Cake Compression Mechanisms in Raw and (Electro)Coagulated Pretreated Waters

Electrocoagulation and Alum Coagulation Reduced Fouling to a Greater Extent at Lower Pressures

Instantaneous relative flux profiles for the two coagulant dosages at the lowest (14 kPa) and highest (164 kPa) pressures investigated are shown in Figure 27 for raw (blue), electrocoagulated (red), and alum-coagulated (green) Lake Houston water. As noted previously [40, 51, 161], higher fluxes were obtained following pretreatment, especially at low pressure. The rest of this section focuses on mechanistically explaining the role of pressure and coagulation type in inducing relative differences in fouling through cake compression.

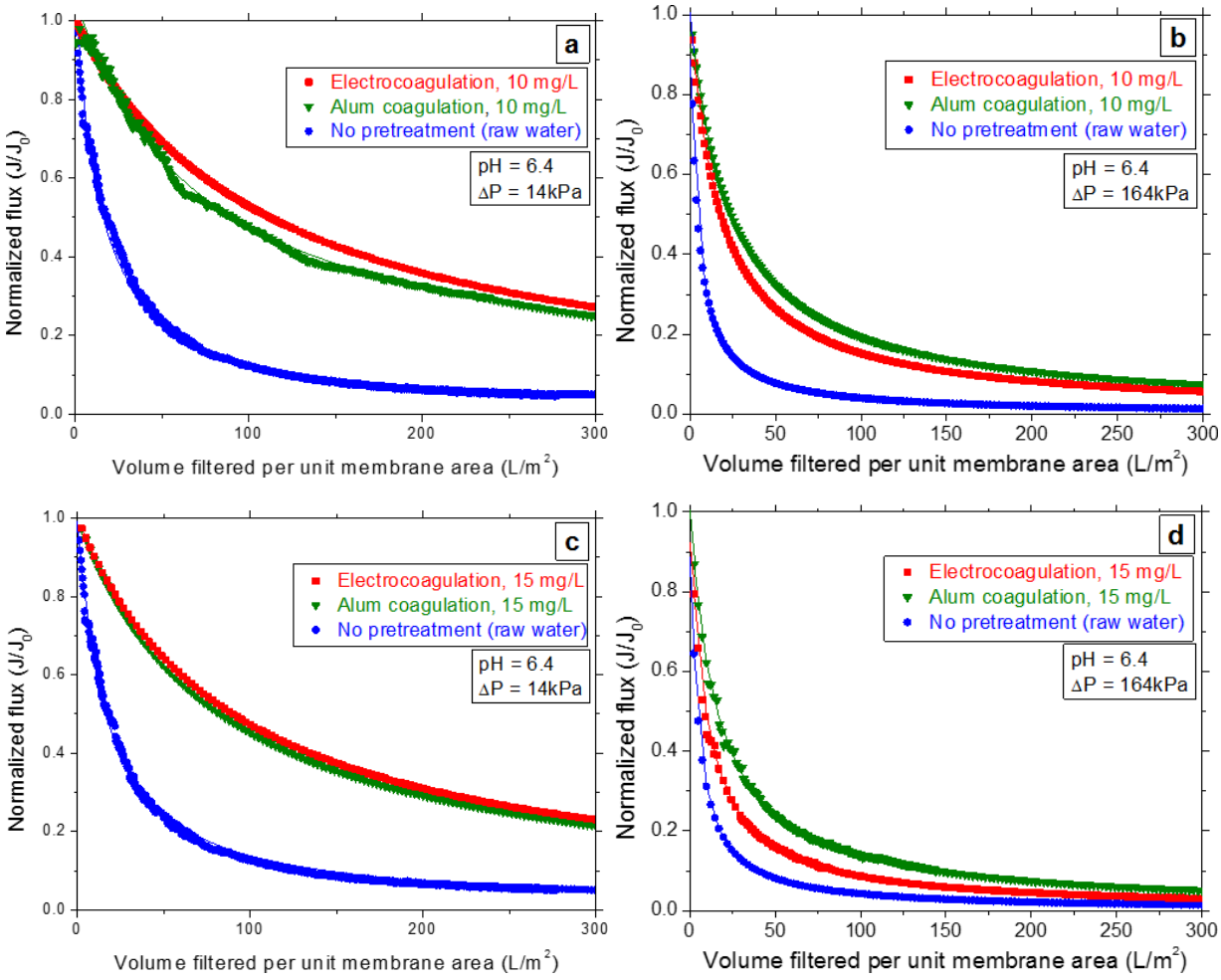

Figure 27. Normalized instantaneous flux profiles corresponding to untreated, electrocoagulated, and alum-coagulated Lake Houston water.

Test conditions represented are: (a) 10 mg/L and 14 kPa, (b) 10 mg/L and 164 kPa, (c) 15 mg/L and 14 kPa, and (d) 15 mg/L and 164 kPa. Corresponding profiles with no pretreatment are also shown. Entire length of each flux profile could be fitted with cake filtration model.

Importantly, fouling was more effectively controlled by electrocoagulation and alum coagulation at lower pressures. At the lowest pressure investigated (14 kPa), fouling was severe for the untreated water — the relative flux decreasing by 95 percent of its initial value at the end of the filtration cycle. Under these conditions, both types of pretreatment improved the pseudo steady-state relative flux substantially, decreasing only by ~75 and ~79 percent at coagulant dosages of 10 mg/L and 15 mg/L respectively (Figures 27a and c). In contrast, pretreatment only negligibly increased the pseudo-steady-state relative flux at the highest pressure investigated. At 164 kPa, the flux declined by 99 percent for raw water, and pretreatment improved it to only ~94 and ~96 percent for the 10- and 15-mg/L coagulant dosages, respectively (Figures 27b and d). Hence, operating at a higher pressure on coagulated waters considerably exacerbated fouling.

Flux Profiles Were Quantitatively Explained by a Compressible Cake Filtration Model

The entire flux profile was quantitatively governed by classical cake filtration theory [40, 56, 58, 59] as evidenced by accurate fits in all cases in Figure 27:

$$\frac{dt}{d(V/A_m)} = \frac{\mu \alpha^* C_b}{\Delta P}\left(\frac{V}{A_m}\right) + \frac{1}{J_0} \tag{5}$$

where t is time, V is cumulative permeate volume, A_m is the effective membrane area, μ is the absolute viscosity, C_b is the bulk particle concentration, and J_0 is the clean-water flux. Straight-line fits to inverse instantaneous flux versus cumulative volume filtered, as given by Equation 3, were used to calculate α* from all experiments. Figure 28 demonstrates that, in all cases, cakes compacted in a power-law fashion (i.e., straight-line increase in α* with ΔP when plotted on a log-log scale [52, 54, 56, 58, 64]). The resulting compressibility indices varied in the order: raw water < alum coagulation < electrocoagulation. Close inspection of the y-axes in Figure 28 reveals that α* and α_0* were significantly higher for the raw water than for the pretreated suspensions.

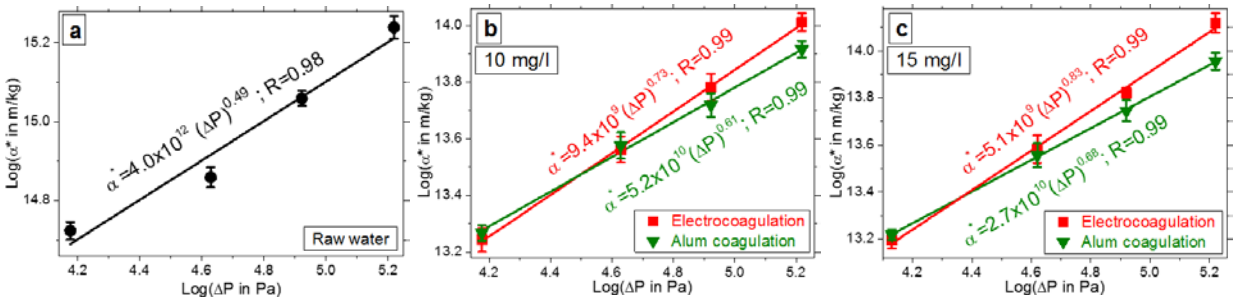

Figure 28. Power-law compressibility of colloidal deposits formed on the membrane surface for (a) untreated Lake Houston water and for (electro)coagulated suspensions at (b) 10 mg/L and (c) 15 mg/L aluminum dosage.

Raw-water cakes can be classified as moderately compactible (n=0.49), whereas highly compressible cakes were formed after coagulation with indices ($0.61 \leq n \leq 0.83$) in a similar range reported for other sweep flocculated colloids [54, 64]. Physicochemical characteristics of untreated, electrochemically coagulated, and alum-coagulated water were systematically and rigorously investigated in detail to elucidate cake compression mechanisms.

Primarily Amorphous $Al(OH)_{3(s)}$ Precipitates Were Generated by Electrocoagulation and Alum Coagulation

XRD patterns of solids generated by alum addition (aqua) and electrochemical aluminum addition (orange) to Nanopure water at pH 6.4 are shown in Figure 29. Shallow and broad peaks (hkℓ: 020, 120, 140, 031, 051, 200) were observed for electrocoagulation, indicating precipitation of small amounts of boehmite nanocrystals [37]. Applying Scherrer's formula to the most intense peak (2θ=14.5°) yielded a crystal size of ~5 nm, which is in the reported size range of fresh aluminum precipitates [153]. However, actual sizes may be somewhat larger since microstrain (e.g. dislocations and stacking faults) and instrumental effects also contribute to peak broadening [162]. Alum coagulated solids did not exhibit any crystallinity indicating differences in the nature of precipitates formed by electrocoagulation and alum coagulation in Nanopure water.

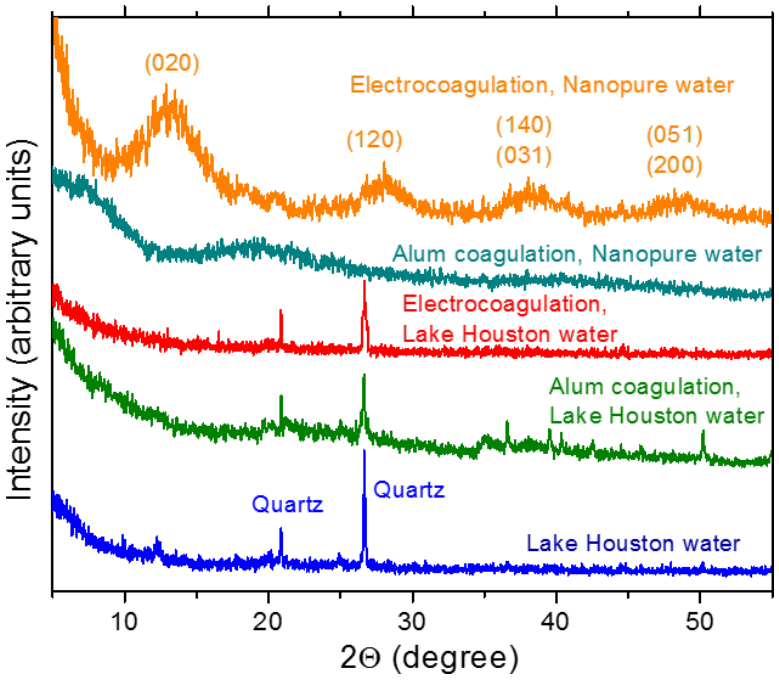

Figure 29. XRD patterns of electro-coagulated and alum-coagulated flocs.

Diffraction patterns of raw water colloids and the precipitates generated in Nanopure water are also shown.

Diffractograms corresponding to Lake Houston water (blue for raw water, red for electrocoagulation, and green for alum) are also shown in Figure 29. The only sharp peaks correspond to naturally occurring quartz probably from clays. Distinct boehmite peaks obtained when Al was electrochemically added to Nanopure water (orange line) were not visible in the corresponding diffraction

pattern for Lake Houston, which is attributed to disruption of crystalline Al precipitation by NOM [153, 163]. Hence, solids present in (electro)chemically treated MF feed waters were primarily amorphous, validated by the lack of any crystal habit in electron micrographs.

An XPS survey analysis was used to obtain the atomic concentrations (in percent) of cakes formed by untreated, electrocoagulated, and alum-coagulated Lake Houston water and also by "pure" (electro)coagulants generated in Nanopure water (Figure 30). Results corresponding to the "pure" precipitates will be discussed in this section. The O:Al atomic concentration ratio corresponding to "pure" electrochemically generated coagulant in Nanopure water was close to 3 (=3.14), indicating predominantly $Al(OH)_{3(s)}$ precipitates. Therefore, boehmite ($\gamma AlO(OH)$) did not contribute significantly to mass of Al solids even in Nanopure water. Note that boehmite has been described earlier in the text discussion of Figure 4. The O:Al ratio was significantly higher (=3.62) for "pure" alum-generated precipitates in Nanopure water. Sulfur (3.29%) was detected on alum-generated flocs arising from the concurrent addition of SO_4^{2-} anions during conventional alum coagulation [164]. Adjusting for the contribution of SO_4^{2-} ions reduced the O:Al ratio to near 3 (=2.96) demonstrating that the primary precipitate during alum coagulation was also $Al(OH)_{3(s)}$.

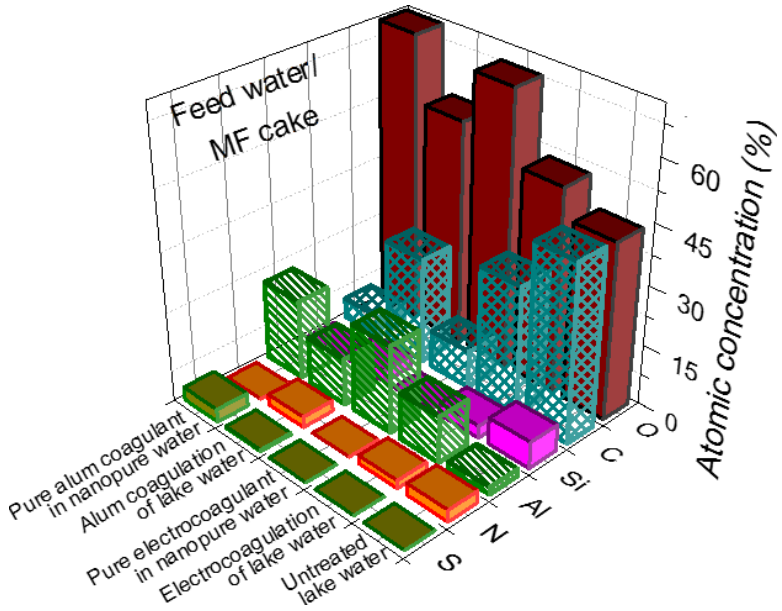

Figure 30. O, C, Si, N, Al, and S percentage atomic concentrations of MF cakes (untreated, electrofloated, and alum-coagulated Lake Houston water).

Atomic concentrations corresponding to "pure" coagulants generated during Nanopure water electro-flotation and alum coagulation are also shown.

Amorphous precipitates in pretreated MF feed waters appeared to be gelatinous and fluffy under the electron microscope, unlike natural colloids in Lake Houston. The gelatinous nature of amorphous $Al(OH)_3$ arises from kinetically favored high water uptake. The $Al(OH)_3$ eventually transforms to crystalline polymorphs with aging over longer timeframes [119, 165]. Hence, a portion of cake compressibility could be attributed to deformation of individual flocs that make up the foulant layer on the membrane surface. The deformation of individual flocs also could

partially explain the higher compressibility index reported after sweep flocculation compared with charge neutralization of surface water [64]. The inverse instantaneous flux followed the cumulative volume filtered in a straight-line manner [166], indicating low elastic contributions. Crystalline quartz and condensed siliceous shells (frustules) of diatoms [131] present in the raw water are rigid and not expected to deform at higher pressures, which partially explains the lower compression index of cakes formed by natural colloidal matter during MF of untreated water.

Physical Characteristics of Colloids in MF Feed Waters

Table 7 summarizes physicochemical properties of colloids and flocs in feed waters. As expected, pretreatment significantly increased the cake mass (high foulant loading) due to $Al(OH)_{3(s)}$ precipitates. Also, cake masses were similar following electrocoagulation and alum-coagulation pretreatment for a given aluminum dose. The greater productivity after pretreatment, despite the higher mass of cakes formed, demonstrates that (electro)coagulation formed more permeable deposits with lower specific resistance. This was confirmed by the aggregation of natural colloidal matter during pretreatment (Table 7), with alum and electrocoagulation increasing average particle sizes more than 12-fold. The slightly higher particle sizes measured for alum-coagulated flocs for a given aluminum dose was attributed to sulfate-mediated $Al(OH)_{3(s)}$ precipitation kinetics [153, 164]. Hence, lower cake specific resistance after pretreatment (Figure 28) was partially attributed to larger particles being filtered.

Table 7. Feed Water and Cake Characteristics for Untreated, Electrocoagulated, and Alum-Coagulated Lake Houston Water

Cake parameters	Raw water	Electrocoagulation		Alum coagulation	
		10 mg/L	15 mg/L	10 mg/L	15 mg/L
Cake mass (mg/mL)	0.008±0.002	0.035±0.002	0.049±0.003	0.036±0.001	0.050±0.002
Particle size (μm)	14±3	175±12	188±14	186±10	194±13
ζ potential (mV)	–16.51±0.13	–1.21±1.22	2.61±0.56	–3.07±1.70	–0.19±1.27
$d_{f,3D}$	2.75±0.10	1.67±0.02	1.74±0.11	2.17±0.06	2.07±0.13
α^*_0 (m/kg Pa^n)	4.00×10^{12}	9.40×10^{9}	4.39×10^{9}	7.62×10^{10}	4.23×10^{10}
n	0.49±0.04	0.74±0.05	0.85±0.07	0.58±0.04	0.63±0.03
Floc strength*	Strongest	Weakest		Medium	
Comments on chemical composition*	↑↑hydrophobic ↑↑amides ↑↑acidic organics ↑↑silica	↑hydrophobic ↓amides ↓acidic organics = silica		↓hydrophobic ↑amides ↑acidic organics = silica	

Suspended solids in untreated Lake Houston water were very dense and compact ($d_{f,3D}$=2.75), symptomatic of low attachment efficiencies during reaction-limited aggregation of stable, negatively charged colloids and floc restructuring [59, 163]. Electrocoagulation and alum coagulation effectively destabilized natural colloids by a combination of sweep flocculation and charge neutralization [37, 167], thereby increasing attachment efficiencies and lowering fractal dimensions

($1.67 \leq d_{f,3D} \leq 2.17$). Electrocoagulated aggregates were looser ($d_{f,3D} \approx 1.7$) than alum coagulated ones ($d_{f,3D} \approx 2.1$). In addition to the larger particle sizes resulting from coagulation, the formation of branched and porous flocs would further decrease specific cake resistance at null pressure by facilitating intra- and inter-floc water permeation [58–60]. Alum-coagulated flocs were always slightly more negative than their electrocoagulated counterparts for a given aluminum dose (Table 7) due to sorbed SO_4^{2-} ions revealed by XPS (Figure 30) [164]. Incorporation of hydrogen bubbles during electrocoagulation increased floc porosity and reduced $d_{f,3D}$ (e.g., 1.67 for electrocoagulation compared with 2.17 for alum coagulation at 10 mg Al/L). The order of magnitude lower α_o^* for electrocoagulation pretreatment compared with alum coagulation (e.g., 4.4×10^9 and 4.2×10^{10} m/kg Pa^n, respectively, at 15 mg Al/L) is attributed to the higher porosity of electrocoagulated flocs. Since flocs may rearrange in a filter cake especially at higher pressures [55, 62, 168, 169], we have compared α_o^*, not α^* as reported by others [58, 59, 61, 63].

Increased branching and porosity can also be expected to make electrocoagulated flocs more fragile, suggesting that higher pressures would induce their cakes to experience a greater degree of breakage and collapse [61, 62, 64, 168, 169]. As expected, higher compressibility indices were measured for cakes formed in electrocoagulated waters (e.g., 0.85 compared with 0.63 for cakes from alum-coagulated waters at 15 mg Al/L dose). As seen in Figure 27, alum-coagulated cakes were marginally more resistant at low pressure but electrocoagulated suspensions formed more resistant cakes at higher pressures due to a greater extent of inelastic compression (i.e., cake collapse and reorganization).

Chemical factors leading to differences in cake compression are discussed next.

Acidic Organics, Amides, and Hydrophobic Compounds Were Present on Natural Colloids (Untreated Water)

XPS survey spectra of cakes generated by filtering 150 mL of untreated Lake Houston water showed that the major elemental constituents were carbon (C 1s at 285 eV), oxygen (O 1s at 532 eV), silicon (Si 2s at 160 eV, Si 2p at 103 eV), and nitrogen (N 1s at 484 eV). Lower amounts of aluminum (Al 2s at 119 eV, Al 2p at 75 eV) and calcium (Ca 2p at 348 eV) were also detected and validated by atomic absorption spectroscopy (0.2 mg Al/L and 0.4 mg Ca/L respectively). The high-resolution Si 2p peak was centered near 103 eV, showing predominantly oxygenated siliceous compounds (e.g. silica and silicates) in lake water, which is consistent with quartz detected in XRD (Figure 29) and diatoms seen in scanning electron micrographs. As discussed, these forms of silica are rigid and not expected to contribute by themselves to compressibility. Detailed analysis of the C 1s, O 1s, and N 1s peaks (Figure 31) revealed that NOM in Lake Houston contained protein-like, carbohydrate-like, hydrophobic, and acidic organic compounds.

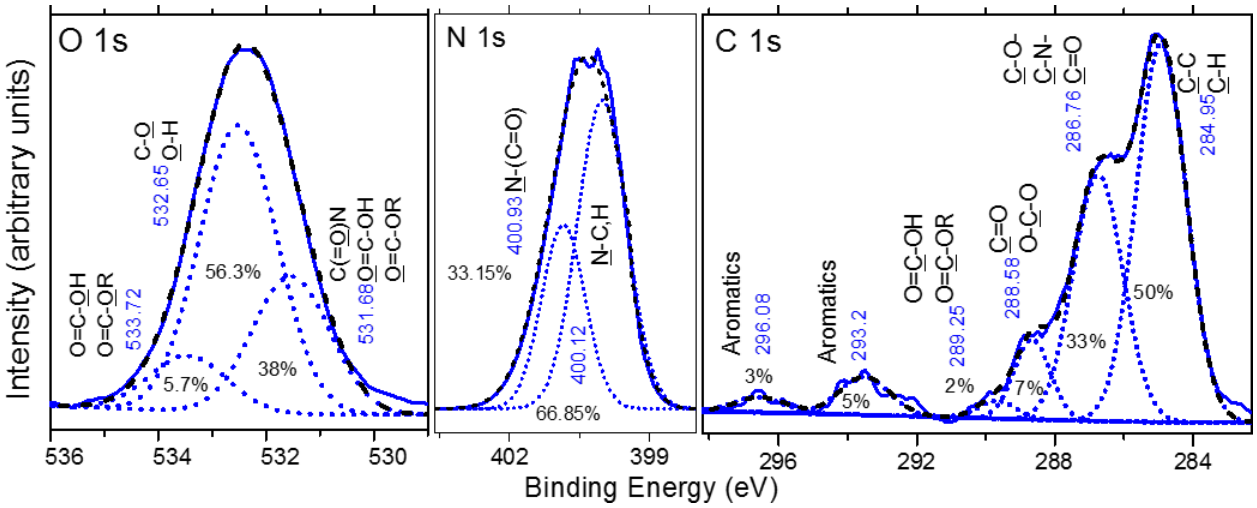

Figure 31. Curve fitted high resolution XPS spectra corresponding to C 1s, O 1s, and N 1s core level analysis of raw water colloids in the cake.

The C 1s core-level spectrum was resolved into four component peaks with full width at half-maximum (FWHM)=1.3–1.7 eV and binding energies at:

(i) 284.95 eV, attributed to –C–C–/–C–H in aromatic and aliphatic hydrocarbon backbones,
(ii) 286.76 eV, attributed to –C–O–/–C–N– in alcohols, phenols, and proteins,
(iii) 288.58 eV, attributed to –C=O/–O–C–O– in aldehydes, ketones, amides, and (hemi)acetals, and
(iv) 289.25 eV, attributed to C(=O)OH/C(=O)OR in humic and fulvic acids and esters [133, 167, 170, 171].

The shake-up satellite peaks at 293.2 eV and 296.08 eV probably resulted from π–π* transitions of aromatic rings [170] indicating NOM aromaticity (SUVA=2.94±0.30 L/mg-m). Note that the atom of interest, whose binding information is obtained, is underlined in the text and the figures.

The O 1s core level peak was decomposed into three peaks, each with FWHM=1.7 eV and binding energies at:

(i) 531.68 eV, attributed to carbonyl groups present in carboxyl/carboxylates (C(=O)OH/C(=O)O^-), esters (C(=O)OR), and amides (C(=O)N),
(ii) 532.65 eV, attributed to O–(C, H) from hydroxides and (hemi)acetals, and
(iii) 533.72 eV, attributed to singly bonded oxygen present in carboxyls (C(=O)OH) and esters (C(=O)OR) [133, 172, 173].

Hydroxides and (hemi)acetals indicate the presence of carbohydrates and sugars, whereas carboxyl/carboxylate moieties suggest organic acids. The concentration of carbohydrate-like substances measured by colorimetry was 0.81 mg/L.

The N 1s peak was centered around 400.2 eV, demonstrating predominantly organic nitrogen [174], verified by low concentrations of nitrite (<0.01 mg/L) and nitrate (0.11 mg/L) measured via ion chromatography. Raw water N 1s core level spectrum was resolved into two component peaks with 1.0–1.2 eV FWHM (Figure 31) and binding energies at:

(i) 400.12 eV, attributed to –N–C–/–N–H in amines and amino acids, and
(ii) 400.93 eV, attributed to –N(C=O)– in amides.

The concentration of protein-like substances measured by the modified Lowry assay was 0.32 mg/L.

The significant presence of polar compounds (e.g., amide, amines, and acidic organics) and hydrophobic moieties in natural colloids suggests an increased propensity toward hydrogen bonding and complexation, in addition to hydrophobic interactions. Hence, the low compressibility index of colloidal matter in Lake Houston can also be attributed to the relatively high strength of interparticle interactions that reduced inelastic cake behavior, in addition to physical factors discussed earlier. Variations in the atomic composition of precipitates formed by electrocoagulation and alum coagulation are discussed next to mechanistically understand differences in their compressibility.

Coagulation of Natural Colloidal and Organic Matter in Lake Houston Water and Uptake onto Flocs

Figure 30 also provides evidence for the transfer of carbonaceous, siliceous, and nitrogenous compounds from the raw water to (electro)chemically precipitated coagulants. For example, Si and N were not detected in “pure” coagulants generated in Nanopure water, but increased to 3.1 and 2.1 percent, respectively, in electrochemically precipitated $Al(OH)_3$ and to 3.0 and 2.7 percent, respectively, in alum coagulants from Lake Houston water. Similarly, only 9.3 and 5.1 percent of adventitious carbon was detected in coagulants formed by electrolyzing or adding alum to Nanopure water, respectively. However, C in coagulants from pretreated Lake Houston water increased to 32.3 percent after electrocoagulation and to 26.6 percent after alum coagulation. Survey spectra showed that alum coagulation was more effective than electrocoagulation in removing nitrogenous compounds, as evidenced by their relative N percentages (2.7% for alum and 2.1% for electro-coagulation). In contrast, both the uptake and speciation of sorbed siliceous compounds were similar in the two types of flocs (2.9% for alum and 3.1% for electrocoagulation), as shown by survey scans and high-resolution Si 2p peak deconvolution. Therefore, Si probably did not contribute significantly to measured differences in cake characteristics with pretreatment type.

The aluminum composition of alum-coagulated and electrocoagulated Lake Houston flocs was similar (11.6%). However, O was slightly higher in alum-coagulated Lake Houston flocs (56%) than in those generated electrochemically (51%). As was the case for the “pure” coagulants discussed earlier, this result is

attributed to oxygenated groups (e.g., SO_4^{2-}) that formed following alum addition. The presence of such groups is confirmed by (i) the slightly higher sulfur concentrations in the alum-coagulated flocs than in untreated lake water (0.4% in Figure 30) and (ii) marginally more negative ζ potential (Table 7). Changes in the component peak locations and areas in XPS spectra of electrocoagulated and alum-coagulated suspensions, compared to untreated Lake Houston water, were used to identify NOM sorption onto flocs, as discussed next.

Uptake of Carbonaceous Compounds by Flocs

Figure 32 depicts curve-fitted high-resolution C 1s XPS spectra corresponding to untreated Lake Houston water (left), electrocoagulation (middle), and alum coagulation (right).

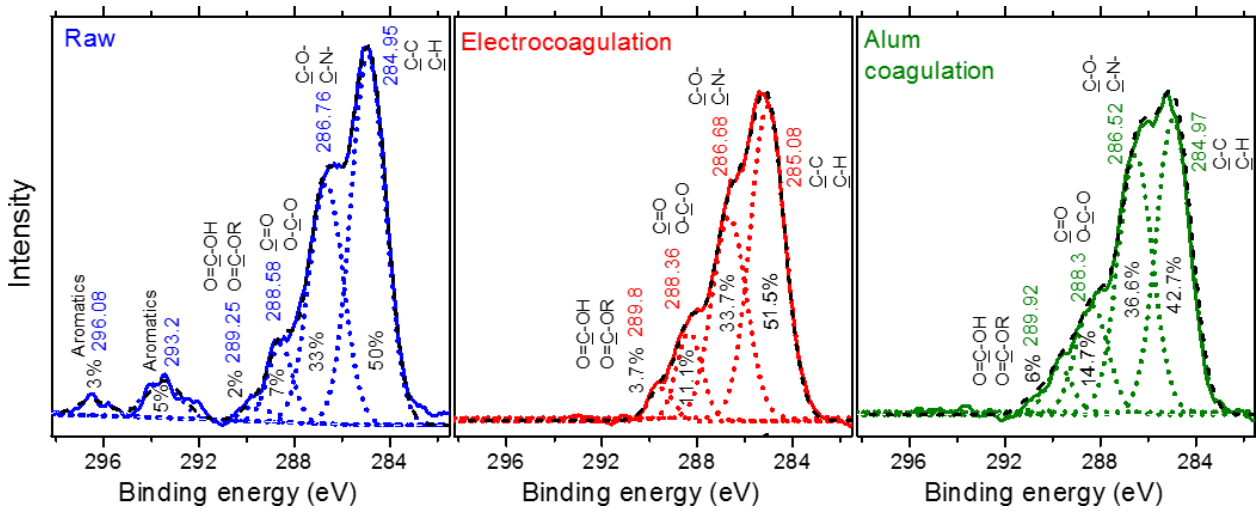

Figure 32. Deconvoluted XPS C 1s spectra corresponding to MF feed water flocs after no pretreatment, electrochemical pretreatment (includes both floated and suspended flocs/electro-coagulation), and alum coagulation.

Magnitude of y axis (intensity) is same in all three graphs. Coagulant dose = 10 mg Al/L. Note that the leftmost panel corresponding to untreated raw water is from Figure 31.

The alum coagulation C 1s peak was similar in intensity to the electrochemical pretreatment C 1s peak, showing similar removals of organic carbon by both methods. Correspondingly similar DOC concentrations were measured in MF permeates following alum coagulation (2.5 mg DOC/L at 10 mg Al/L and 2.3 mg DOC/L at 15 mg Al/L) and electrochemical pretreatment (2.6 mg DOC/L at 10 mg Al/L and 2.4 mg DOC/L at 15 mg Al/L). Although total NOM uptake was similar for both types of pretreatment, areas of component peaks for C–C/C–H, C–N/C–O, C=O/O–C–O, and C(=O)OH/C(=O)OR were different, indicating variations in the accumulation of these various moieties based on coagulation type. The C–C/C–H peak area was higher in electrocoagulated flocs (51.5%) than in alum flocs (42.7%), indicating greater sorption of hydrophobic organics [175]. This is presumably mediated by the electrolytically released hydrogen bubbles, which show a greater affinity towards hydrophobic surfaces [176, 177]. UV_{254}

absorbance values were slightly lower in MF permeates after electrocoagulation (0.054 cm^{-1} at 10 mg Al/L and 0.049 cm^{-1} at 15 mg Al/L) than after alum coagulation (0.059 cm^{-1} at 10 mg Al/L and 0.054 cm^{-1} at 15 mg Al/L), confirming greater uptake of hydrophobic compounds by electrocoagulated flocs.

In contrast, the C(=O)OH/C(=O)OR peak area was higher in alum coagulated flocs (5%) than in electrocoagulated ones (3.7%), indicating that the alum pretreatment is better at taking up acidic organic matter. Additionally, compared with raw water, the C(=O)OH/C(=O)OR peak was shifted by +0.67 eV in electrochemically generated flocs and by +0.55 eV in alum-coagulated flocs, indicating potential inner-sphere complexation of carboxylated NOM moieties with coagulant ≡Al-OH groups [133, 135, 156]. FTIR also showed complexation of acidic organic matter onto electrocoagulated flocs, indicated by the appearance of symmetric and asymmetric $C(=O)O^-$ stretching bands in the 1650–1400 cm^{-1} range [177]. Other C 1s component peaks of flocs did not exhibit significant binding energy shifts compared with raw water, demonstrating largely physisorption of NOM. Further, C–N and C=O/C(=O)N component peak areas were higher in alum-coagulated flocs (36.6% and 14.2%, respectively) than in electrocoagulated flocs (33.8% and 11.1%, respectively) showing the greater affinity of alum coagulation towards nitrogenous compounds such as amides.

Uptake of Nitrogenous Compounds by Flocs

Deconvolution of N 1s core level spectra showed peaks corresponding to N–(C=O) and N–C/H moieties, indicating sorption of proteinaceous compounds (Figure 33). The N–C/H component peaks in flocs showed negligible shifts in binding energy compared with raw water (<0.25 eV), indicating physisorption of amines onto electrocoagulated and alum-coagulated flocs. In contrast, the N–(C=O) peak showed significant shifts (+0.59 eV for electrocoagulation and +0.41 eV alum coagulation), signifying stronger sorption of amides than amines. Moreover, stronger and greater binding of proteinaceous compounds to alum flocs was inferred because their N–(C=O) peak (area=21.1%) was more intense than that of electrocoagulated flocs (area=17.9%).

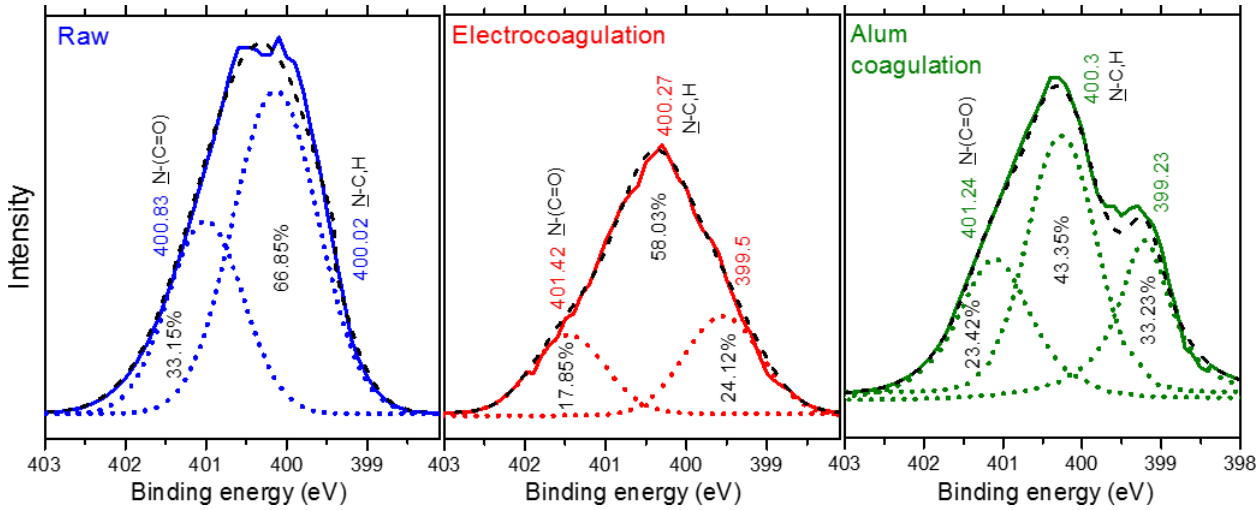

Figure 33. Curve fitted XPS N 1s spectra corresponding to MF feed water flocs after no pretreatment, electrochemical pretreatment (includes both floated and suspended flocs/ electrocoagulation), and alum coagulation.

Magnitude of y axis (intensity) is same in all three graphs. Coagulant dose = 10 mg Al/L.

Also in Figure 33, an additional peak at low binding energies emerged after both alum coagulation and electrocoagulation (399.2 and 399.5 eV, respectively). This probably originates from coagulation of dissolved nitrogenous substances that passed through the microfilter without pretreatment but were captured by it after (electro)coagulation. The new peak's area was greater for alum-coagulated flocs (31.2%) than for the electrocoagulated ones (24.1%), suggesting that conventional coagulation was more effective in taking up dissolved nitrogen. The overall N 1s peak in Figure 33, as well as C–N and N(C=O) component peaks in Figure 32, were also more intense for alum coagulation, further corroborating its greater removal of nitrogenous compounds than electrocoagulation. This was confirmed by colorimetric protein measurements performed after dissolving the flocs at high pH. This test showed 14 ng proteins/mg Al for the alum-coagulated flocs compared with only 10 ng proteins/mg Al for electrocoagulation.

Improvements in Nanofilter Flux with Advanced Pretreatment

Effect of Pretreatment Type on Nanofilter Fouling

DOC concentrations in the NF feed and permeate waters, along with steady-state specific flux values, are summarized in Table 8. Instantaneous NF fouling profiles with varying pretreatment types are compared in Figure 34.

Table 8. Comparison of DOC Concentrations and Steady-State NF Fluxes for Various Pretreatments

Pretreatment	Feed water (mg/L)	Permeate water (mg/L)	Steady state normalized specific flux (%)
MF only	5.99 ± 0.60	0.66 ± 0.04	51
Electrocoagulation–MF	3.58 ± 0.36	0.77 ± 0.09	72
Chemical coagulation–MF	3.82 ± 0.53	0.54 ± 0.07	77
Electroflotation–MF	3.55 ± 0.46	0.67 ± 0.07	88

As expected, the highest feed-water DOC concentration (6 mg/L) and lowest steady-state NF flux (49% decline) was measured following pretreatment with MF only. As noted in earlier reports [e.g., 75], the flux rapidly declined initially before reaching a steady state. As seen in Figure 34, any type of coagulation–MF pretreatment improved steady-state NF fluxes compared with pretreatment with MF alone, which is attributed to correspondingly lower DOC concentrations in the NF feed water (Table 8). Importantly, even though NF feed water DOC concentrations following any coagulation–MF pretreatment were similar (average 3.65 mg/L), a consistent trend was observed over all time intervals: fouling was best controlled by electroflotation–MF, followed by alum coagulation–MF, and then by electrocoagulation–MF (and MF only gave lowest fluxes). This pattern demonstrates the inadequacy of DOC concentration alone as a measure of fouling potential, as reported by others [e.g., 178, 179]. Hence, the surfaces of fouled membranes and deposited foulants were characterized extensively to obtain insights into foulants that caused different-flux decline profiles based on pretreatment.

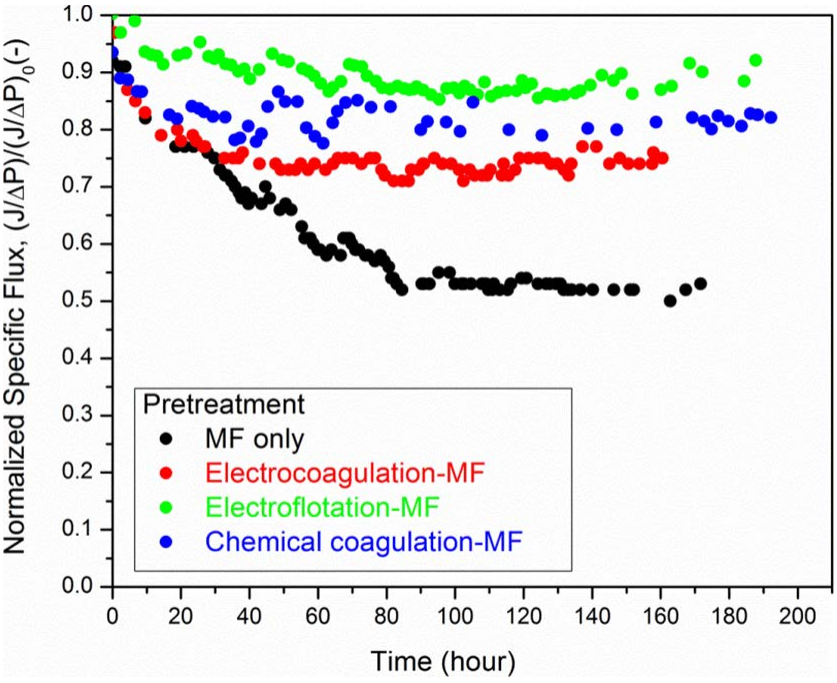

Figure 34. Comparison of NF flux decline profiles following various pretreatments.

Characterization by ATR-FTIR

ATR-FTIR spectra of the virgin and fouled NF membranes are compared in Figure 35, and peak assignments are summarized in Table 9. The virgin GE Osmonics DL membrane produced bands typical of modified semi-aromatic polyamide nanofilters [180, 181]. Only the amide I band (1640 cm^{-1}) was observed for the virgin DL membrane, and the amide II (1541 cm^{-1}) and aromatic amide bands (1609 cm^{-1}) were absent [181]. Aryl-O-aryl stretching (1243 cm^{-1}), symmetric SO_2 stretching (1151 cm^{-1}), and asymmetric SO_2 stretching (1323 cm^{-1}) peaks are attributed to the polysulfone support layer arising from penetration of the incident beam below the active layers of the DL membrane. Attenuation of these peak intensities in fouled membranes provides additional evidence that they are associated with the support layer.

For fouled nanofilters, bands in the region 950–1110 cm^{-1} were assigned to C–O–C and C–O–P vibrations, demonstrating that polysaccharides were important foulants. The peak at 1040 cm^{-1} signifies proteins or *N*-acetyl amino sugars from bacterial cell walls, suggesting that these polysaccharides potentially originated from bacterial extracellular polymeric substances [179]. Weak peaks in the bacterial fingerprint region (650–900 cm^{-1}) for all the fouled membranes (possibly arising from aromatic ring vibrations of various nucleotides) also suggest the biological origin of NF foulants in our study [182]. As has been found in other surface waters and wastewaters, protein foulants were also identified by the presence of the bands for amide I (1700–1600 cm^{-1}), II (1543–1548 cm^{-1}), and III (1240–1310 cm^{-1}) in fouled membranes [e.g., 73, 74, 183, 184]. The amide I band is mainly associated with C=O stretching of peptide linkages, with contributions from C–N stretching and CCN deformation. Amide II is largely the result of in-plane N–H bending and C–N stretching with small contributions from C=O stretching. Amide III is due to a complex mixture of coordinate displacements [185] and ν*C*–N stretching [186]. Fouled membranes had amide I peak intensities higher than those seen in the virgin membrane, and they also featured amide II peaks, which were completely absent in the virgin membrane. Also, the amide II band was absent in ATR-FTIR spectra of potential NF foulants removed by MF-alone pretreatment (data not shown). Therefore, its appearance on fouled surfaces suggests that peptides with predominantly C–N and N–H stretching either were not significantly removed during pretreatment or were generated by biological activity over the duration of nanofilter operation.

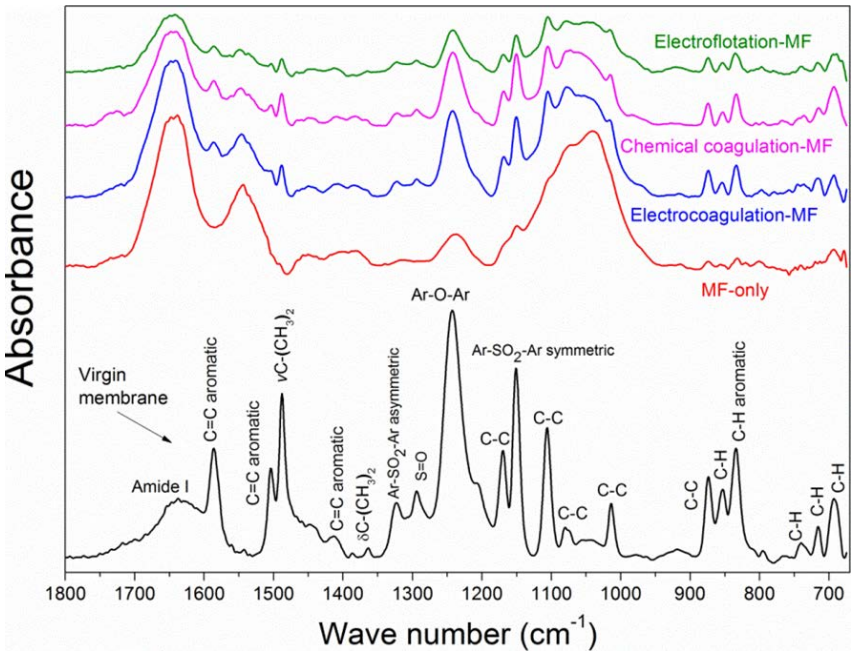

Figure 35. ATR-FTIR spectra of virgin and fouled NF membranes.

In all cases, the highest peak intensities were measured following MF-only pretreatment, indicating increased removal of NF-fouling polysaccharides and proteins during pretreatment by electrocoagulation and chemical coagulation. For example, the broad polysaccharide peak (950–1200 cm^{-1}) attenuated individual C–C and Ar–SO_2–Ar stretches in the virgin membrane. However, these peaks were recovered (but with lower intensities) following (electro)coagulation–MF, signifying partial polysaccharide removal during pretreatment. Analogously, NF foulant peaks were weakest following electroflotation–MF pretreatment, suggesting that this process was most efficient in foulant removal.

Table 9. Peak Assignments for FTIR Spectral Features of Virgin and Fouled Membranes [179, 181, 182, 187]

	Peak (cm^{-1})	Possible Peak Assignments
Polysulfone support	834	In-phase out-of-plane hydrogen deformation of para-substituted phenyl groups
	875–1110	*ν*C–C (C–C stretching vibrations)
	1151	Ar–SO_2–Ar stretching vibrations from polysulfone support
	1243	Ar–O–Ar stretching vibrations
	1323	Asymmetric SO_2 stretching vibration
	1365–1385	C–H symmetric deformation vibration of >C(CH_3)$_2$
	1586, 1504, 1488	Aromatic in-plane ring bend stretching vibration
Active/skin layer	1640	Amide I for virgin DL membrane

	Peak (cm^{-1})	Possible Peak Assignments
Foulant layer	650–900	*v*C–H (C–H rocking), bacterial fingerprint region, ring "breathing"
	1040	Proteins or *N*-acetyl amino sugar present in bacterial wall
	900–1200	*v*C–O–C, C–O dominated by the ring vibrations of polysaccharides C–O–P, P–O–P
	1240–1310	Amide III band from protein
	1543–1548	δNH bending and vC–N stretching associated with polypeptide chains in protein (Amide II bend)
	~1640	*v*C=O stretching associated with protein (Amide I band)

Protein Secondary Structures

Detailed information on the secondary structures of protein foulants was obtained by analyzing the amide I band (1700–1600 cm^{-1}) to compare pretreatment effects on foulant conformation (Figure 36). Table 10 summarizes the secondary structures detected on the surfaces of fouled nanofilters, which were identified based on spectral analyses of model peptides and proteins of known structures [182, 186, 188]. All fouled NF membranes contained predominantly α helices and β structures in nearly equal parts, suggesting similar contributions from animal or plant tissues and bacteria [182, 186]. The decrease in intramolecular β structures from MF only to electroflotation–MF pretreatment (left to right in Table 10), plus the decrease in turns and bends and the corresponding increase in random coils, indicates the loss of various proteins' three-dimensional structural stability and their adoption of unordered structures. The progressively increasing fraction of random coils from MF-only to electroflotation–MF pretreatment suggests coagulation-induced denaturation of protein foulants. Coagulation also decreased the α helices and increased the number of 3_{10}–helices, indicating a possible shift from carbonyl oxygen-to-amide hydrogen bonds between residues *i* and *i*+4 (α helices) to residues *i* and *i*+3 (3_{10}–helices) [189].

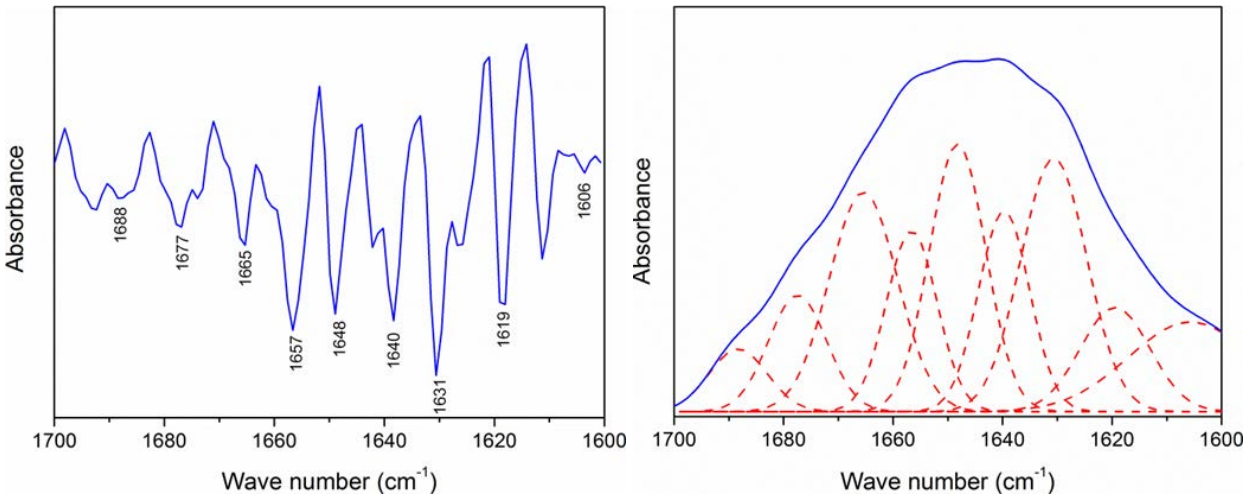

Figure 36. Representative second-derivative spectrum of the NF membrane surface following chemical coagulation pretreatment (left), compared with the curve-fitted amide I peak (right).

Table 10. Secondary Structure Peak Assignments for Amide I Band and the Percentage Area of Each Peak for NF Foulants with Different Pretreatments

Wave number (cm^{-1})	Secondary Structures	MF only (%)	EC–MF (%)	CC–MF (%)	EF–MF (%)
1600–1610	Amino acid side chain	4.9	6.8	8.5	10.1
1610–1625	Intermolecular β structure	7.9	7.7	7.9	13.4
1630–1640	Intramolecular β structure (β sheet)	22.3	17.8	11.2	5.8
1640–1650	Unordered structure/random coil	5.6	8.2	16.4	17.4
1650–1660	α helices	27.4	20.1	10.0	11.3
1659–1666	3_{10} – helix	0.0	18.5	16.4	11.8
1660–1680	Higher frequency of β structure	3.7	4.1	7.4	17.4
1663, 1680–1690	Turns and bends	28.2	16.9	22.2	12.9

EC, electrocoagulation; CC, chemical coagulation; EF, electroflotation.

Foulant Characterization by XPS

Survey and high-resolution scans of virgin and fouled membranes are summarized in Table 11. O/C and N/C ratios generally increased with any kind of coagulation pretreatment compared with MF alone, consistent with greater DOC removal (as shown earlier in Table 8). High-resolution scans were obtained to analyze amide functionalities and polysaccharides and for comparison with FTIR spectra. The C 1s peak was resolved into four components (Figure 37):

(1) A peak at 284.8 eV due to C–(C,H) from lipids or amino acid side chains;
(2) A peak at 286 eV attributed to C–(O,N, OH) associated with alcohol, ether, or amine;
(3) A peak at 287.8 eV from C=O, or N–C=O as in carboxylate, carbonyl, amide, acetal, or hemiacetal; and
(4) A weak peak at 288.9 eV arising from O=C–OH and O=C–OR, commonly found in carboxyl or ester groups.

Table 11. XPS Survey and High-Resolution Scans for Virgin and Fouled NF Membranes

NF Pretreatment	Survey Scans		High-Resolution Scans			
	O/C	N/C	284.8 eV C–(C,H) (%)	286 eV C–(O,N) (%)	287.8 eV (C=O, N–C=O) (%)	288.9 eV (O=C–OH, O=C–OR) (%)
Virgin (no pretreatment)	0.284	0.155	56.1	18.4	18.0	7.5
MF only	0.367	0.068	31.5	32.6	25.6	10.4
Electrocoagulation–MF	0.385	0.069	39.0	28.6	24.2	8.2
Chemical coagulation–MF	0.374	0.090	44.2	23.5	24.1	8.2
Electroflotation–MF	0.411	0.077	54.8	19.9	17.4	7.9

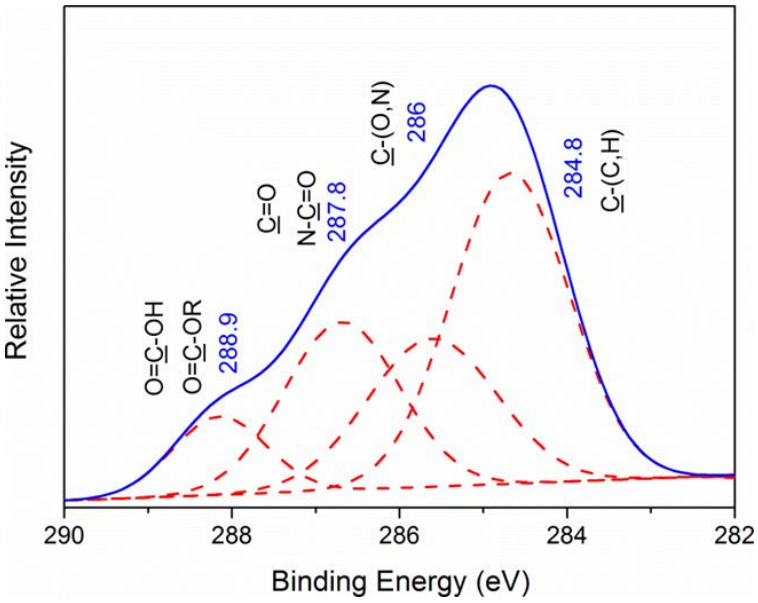

Figure 37. Representative high-resolution scan of C 1s region of a fouled NF membrane following pretreatment by chemical coagulation–MF.

In all cases, higher percentages of the 286-, 287.8-, and 288.9-eV C 1s peaks were measured on the fouled membranes than on the virgin membrane, consistent with the presence of protein and acidic polysaccharides in the foulant layer, as reported earlier via FTIR. The partial removal of protein and carbohydrates by any type of coagulation is manifested as lower percentages of the same peaks (and a correspondingly higher 284.8-eV peak) compared with MF-only pretreatment. Substantial contributions from C–(O,N), C=O, and HO–C=O in Table 11 are consistent with the FTIR finding that polysaccharides and amide I and amide II conformations of proteins contributed to NF fouling.

Alcian Blue Staining to Detect the Presence of Acidic Polysaccharides

Further evidence for polysaccharide fouling was obtained by colorimetry. Apparent bright blue to green spots or islands were observed in all fouled membranes following Alcian Blue staining, indicating that acidic polysaccharides contributed to fouling. It was observed that the polysaccharides generally accumulated near the vertices of the feed spacer (dead zone). One potential source of these foulants are transparent exopolymeric particles of biological origin, especially since MF alone is not effective in their removal [190, 191]. Positive stains in all pretreated nanofilters also indicate the ineffectiveness of coagulation to remove these foulants.

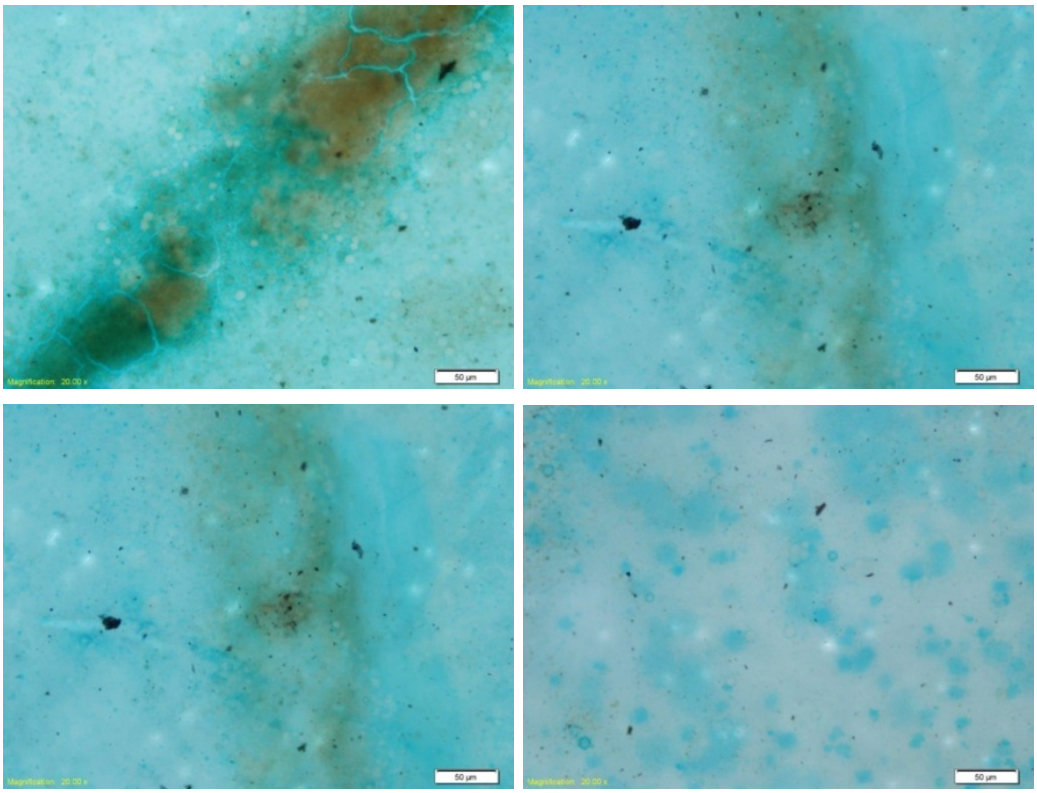

Figure 38. Images of NF membrane surfaces after Alcian Blue staining following various pretreatment processes, showing the presence of transparent exopolymeric particles.

Top left (MF-alone), top right (electrocoagulation–MF), bottom left (alum coagulation–MF), and bottom right (electroflotation–MF).

Hydrophobicity

Contact angles of fouled NF membranes (62±3.7°) were very similar to each other and to that of the virgin membrane (61±1.1°), as depicted in Figure 39. Hence, fouling and pretreatment type did not have significant effects on nanofilter wettability. Similar results have been reported for other nanofilters and ultrafilters with virgin membrane contact angles in the range 40–60 degrees fouled by hydrophilic components of NOM [179, 183]. Therefore, it appears that the predominant foulants in our experiments were also hydrophilic neutrals such as polysaccharides and amides identified earlier by spectroscopy. This is consistent with preferential removal of high-molecular-weight hydrophobic components by coagulation pretreatment. Additionally, the contact angle of the raw-water colloids removed by MF alone as a cake layer was measured to be significantly higher (73±0.9°), indicating preferential removal of hydrophobic NOM by MF alone. Hence, the pretreatment alternatives evaluated appear to have removed more of the hydrophobic components in the raw water, thereby relatively enhancing the hydrophilic fraction of NOM in the NF feed water.

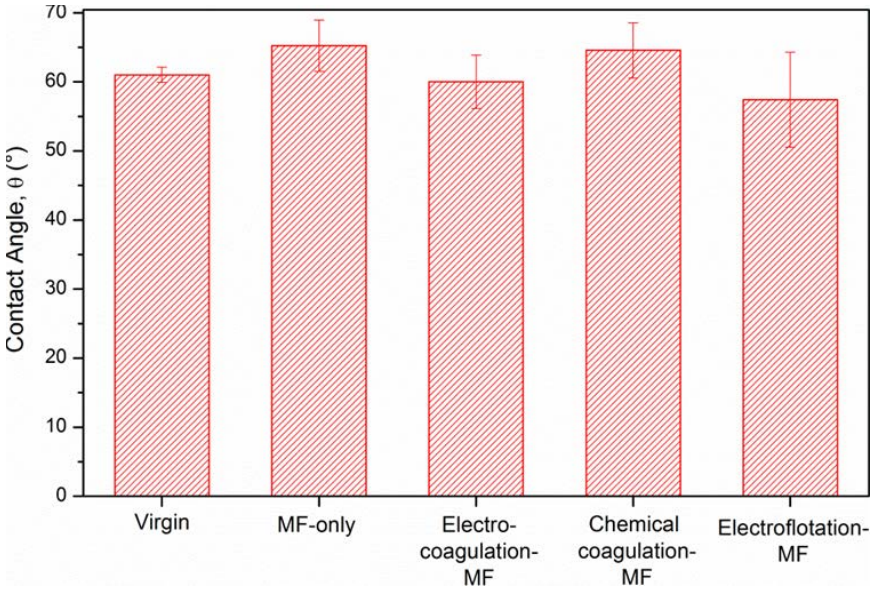

Figure 39. Contact angles for the virgin and fouled NF membranes.

Surface Topography by AFM

Three-dimensional AFM images of a virgin membrane and a representative fouled membrane (after chemical coagulation–MF pretreatment) and corresponding roughness values are given in Figure 40 and Table 12, respectively. The DL membrane exhibited the typical "peak and valley" network characteristic of all polyamide membranes, and its roughness was 49 nm, similar to previously reported values [192]. Foulant deposition changed the surface morphology (see Figure 40) and only slightly increased the root-mean-square roughness for all pretreatments. These changes are attributed to the relatively low divalent cation concentrations (total hardness of 67 mg/L as $CaCO_3$) in the feed water, which lowered NOM complexation, resulting in thinner and sparser foulant deposition [193, 194]. The efficient removal of larger molecular weight (more bulky) hydrophobic compounds by all pretreatments evaluated resulted in statistically similar surface roughness values (at 95% confidence) for all fouled nanofilters.

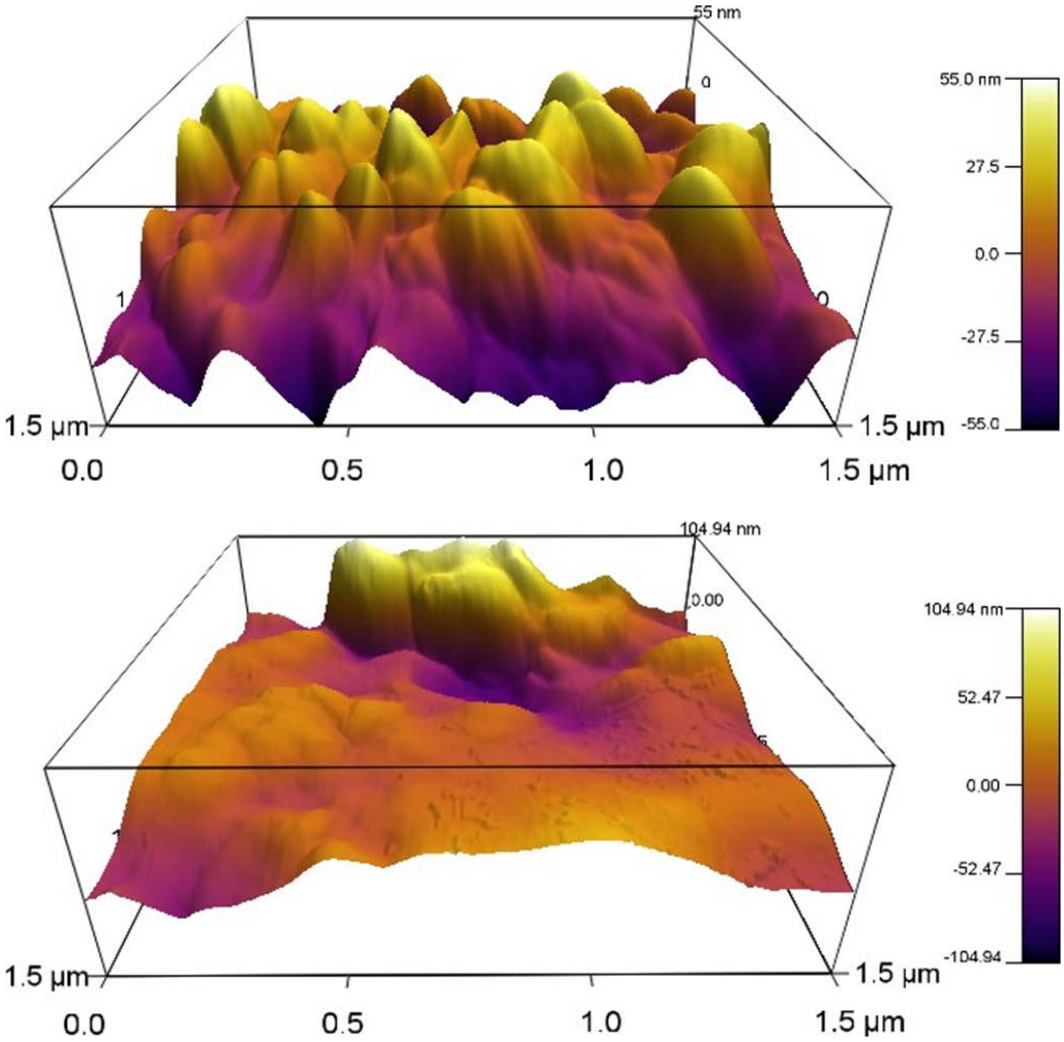

Figure 40. Surface topography of NF membranes.

The virgin membrane is shown in the top, and the fouled membrane, after chemical coagulation–MF pretreatment, is shown in the bottom.

Table 12. Root-Mean-Square Roughness Values for Virgin and Fouled NF Membranes

NF pretreatment	Roughness (nm)
Virgin (no filtration)	49 ± 1.11
MF only	77 ± 11.51
Electrocoagulation–MF	76 ± 8.30
Chemical coagulation–MF	61 ± 1.55
Electroflotation–MF	60 ± 7.99

Virus Control by Iron Electrocoagulation–Microfiltration

Electrocoagulation Generated Ferrous Iron at Nearly 100-Percent Efficiency

Iron dissolution was monitored over a range of current densities by varying the current and the electrocoagulant generation times. The results are summarized in Figure 41.

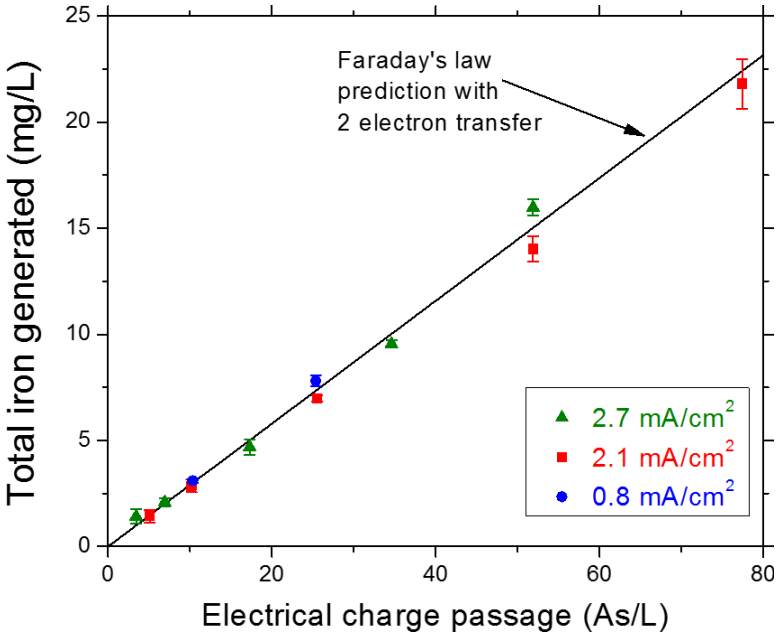

Figure 41. Experimental evidence for ferrous iron generation during electro-coagulation at different current densities.

Figure 41 demonstrates that iron concentrations in the electrochemical cell increased linearly with total charge passed and agreed quantitatively with Faraday's law predictions for two-electron transfer. Therefore, the only anodic process in our experiments was the oxidation of iron metal to soluble Fe^{2+} in accordance with other recent reports [195, 196]. In contrast, not cleaning the anode can result in passivation, chemical dissolution, or pitting, which can either increase or decrease iron concentrations in the cell relative to the Faraday's law predicted values, especially during longer term operation [8, 195, 196]. Substantial ferrous iron concentrations were directly measured in the cell after 2 minutes of rapid mixing at slightly basic and slightly acidic pH levels. The results, especially those at pH 6.4, provide additional evidence for Fe^{2+} dissolution. (See Figure 42.) The fraction of Fe^{2+} was significantly lower at the higher pH level. For example, after 6 s electrolysis, more than half the total iron was present as Fe^{2+} at pH 6.4, whereas only 6 percent Fe^{2+} was measured at pH 7.5. This result was caused by the strong (inverse second order) influence of pH on the Fe^{2+} oxidation rate, since electrocoagulation was initiated under open atmospheric conditions [195, 197, 198] in the absence of NOM.

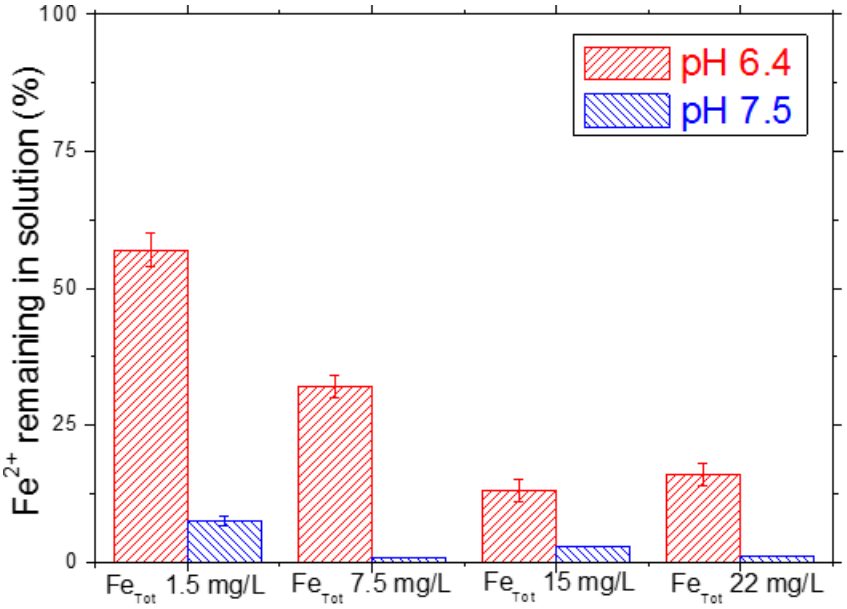

Figure 42. Ferrous iron concentrations as a percentage of total iron for different electrolysis durations at pH 6.4 and 7.5.

Based on the above evidence, $Fe(OH)_3$ precipitation in our experiments is expected to occur predominantly through dissolved-oxygen-mediated oxidation of electrochemically generated Fe^{2+}:

Anode:	$Fe^0_{(s)} = Fe^{2+} + 2e^-$
Oxidation:	$4Fe^{2+} + O_2 + 4H^+ = 4Fe^{3+} + 2H_2O$
Hydrolysis:	$Fe^{3+} + 3H_2O = Fe(OH)_3 + 3H^+$
Cathode:	$2H_2O + 2e^- = 2OH^- + H_{2(g)}$
Overall:	$4Fe^0_{(s)} + 10H_2O + O_2 = 4Fe(OH)_{3(s)} + 4H_{2(g)}$

The hydrolysis reaction shown is a simplified version of the multitude of reactions given by Stumm and Morgan [198]. Bubbles were formed in the electrochemical cell, as predicted by the above reactions. Also, the cathodic production of hydroxyl ions transiently increased the bulk pH of the Lake Houston water during electrolysis by approximately 0.5 units, which later decreased to approximately the original value. (The alkaline lake water has a low buffering capacity.) Since these pH changes are expected to depend on feed-water alkalinity, current density, and residence time (iron dosage), it is recommended that the pH be monitored closely during electrocoagulation.

Virus Reductions in Electrocoagulated and Chemically Coagulated and Microfiltered Waters

Figure 43 summarizes reductions in MS2 virus concentrations in microfiltered synthetic and natural waters after electrocoagulation and chemical coagulation pretreatment. In the absence of any pretreatment, microfiltration alone removed

only < 0.5-log of viruses, demonstrating negligible sieving. This result was expected, as the virus size, on average, is only 14 percent of membrane pore diameter. Pretreatment with chemical coagulation for Lake Houston water and electrocoagulation for synthetic water increased virus removals monotonically with coagulant dosage [16, 87, 88], attaining the 4-log removal/inactivation criterion under the Surface Water Treatment Rule at relatively low iron dosages (<4 mg/L).

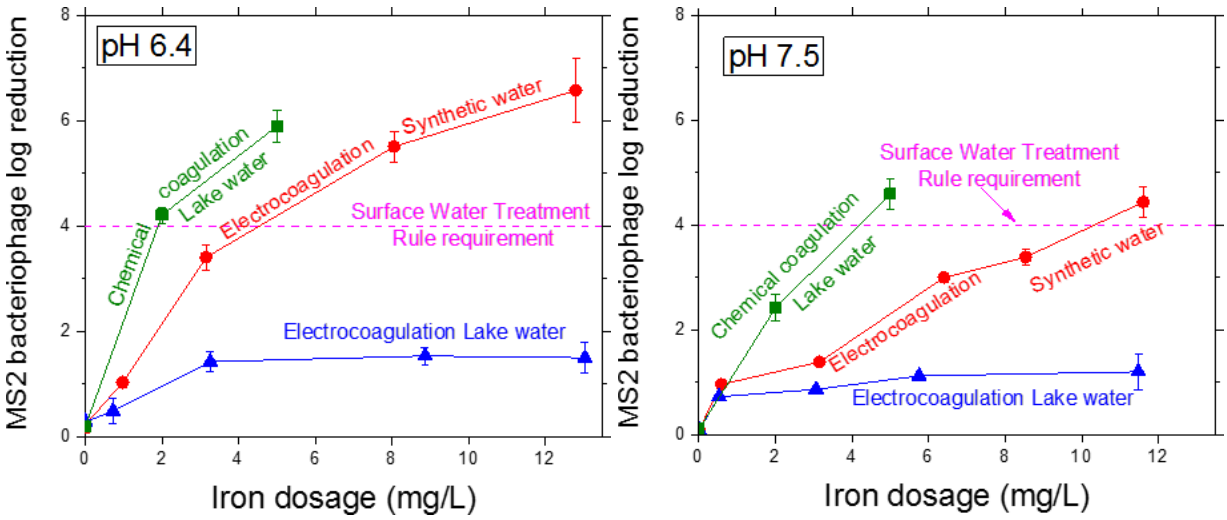

Figure 43. Comparison of virus removals by microfiltration with different pretreatment processes and feed waters at pH 6.4 and 7.5.

In contrast, electrocoagulation was ineffective for virus control in natural water, achieving a maximum of only 1.5-log (97%) reduction at pH 6.4, even at a relatively high iron dosage of 13 mg/L. However, electrocoagulation–MF achieved 6.5-log (99.99997%) virus reduction from synthetic water at pH 6.4 at a similar iron dosage. Similar trends were obtained at pH 7.5: electrocoagulation–MF was more effective in controlling viruses from synthetic water that was devoid of NOM compared with those from natural water that contained moderate DOC concentrations (4.5 mg/L). It is hypothesized that the poor performance of iron electrocoagulation pretreatment in removing viruses from Lake Houston water was caused by the presence of NOM (discussed below in the section "NOM Decreases Effectiveness of Virus Removals").

Also as seen in Figure 43, conventional chemical coagulation outperformed electrocoagulation pretreatment for virus control in Lake Houston water at both pH values investigated. Low virus reductions by electrocoagulation were due to electrochemical generation of highly soluble Fe(II) (which was oxidized to relatively insoluble $Fe(OH)_3$ in situ). However, insoluble $Fe(Cl)_3$ is directly added in chemical coagulation, which precipitated and encapsulated viruses, removing them over the course of the experiment. Viruses were controlled more effectively by adding more and more Fe(III) due to availability of a greater number of sites

for virus sorption and superior virus enmeshment by increasing mass of $Fe(OH)_3$ precipitates [16, 89].

Figure 43 further depicts better virus control at pH 6.4 than at pH 7.5 for chemical coagulation of natural water and for electrocoagulation of synthetic water. Hence, it appears that increased charge neutralization and a greater degree of electrochemical inactivation at pH 6.4 were more important than decreased $Fe(OH)_3$ precipitation in controlling viruses in these experiments. However, virus reductions were poor for electrocoagulation of natural water at both pH values investigated, which is attributed to Fe^{2+} complexation by NOM and resulting weak destabilization.

Direct Evidence for Virus Sorption onto Iron Flocs

Virus concentrations in seeded feed waters were measured after adding 1 mL of stock solution ($O(10^{10})$ PFU/mL) to the 450-mL test suspension to be electrocoagulated, resulting in feed concentrations of $O(10^8)$ PFU/mL. After selected electrocoagulation experiments (before microfiltration), iron flocs were separated by centrifugation (10,000 *g* for 20 minutes) and dissolved in 6 percent beef extract (after elevating the pH to 9.5) to quantify sorption of MS2 phages onto the precipitated coagulant [88, 199]. As seen in Figure 44, nearly all the seeded viruses ($O(10^8)$) were recovered from the synthetic water, demonstrating that the vast majority of the viruses were sorbed onto the iron hydroxide precipitates. In contrast, only a very small fraction of the seeded viruses (1.3%) were associated with the precipitates for natural water. These measurements confirm the negligible removals by sweep flocculation from NOM-containing surface water, whereas excellent removals were possible in the absence of NOM (from synthetic water), as shown in Figure 43.

Evidence for Virus Inactivation in the Electrochemical Cell

Figure 43 also depicts that a lower pH enhanced virus control during electrocoagulation–microfiltration of synthetic waters and chemical coagulation–microfiltration of Lake Houston water. For example, at an electrocoagulant dose of ~ 8 mg/L, MS2 concentrations in synthetic water were reduced by 5.5-log (99.9997%) at pH 6.4 but only by 3.4-log (99.96%) at pH 7.5. To better understand the differences in virus reductions during electrocoagulation between pH 6.4 and 7.5, more control experiments were performed. Viruses were added to natural and synthetic water after pH adjustment and electrocoagulated at a dose of 10 mg/L as Fe. After electrochemical iron dosing, the water was then slowly mixed for a period of 5 hours (duration of a typical experiment), and viruses in the supernatant and flocs were enumerated every hour. Viruses associated with the flocs were enumerated following dissolution in beef extract at pH 9.5, as explained in the previous section. Inactivation values reported in Figure 45 were calculated using virus concentrations in both the supernatant and the flocs [88, 199].

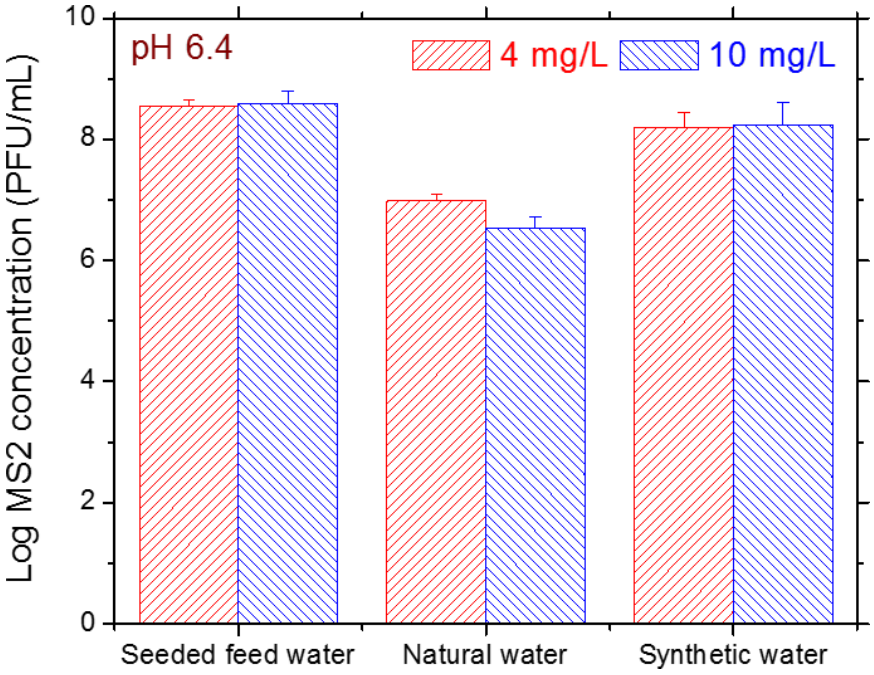

Figure 44. Virus recoveries by dissolving electrocoagulated flocs from natural and synthetic waters.

The bars labeled "seeded feed water" refer to measurements made immediately after adding virus stock to the test water. The bars labeled "natural water" and "synthetic water" refer to measurements made in the respective waters after dissolving flocs that formed after electro-coagulating for 25 s (4 mg/L Fe) and 62 s (10 mg/L Fe). As observed, almost all the viruses were present in the supernatant of the natural water compared with those adsorbed onto flocs. The reverse trend was obtained for synthetic water where almost all the originally seeded viruses were sorbed onto iron precipitates.

As seen in Figure 45 for synthetic waters, virus concentrations monotonically decreased over time, reaching 2.2-log at pH 6.4 and 1.2-log at pH 7.5 after 5 hours. Hence, MS2 viruses appear to be inactivated during electrocoagulation of synthetic waters in the absence of NOM, which can be partially attributed to electrochemically generated oxidants such as $^{\bullet}OH$, O_3, H_2O_2, free chlorine and ClO_2 simply due to current passage [200–202]. Additionally, similar to Fe^{2+} produced by dissolution of nanoparticulate zerovalent iron [111], the anodic dissolution of metallic iron can result in the formation of hydroxyl radicals and superoxide anions, which are capable of inactivating MS2 viruses. In any case, the measured reductions in MS2 concentrations in synthetic waters are attributed to oxidative modifications of the proteinaceous capsid by exogenous reactive oxygen species (ROS) or alterations to the capsid proteins' secondary structures following sorption onto the flocs [88, 111, 203]. In contrast, only 0.2-log reductions in MS2 concentrations were measured at 5 hours for natural waters. This suggests that NOM potentially acted as a sink for electrochemically produced ROS, reduced the ROS generation rate, and/or decreased direct Fe^{2+}-virus interactions via complexation [111, 204, 205].

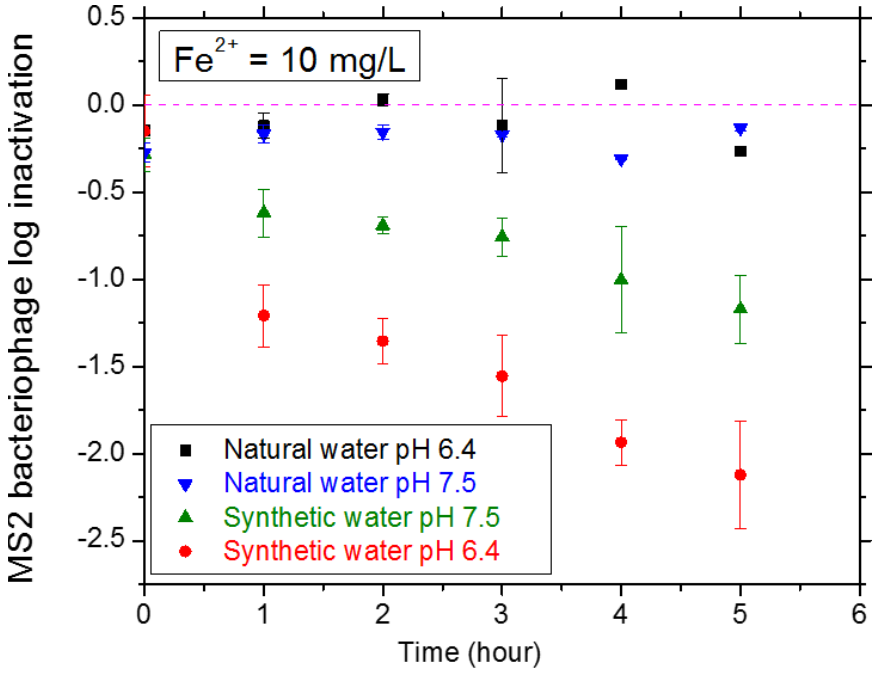

Figure 45. Ferrous iron inactivates MS2 coliphage in synthetic waters only when no NOM is present.

Virus Destabilization Mechanisms

As illustrated in Figure 46, the ζ potential of MS2 viruses in synthetic water, in the absence of any coagulant, was approximately –35 mV, which is consistent with literature reports e.g. [206, 207]. The magnitude of the ζ potential was lower in natural water (~ –17 mV) potentially due to adsorption of NOM and divalent cations. The less negative zeta potentials for colloids suspended in natural water at pH 6.4 were attributed to more protonation of adsorbed NOM (reduced degree of dissociation and lower negative charge) in acidic waters and to the higher concentrations of positively charged $Fe(OH)^{2+}$ and $Fe(OH)_2^{+}$. At pH 7.5, by contrast, the dominant species are $Fe(OH)_3^{0}$, $Fe(OH)^{2+}$ and $Fe(OH)_4^{-}$, which as a first approximation can be assumed to be adsorbing onto flocs [115]. Since the MS2 virus was negatively charged in all the experiments, the electrostatic barrier was decreased at lower pH, allowing greater removals by adsorption. Other research [e.g., 17, 208] has found that the ζ potential of electrocoagulated virus suspensions increases (→ 0) with iron dose for a given pH in both surface water and synthetic water. Sweep flocculation was the dominant virus destabilization mechanism, since significantly negative ζ potentials (approximately –15 mV) were measured even at the highest iron concentration employed in removal experiments. (See Figure 43.) This suggests the secondary role of adsorption of positively charged iron species onto viruses and the resulting charge neutralization.

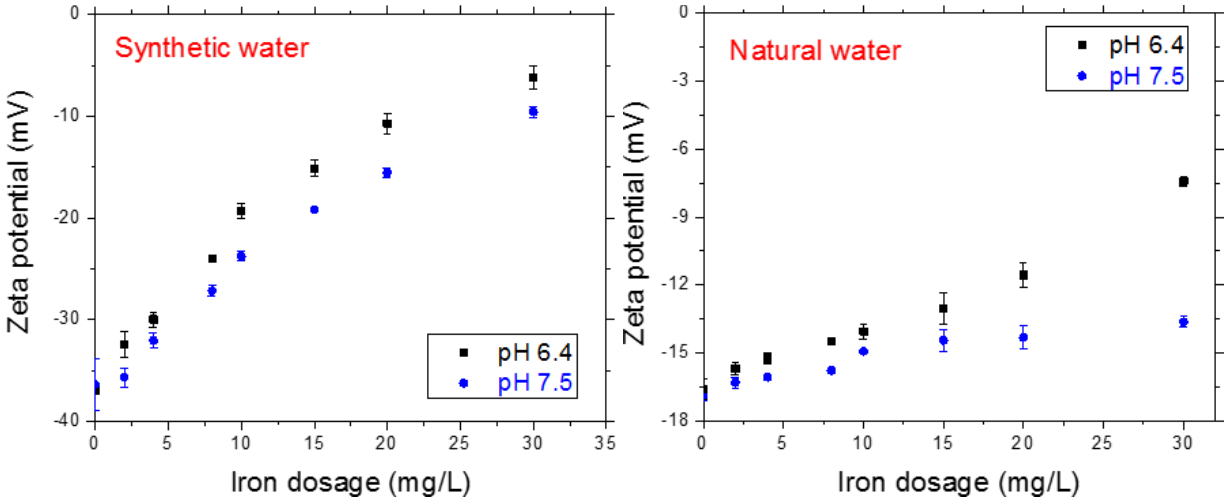

Figure 46. Effect of electrochemical iron addition on zeta potential in synthetic and natural waters at pH 6.4 and 7.5.

Virus Removals Increased as a Cake Layer Was Formed for Natural Water

A monotonic trend of increasing removals was observed for natural waters as filtration progressed (Figure 47). In other words, the cake layer appears to have reduced the effective membrane pore size and also served as a "dynamic membrane," contributing a secondary filtration effect for viruses in the presence of colloidal materials [81, 82]. Additionally, since the isoelectric point of $Fe(OH)_3$ is close to 8.0, it tends to be positively charged in the pH range of our experiments and can therefore adsorb negatively charged MS2 viruses, thus contributing to additional removal by the cake layer. These effects are similar to increases in dissolved solute rejection due to the presence of a foulant layer, which has been attributed to sieving or specific interactions [42, 209]. Since virus concentrations in the filtered water decreased over time, the average of three samples (taken near the beginning, middle, and end of filtration after 5, 24, and 37 cm^3 filtered/cm^2 membrane area, respectively) was used to calculate the log virus reductions reported in Figure 43.

After filtration, the membranes were dried overnight in an oven at 60 °C, sputter coated with a thin conductive (gold) layer and observed under a field emission scanning electron microscope (LEO 1525, Carl Zeiss). The left panel in Figure 48 depicts the heterogeneous nature of natural colloidal materials present in surface water. Morphology of the cake in the right panel of Figure 48 also suggests that amorphous iron oxyhydroxides were present [210]. Natural colloids are seen to be interspersed with flocs on membranes used to filter electrocoagulated samples, which is consistent with in situ oxidation of Fe(II) to form insoluble $Fe(OH)_3$ (and which also explains the poor electrocoagulation performance indicated in Figure 43).

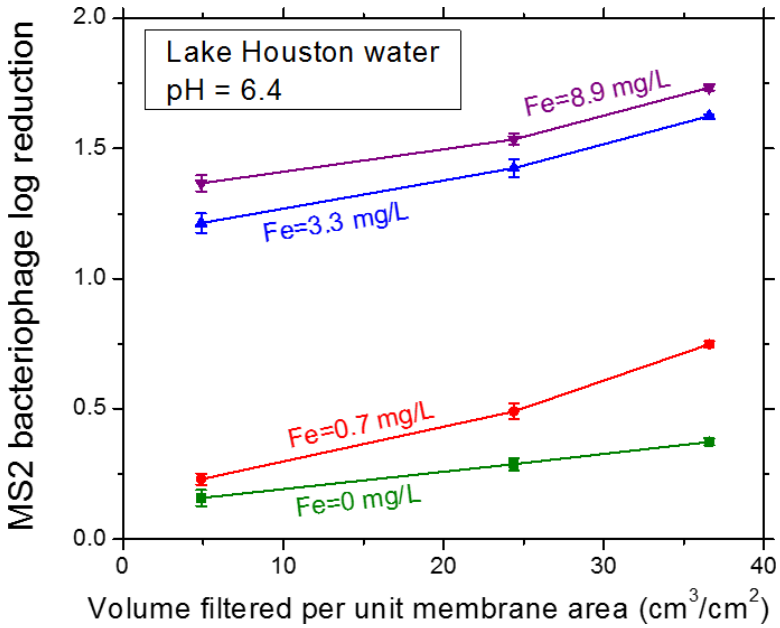

Figure 47. Effects of coagulant dose and cumulative volume filtered on virus control.

MS2 concentrations in the permeate decreased as a cake was formed during microfiltration of natural water.

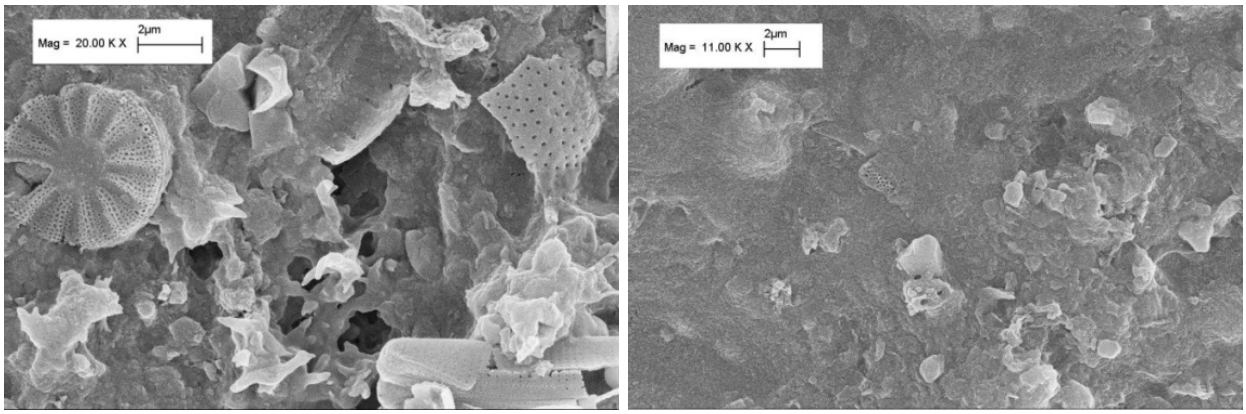

Figure 48. Scanning electron micrographs of natural colloidal materials visualized after filtering raw water (left) and of the cake formed after filtration of 150 mL of electrocoagulated water at pH 6.4 and 10 mg Fe/L (right).

NOM Decreases Effectiveness of Virus Removals

To empirically demonstrate the deleterious role of NOM on virus removals during iron electrocoagulation, 5 mg/L of Suwannee River Humic Acid was also added to synthetic waters. Virus removals from these feed waters were evaluated by electrocoagulation–microfiltration at an iron dosage of 10 mg/L at pH 6.4 and 7.5. Separate chemical coagulation experiments were also performed in which soluble $FeSO_4$ was added (10 mg/L as Fe^{2+}), rapid mixed for 1 minute at 495 s^{-1}, flocculated for 30 minutes at 32 s^{-1} and immediately filtered using a 0.22-µm

syringe filter (09-719A MCE sterile, Fisher Scientific). As shown in Figure 49, the presence of NOM worsened virus removals by ~4-log at pH 6.4 and ~2-log at pH 7.5 following electrocoagulation–microfiltration. Also, virus removals by $FeSO_4$ coagulation–microfiltration deteriorated by ~1.5-log at both pH values. These results indicate competition between NOM and viruses to interact with hydrolysis species such as Fe^{3+}, $FeOH^{2+}$, $Fe(OH)_2^{+}$, and $Fe(OH)_4^{-}$, which would decrease viruses sorption onto iron flocs instead resulting in Fe^{2+}-NOM complexes. Humic acids can also interfere with the kinetics of ROS production in the electrochemical cell by providing carboxyl groups to complex with Fe^{2+} or alternately by initiating, promoting, or inhibiting ROS transformations [211, 212]. Hence, NOM appears to inhibit virus control by (i) complexing with Fe^{2+} and slowing its rate of oxidation to insoluble Fe^{3+}, thereby interfering with sweep flocculation [205, 213], (ii) reducing direct interactions between Fe^{2+} and capsid amino acids due to complexation [214], (iii) scavenging ROS and decreasing their concentration, or (iv) decreasing the ROS generation rate [204]. Similar results have also been reported during filtration with carbon nanotubes, in the course of which virus removals decreased upon NOM addition [206].

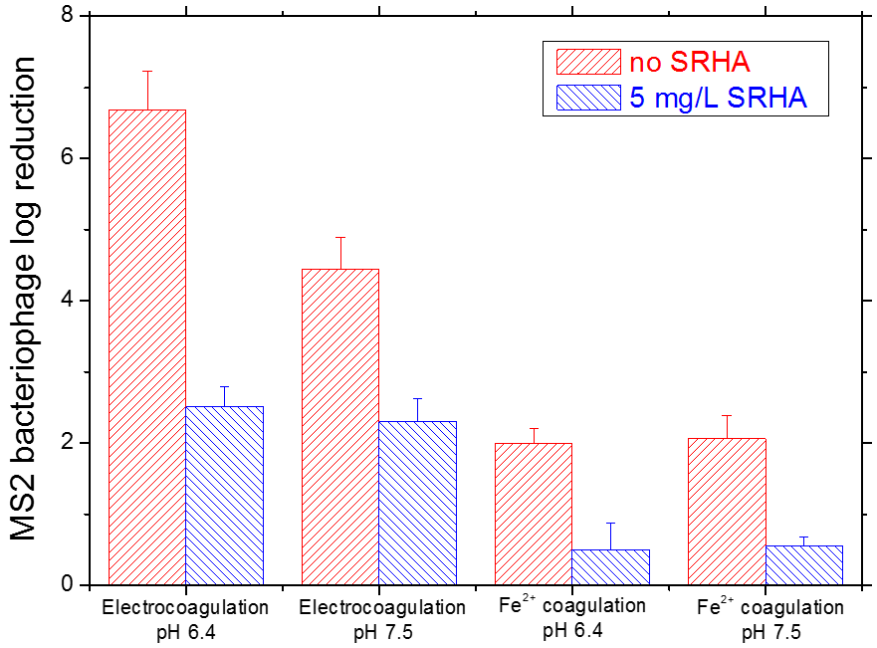

Figure 49. Lower virus removals from synthetic water to which 5 mg/L Suwannee River Humic Acid had been added.

Electrocoagulation at 10 mg/L iron was used as pretreatment for microfiltration. $FeSO_4$ was employed as the chemical coagulant (at a dosage of 10 mg/L as Fe), and the flocculated (30 minutes) suspension was immediately filtered through a 0.22-µm syringe filter.

Virus Control by Aluminum Electrochemical Pretreatment to Microfiltration

Virus Reductions in Treated Waters

As shown earlier [16, 82, 215], when no coagulant was added, virus reductions were only approximately 0.2-log, demonstrating negligible sieving of the 27-nm virus by the microfilter nominally rated at 220 nm, as seen in Figure 50. Coagulation pretreatment reduced virus passage, resulting in 2.5–3.0 log removal at an intermediate dosage of 5 mg/L. Separate controlled experiments demonstrated that viruses were not inactivated by aluminum electrolysis and aluminum sulfate addition, unlike the results obtained using prehydrolyzed aluminum salts [216, 217]. This finding demonstrates negligible net production of chemical oxidants during aluminum electrolysis, unlike the results for electrodes such as Pt/Cu or Ti/RuO_2 [202, 218]. Therefore, measured reductions in virus concentrations in all our experiments were solely attributed to their removal and not their inactivation.

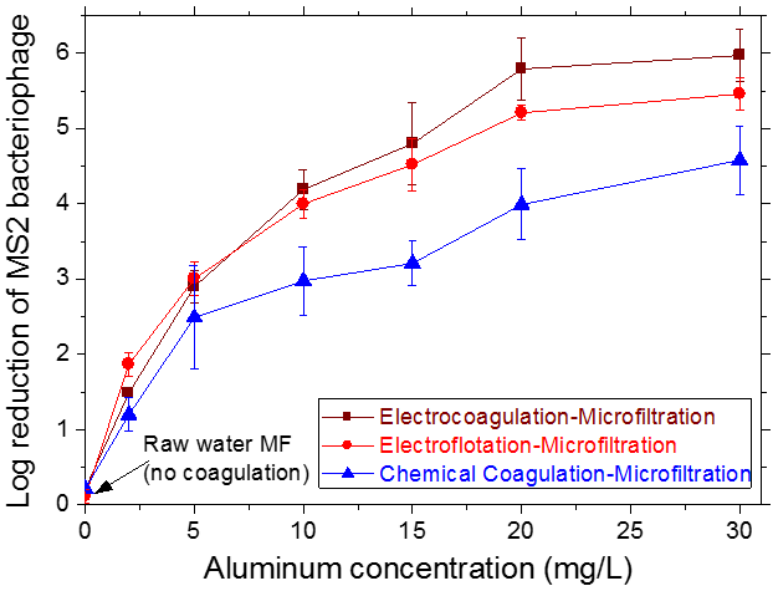

Figure 50. Virus control by combined coagulation pretreatment and MF.

Datapoints are the average of two or three replicate experiments, and error bars correspond to standard deviations of six to nine plaque assays. Each datapoint includes measurements made after filtering 24, 121, and 367 L/m^2 of feed water per unit membrane area, as shown in Figure 51. The spiked virus concentration in the feed water was in the order of 10^8 PFU/mL. Note that zero aluminum concentration corresponds to no coagulant addition.

Electrocoagulation and electroflotation pretreatment removed 5.5–6.0 logs of viruses at highest dosages evaluated, compared with only 4.0–4.5 logs by chemical coagulation. Even at lower dosages, electrochemical treatment

outperformed chemical coagulation. Enhanced virus control by electrochemical pretreatment is attributed to electrophoresis of negatively charged phages, which would have increased their concentrations in the proximity of the anode. (Note that the isoelectric point of MS2 is 3.9, and the solution pH was 6.4; also see Figure 56.) Simultaneously, fresh aluminum precipitates are continually generated in this microenvironment by anodic dissolution. Additionally, hydrolysis of electrochemically generated Al^{3+} ions decreases the local pH, shifting the equilibrium toward other surface-active dissolved monomers and polymers such as $AlOH^{2+}$, $Al(OH)_2^{+}$, $Al_2(OH)_2^{4+}$, $Al_3(OH)_4^{5+}$, etc. [115, 219], which can adsorb readily onto viruses. It is reasonable to suggest that the intermingling of locally high concentrations of viruses, dissolved hydrolysis products, and solid precipitates in the vicinity of the anode during electrolysis promoted destabilization, consequently increasing phage removal compared with conventional alum coagulation, in which concentrations are more uniform.

Additionally, electrocoagulation was slightly more effective than electroflotation —notably at 20- and 30-mg/L dosages, as seen in Figure 50. Insights into this observation were gleaned by monitoring viruses in the permeate water after filtering 2.4, 12.2, and 36.7 cm^3/cm^2 of pretreated waters per unit membrane area. Virus control by electrocoagulation–MF tended to improve with continued filtration of the suspension (Figure 51a), whereas it remained relatively constant following electroflotation–MF (Figure 51b). Therefore, the thicker cake layer formed during MF of electrocoagulated water appears to act as a dynamic membrane, removing additional viruses as filtration progresses. Similar trends in virus removal have also been reported due to accumulation of bacteria or colloidal foulants on microfilters [82, 215, 220]. As may be expected, this effect was more prominent at higher coagulant dosages corresponding to greater mass of precipitates (thicker cake and lower flux). Lower mass loading on the membrane following electroflotation resulted in the formation of thinner cakes, making this effect less pronounced and allowing virus removal to be relatively constant over the duration of MF.

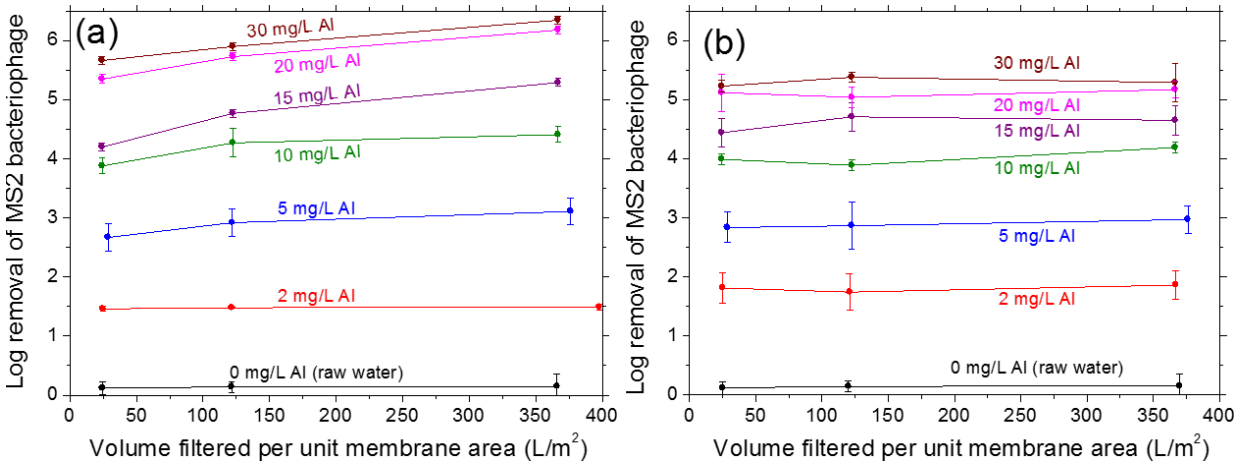

Figure 51. Virus removal over the course of MF following electrocoagulation pretreatment (a) and electroflotation pretreatment (b) at different dosages in the range 0–30 mg/L Al.

Enmeshment of Viruses in Aluminum Precipitates

Direct evidence of virus enmeshment in precipitates was first obtained by epifluorescence microscopy. Figure 52 depicts corresponding bright-field and fluorescence images of the raw water and electrocoagulated flocs in the Al dosage range 2–20 mg/L, incorporating FITC-labeled viruses.

As seen qualitatively in Figure 52, the intensity increased with aluminum dosage. This was quantitatively shown by calculating the average fluorescence intensity over the entire floc area for three different images using Image J software. Hence, more viruses were captured with increasing dosage, consistent with the results presented in Figure 50. X-ray diffractometry has shown that our experiments generate gelatinous and fluffy $Al(OH)_3$ polymorphs during electrocoagulation of surface water [37]. These amorphous precipitates could be initiated around virus nuclei. Additionally, floc growth during slow mixing sweeps out viruses from suspension, while more efficient virus capture occurs through the formation of bigger flocs at higher Al dosages (seen qualitatively in Figure 52 and reported quantitatively in our previous work [37]). As such, sweep flocculation of viruses onto $Al(OH)_3$ aggregates that are larger than the membrane pore size and are subsequently removed during MF is the dominant destabilization and removal mechanism.

Moreover, after selected experiments, flocs were separated by centrifugation (10,000 *g* for 20 minutes) and the pellet was then dissolved in 6-percent beef extract after elevating the pH to 9.5 using NaOH [215, 221]. Flocs were visually observed to be completely dissolved at this pH, thereby releasing the captured viruses. Those viruses were later enumerated along with the viruses that remained in the centrifuged supernatant. Representative results are summarized in Figure 53 for a relatively low (5 mg/L) and high (20 mg/L) Al dosage. Phage concentrations measured soon after adding MS2 stock suspension to the feed water are labeled "seeded feed water." The supernatant, which retained only uncoagulated or free viruses, registered significantly lower concentrations (e.g. 2.0–5.5 logs) than its initial values, representing only a very small fraction (< 0.7%) of the seed. Nearly all the seeded viruses were captured within the solid matrix (compare the 1st and 3rd bars in Figure 53), and this finding confirms that sweep flocculation was the dominant virus destabilization mechanism. The quantitative recovery of MS2 by elution using beef extract at an alkaline pH demonstrates negligible inactivation as well as completely reversible attachment of the viruses onto amorphous $Al(OH)_3$ precipitates during electrocoagulation and chemical coagulation. These results provide a mechanistic basis for the "Standard Method" SM 9510D for virus concentration by aluminum coagulation [221] and simultaneously demonstrate the superiority of electrochemical treatment over alum addition for such purposes (since it achieved higher removals, as seen in Figure 50).

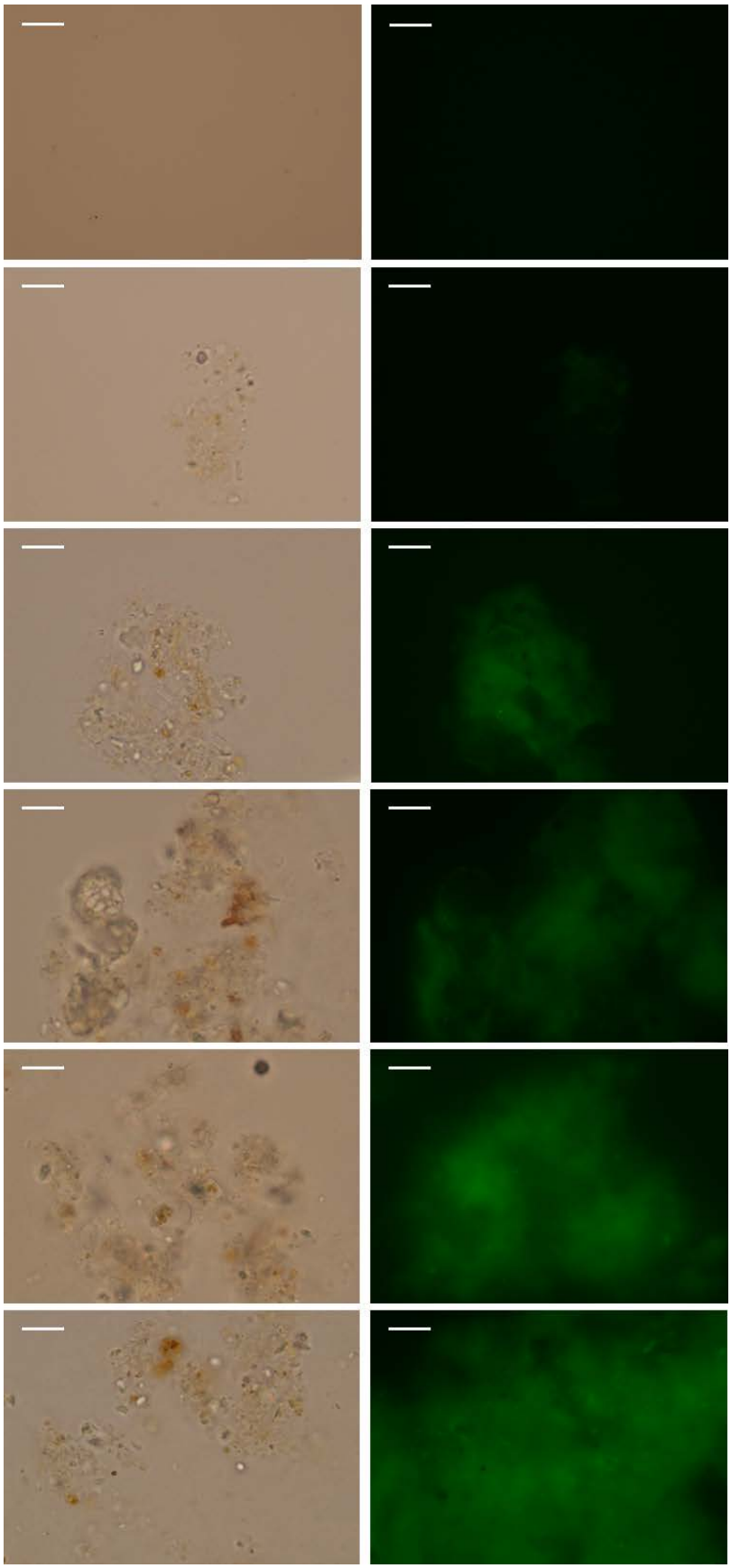

Figure 52. Bright-field (left column) and corresponding epifluorescence images (right column) of electrocoagulated flocs incorporating FITC labeled viruses.

Electrocoagulant dosages from top to bottom are 5, 10, and 20 mg/L Al, respectively. The scale bars equal 10 μm.

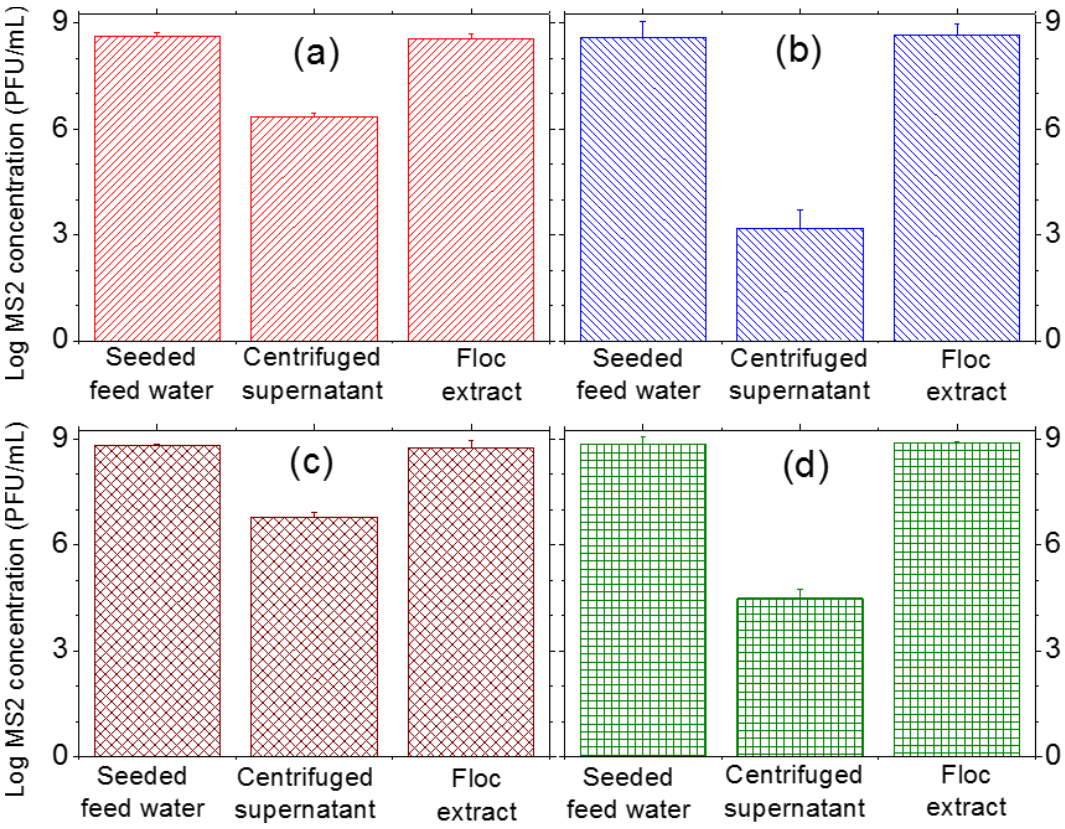

Figure 53. Quantitative recoveries of seeded viruses from flocs.

Representative results for electrocoagulation (a and b) and chemical coagulation (c and d) are shown for 5 and 20 mg/L dosages, respectively. The error bars correspond to one standard deviation of three measurements. The leftmost bars denote the spiked (initial) virus concentrations before coagulation, the middle bars represent uncoagulated free viruses in suspension, and the rightmost bars stand for viruses extracted from the flocs (after coagulation) by dissolving them in beef extract at high pH.

Evidence for Virus Adsorption onto Flocs

Figure 54 depicts representative AFM force pull-off curves generated from the vertical retraction of virus-modified AFM tips from a contacting surface (i.e. floc interface) for flocs generated under a range of aluminum dosages. The adhesion (or unbinding) force was calculated as a product of the maximum AFM tip deflection in the pull-off curve and the cantilever spring constant. Negligible virus (tip)-colloid interactions were observed for the raw water and for water electrocoagulated at the lowest Al dosage investigated (2 mg/L), but adhesion forces progressively increased with electrocoagulant dosage. Pull-off curves at dosages > 5 mg/L exhibited multiple peaks during tip retraction from the floc surface, which is a characteristic trait when macromolecules (e.g. proteins, DNA, polymers, etc.) are used as functional moieties on AFM tips [222–224]. Some of these peaks correspond to multiple pull-off events that occur between protein segments on the viruses that are bound to the surface of the floc (i.e., NOM and heterogeneous precipitates). Other peaks reflect unbinding events that arise through intraprotein bond formation and breakage as the virus is pulled (and

stretched) during tip retraction. Multiple unbinding events have also been reported for rotavirus-NOM interactions [225] and may arise when virus-NOM bonds or calcium/aluminum bridges between viruses and NOM are broken. Such events result from covalent bonding between viruses and functionalized tips. Higher interaction forces also corresponded to unbinding events at greater tip-surface separation distances, presumably due to enhanced proximal binding of protein segments to the substrate. Experimental adhesion forces followed a log-normal distribution in many, but not all cases. The trend of increasing adhesion force with electrocoagulant dosage is consistent in both approaches (independent of the model) and we show the arithmetic mean.

The virus (tip)-floc adhesion force (Figure 55) was calculated at different aluminum dosages by averaging a total of 3,000 individual pull-off curves taken from two separate measurements at 12 different locations on the floc surface for each dosage. Low adhesion forces were measured between the virus-coated AFM tip and colloids in the raw water (0 mg/L) and between the tip and flocs formed at 2 mg/L Al dosage (Figure 55). These low values are attributed to repulsion between viruses and flocs, which are both negatively charged under these conditions, as shown in Figure 56 [99]. Progressive charge neutralization with increasing Al dosage was consistent with adsorption of $Al(OH)^{2+}$, the predominant hydrolysis product at pH 6.4 during our experiments. The ζ potential (or approximate surface charge) of viruses and flocs effectively approached 0 near 10 mg/L and did not increase substantially even as more Al was electrolyzed (i.e., limited restabilization even upon overdosing). Hence, electrostatic interactions appear to explain the monotonic increase in adhesion forces between viruses and flocs as more and more electrocoagulant was added.

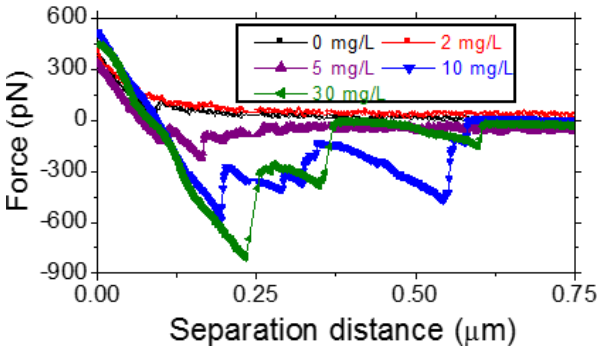

Figure 54. Representative AFM pull-off curves generated during the retraction of MS2-coated tips from the surfaces of flocs incorporating viruses, NOM, and fresh $Al(OH)_3$ precipitates in treated natural surface water.

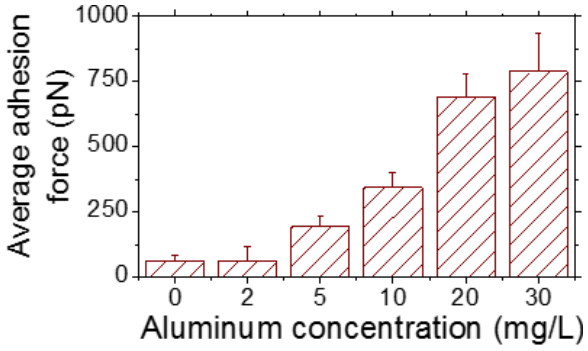

Figure 55. Average (arithmetic mean) adhesion forces between viruses immobilized on AFM tips and the surface of flocs exhibit an increasing trend as the Al dosage is increased in the range 0–30 mg/L.

Concurrent with increasing virus removal, NOM uptake by the flocs and the mass of solids precipitated also increased with electrocoagulant dosage. As shown in Figure 57, similar to alum coagulation [226, 227], electrocoagulation preferentially removed humic substances and higher molecular weight

components of NOM, as evidenced by the higher removal of UV-absorbing substances than of DOC. Even though NOM concentration in the permeate water decreased progressively as more and more aluminum was added, a maximum in NOM removal was observed at 10 mg/L Al (Figure 58). Here we express the amount of NOM adsorbed onto the flocs normalized to cake mass measured after filtering 367 L/m^2 pretreated water. This was due to DOC removal reaching the point of diminishing returns [227] at an electrocoagulant dosage of 10 mg/L (see Figure 51d) whereas the mass of solids precipitated continued to increase with dosage [37]. Effective removal of aromatic (i.e. humics) NOM moieties was verified by the specific UV absorbance (SUVA, absorbance at 254 nm for 1 m path length divided by the DOC concentration expressed in mg/L). Figure 51f depicts the SUVA of NOM captured by the flocs normalized to cake mass measured at the end of the experiment (cumulative filtration of 367 L/m^2), which peaked at an intermediate Al concentration (ca. 5 mg/L). These observations are consistent with floc surfaces becoming more hydrophobic at low dosages, which decreased as more coagulant was added, but were always more hydrophobic than raw water colloids. NOM-coated flocs can more strongly interact with viruses mediated by calcium ions present in the source water or hydrolyzed aluminum species following electrolysis. Therefore, hydrophobic interactions [228] would also have contributed to changes in virus adhesion force with Al dosage, potentially due to formation of Ca/Al inner sphere complexes with COO^- groups located on the MS2 capsid surface (primarily Asp and Glu amino acids).

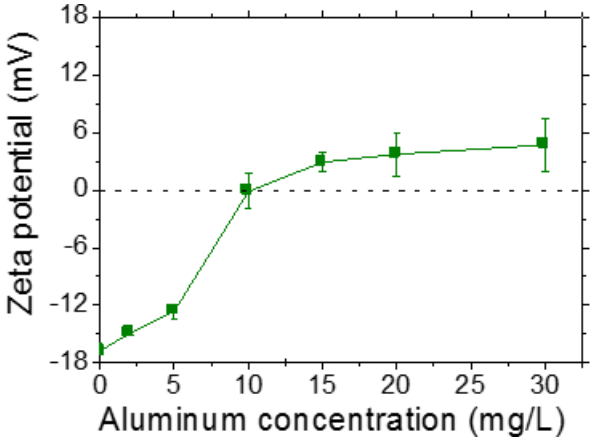

Figure 56. Progressive neutralization of MS2 surface charge (ζ potential → 0) with aluminum addition.

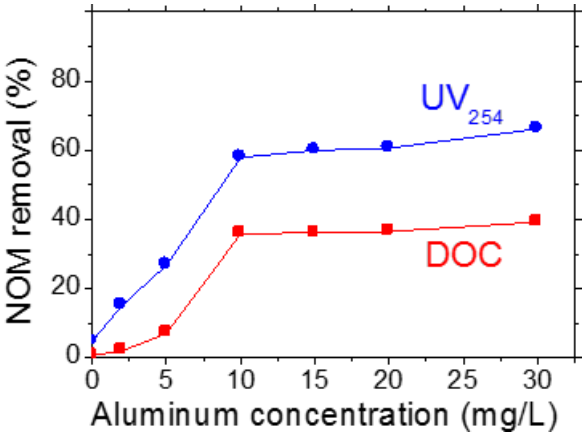

Figure 57. Electrocoagulation preferentially removes UV_{254} absorbing substances compared with DOC.

Higher average adhesion forces measured for dosages ≥5 mg/L during electro-coagulation pretreatment are also consistent with the observed dynamic membrane effect (Figure 51a). In brief, freely suspended and uncoagulated viruses appear to have interacted more strongly with the relatively thick cake as more and more solids were deposited on the microfilter, which ultimately increased their removal as filtration progressed.

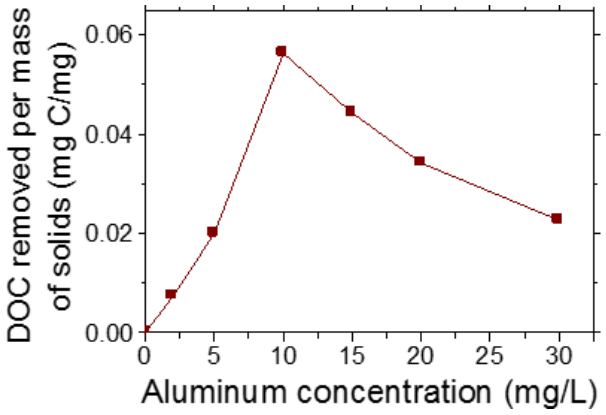

Figure 58. A plot of NOM removal (normalized by total mass of filtered solids) reveals a maximum value at intermediate Al dosage.

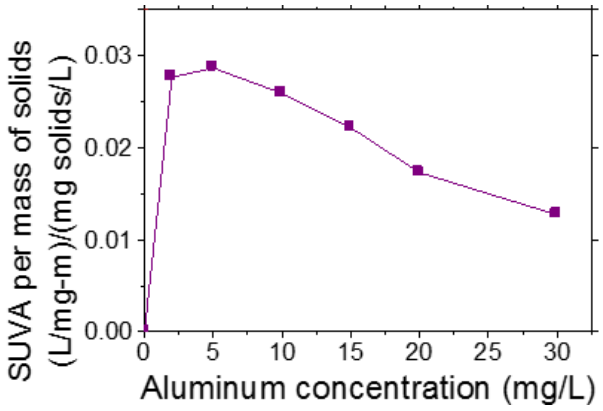

Figure 59. Changes in relative hydrophobicity of flocs using SUVA as a surrogate.

REFERENCES

1. Coplin, L.S., and D. Galloway, *Chapter 7. Houston-Galveston, Texas: Managing coastal subsidence,* in *Land Subsidence in the United States*, D. Galloway, D.R. Jones, and S.E. Ingebritsen, Editors. 1999, U.S. Department of the Interior and U.S. Geological Survey: Reston, VA. p. 35–48.
2. Wiesner, M.R., M.M. Clark, and J. Mallevialle, *Membrane filtration of coagulated suspensions*. Journal of Environmental Engineering, 1989. **115**(1): p. 20–40.
3. Howe, K.J., and M.M. Clark, *Effect of coagulation pretreatment on membrane filtration performance*. Journal American Water Works Association, 2006. **98**(4): p. 133–146.
4. Wiesner, M.R., and J.-M. Laîné, *Coagulation and Membrane Separation, in Water Treatment Membrane Processes*, J. Mallevialle, P.E. Odendaal, and M.R. Wiesner, Editors. 1996, New York: McGraw-Hill.
5. Holt, P.K., G.W. Barton, and C.A. Mitchell, *The future for electro-coagulation as a localised water treatment technology*. Chemosphere, 2005. **59**(3): p. 355–367.
6. Mollah, M.Y.A., P. Morkovsky, J.A.G. Gomes, M. Kesmez, J. Parga, and D.L. Cocke, *Fundamentals, present and future perspectives of electro-coagulation*. Journal of Hazardous Materials, 2004. **114**(1–3): p. 199–210.
7. Moreno, C.H.A., D.L. Cocke, J.A.G. Gomes, P. Morkovsky, J.R. Parga, E. Peterson, and C. Garcia, *Electrochemical reactions for electrocoagulation using iron electrodes*. Industrial & Engineering Chemistry Research, 2009. **48**(4): p. 2275–2282.
8. Cañizares, P., C. Jimenez, F. Martinez, C. Saez, and M.A. Rodrigo, *Study of the electrocoagulation process using aluminum and iron electrodes*. Industrial & Engineering Chemistry Research, 2007. **46**(19): p. 6189–6195.
9. Chen, G., *Electrochemical technologies in wastewater treatment*. Separation and Purification Technology, 2004. **38**(1): p. 11–41.
10. Jiang, J.-Q., N. Graham, C. Andre, G.H. Kelsall, and N. Brandon, *Laboratory study of electro-coagulation-flotation for water treatment*. Water Research, 2002. **36**(16): p. 4064–4078.
11. Cañizares, P., F. Martínez, C. Jiménez, J. Lobato, and M.A. Rodrigo, *Coagulation and electrocoagulation of wastes polluted with dyes*. Environmental Science & Technology, 2006. **40**(20): p. 6418–6424.
12. Mouedhen, G., M. Feki, M.D.P. Wery, and H.F. Ayedi, *Behavior of aluminum electrodes in electrocoagulation process*. Journal of Hazardous Materials, 2008. **150**(1): p. 124–135.
13. Yang, G.C.C., and C.-M. Tsai, *Performance evaluation of a simultaneous electrocoagulation and electrofiltration module for the treatment of Cu-*

CMP and oxide-CMP wastewaters. Journal of Membrane Science, 2006. **286**(1–2): p. 36–44.

14. Mameri, N., A.R. Yeddou, H. Lounici, D. Belhocine, H. Grib, and B. Bariou, *Defluoridation of septentrional Sahara water of north Africa by electrocoagulation process using bipolar aluminium electrodes*. Water Research, 1998. **32**(5): p. 1604–1612.
15. Shen, F., X. Chen, P. Gao, and G. Chen, *Electrochemical removal of fluoride ions from industrial wastewater*. Chemical Engineering Science, 2003. **58**(3–6): p. 987–993.
16. Zhu, B., D.A. Clifford, and S. Chellam, *Comparison of electrocoagulation and chemical coagulation pretreatment for enhanced virus removal using microfiltration membranes*. Water Research, 2005. **39**(13): p. 3098–3108.
17. Holt, P.K., G.W. Barton, M. Wark, and C.A. Mitchell, *A quantitative comparison between chemical dosing and electrocoagulation*. Colloids and Surfaces A: Physicochemical and Engineering Aspects, 2002. **211**(2–3): p. 233–248.
18. Mansouri, K., A. Hannachi, A. Abdel-Wahab, and N. Bensalah, *Electro-chemically dissolved aluminum coagulants for the removal of natural organic matter from synthetic and real industrial wastewaters*. Industrial & Engineering Chemistry Research, 2012. **51**(5): p. 2428–2437.
19. Chen, X., G. Chen, and P.L. Yue, *Separation of pollutants from restaurant wastewater by electrocoagulation*. Separation and Purification Technology, 2000. **19**(1–2): p. 65–76.
20. Bayat, O., O. Kilic, B. Bayat, M. Anil, H. Akarsu, and C. Poole, *Electro-kinetic dewatering of Turkish glass sand plant tailings*. Water Research, 2006. **40**(1): p. 61–66.
21. Durante, C., M. Cuscov, A.A. Isse, G. Sandonà, and A. Gennaro, *Advanced oxidation processes coupled with electrocoagulation for the exhaustive abatement of Cr-EDTA*. Water Research, 2011. **45**(5): p. 2122–2130.
22. Wan, W., T.J. Pepping, T. Banerji, S. Chaudhari, and D.E. Giammar, *Effects of water chemistry on arsenic removal from drinking water by electro-coagulation*. Water Research, 2011. **45**(1): p. 384–392.
23. Lakshmanan, D., D.A. Clifford, and G. Samanta, *Comparative study of arsenic removal by iron using electrocoagulation and chemical coagulation*. Water Research, 2010. **44**(19): p. 5641–5652.
24. Jiang, J.-Q., N. Graham, C. André, G.H. Kelsall, and N. Brandon, *Laboratory study of electro-coagulation-flotation for water treatment*. Water Research, 2002. **36**(16): p. 4064–4078.
25. Ricordel, C., A. Darchen, and D. Hadjiev, *Electrocoagulation-electro-flotation as a surface water treatment for industrial uses*. Separation and Purification Technology, 2010. **74**(3): p. 342–347.

26. Ben Sasson, M., and A. Adin, *Fouling mitigation by iron-based electro-flocculation in microfiltration: Mechanisms and energy minimization*. Water Research, 2010. **44**(13): p. 3973–3981.

27. Mavrov, V., S. Stamenov, E. Todorova, H. Chmiel, and T. Erwe, *New hybrid electrocoagulation membrane process for removing selenium from industrial wastewater*. Desalination, 2006. **201**(1–3): p. 290–296.

28. Chen, X., G. Chen, and P.L. Yue, *Novel electrode system for electro-flotation of wastewater*. Environmental Science & Technology, 2002. **36**(4): p. 778–783.

29. Gamage, N.P., J.D. Rimer, and S. Chellam, *Improvements in permeate flux by aluminum electroflotation pretreatment during constant pressure microfiltration of surface water*. Journal of Membrane Science, 2012. **411–412**: p. 45–53.

30. Timmes, T.C., H.-C. Kim, and B.A. Dempsey, *Electrocoagulation pretreatment of seawater prior to ultrafiltration: Pilot-scale applications for military water purification systems*. Desalination, 2010. **250**(1): p. 6–13.

31. Timmes, T.C., H.-C. Kim, and B.A. Dempsey, *Electrocoagulation pretreatment of seawater prior to ultrafiltration: Bench-scale applications for military water purification systems*. Desalination, 2009. **249**(3): p. 895–901.

32. Bagga, A., S. Chellam, and D. Clifford, *Evaluation of iron chemical coagulation and electrocoagulation pretreatment for surface water microfiltration*. Journal of Membrane Science, 2008. **309**(1–2): p. 82–93.

33. Ben Sasson, M., and A. Adin, *Fouling mechanisms and energy appraisal in microfiltration pretreated by aluminum-based electroflocculation*. Journal of Membrane Science, 2010. **352**(1–2): p. 86–94.

34. Canizares, P., M. Carmona, J. Lobato, F. Martinez, and M.A. Rodrigo, *Electrodissolution of aluminum electrodes in electrocoagulation processes*. Industrial & Engineering Chemistry Research, 2005. **44**(12): p. 4178–4185.

35. Mollah, M.Y.A., R. Schennach, J.R. Parga, and D.L. Cocke, *Electro-coagulation (EC)—science and applications*. Journal of Hazardous Materials, 2001. **84**(1): p. 29–41.

36. Sarkar, M.S.K.A., G.M. Evans, and S.W. Donne, *Bubble size measurement in electroflotation*. Minerals Engineering, 2010. **23**(11–13): p. 1058–1065.

37. Gamage, N.P., and S. Chellam, *Aluminum electrocoagulation pretreatment reduces fouling during surface water microfiltration*. Journal of Membrane Science, 2011. **379**(1–2): p. 97–105.

38. Lahoussine-Turcaud, V., M.R. Wiesner, J.Y. Bottero, and J. Mallevialle, *Coagulation pretreatment for ultrafiltration of a surface water*. Journal American Water Works Association, 1990. **82**(12): p. 76–81.

39. Huang, H., K. Schwab, and J.G. Jacangelo, *Pretreatment for low pressure membranes in water treatment: A review*. Environmental Science & Technology, 2009. **43**(9): p. 3011–3019.

40. Wiesner, M., M. Clark, and J. Mallevialle, *Membrane filtration of coagulated suspensions*. Journal of Environmental Engineering, 1989. **115**(1): p. 20–40.

41. Choi, K.Y.J., and B.A. Dempsey, *In-line coagulation with low-pressure membrane filtration*. Water Research, 2004. **38**(19): p. 4271–4281.

42. Schäfer, A.I., A.G. Fane, and T.D. Waite, *Cost factors and chemical pretreatment effects in the membrane filtration of waters containing natural organic matter*. Water Research, 2001. **35**(6): p. 1509–1517.

43. Judd, S.J., and P. Hillis, *Optimisation of combined coagulation and microfiltration for water treatment*. Water Research, 2001. **35**(12): p. 2895–2904.

44. Gamage, N.P., J.D. Rimer, and S. Chellam, *Improvements in permeate flux by aluminum electroflotation pretreatment during microfiltration of surface water*. Journal of Membrane Science, 2012. **411–412**(0): p. 45–53.

45. Laine, J.-M., J.P. Hagstrom, M.M. Clark, and J. Mallevialle, *Effects of ultrafiltration membrane composition*. Journal American Water Works Association, 1989. **81**(11): p. 61–67.

46. Kim, H.-C., and B.A. Dempsey, *Effects of wastewater effluent organic materials on fouling in ultrafiltration*. Water Research, 2008. **42**(13): p. 3379–3384.

47. Howe, K.J., and M.M. Clark, *Fouling of microfiltration and ultrafiltration membranes by natural waters*. Environmental Science & Technology, 2002. **36**(16): p. 3571–3576.

48. Gu, B., J. Schmitt, Z. Chen, L. Liang, and J.F. McCarthy, *Adsorption and desorption of natural organic matter on iron oxide: Mechanisms and models*. Environmental Science & Technology, 1994. **28**(1): p. 38–46.

49. Peldszus, S., C. Hallé, R.H. Peiris, M. Hamouda, X. Jin, R.L. Legge, H. Budman, C. Moresoli, and P.M. Huck, *Reversible and irreversible low-pressure membrane foulants in drinking water treatment: Identification by principal component analysis of fluorescence EEM and mitigation by biofiltration pretreatment.* Water Research, 2011. **45**(16): p. 5161–5170.

50. Yamamura, H., K. Kimura, and Y. Watanabe, *Mechanism involved in the evolution of physically irreversible fouling in microfiltration and ultrafiltration membranes used for drinking water treatment*. Environmental Science & Technology, 2007. **41**(19): p. 6789–6794.

51. Choi, K.Y.-J., and B.A. Dempsey, *Bench-scale evaluation of critical flux and TMP in low-pressure membrane filtration*. Journal of the American Water Works Association, 2005. **97**(7): p. 134–143.

52. Chellam, S., and J. Jacangelo, *Existence of critical recovery and impacts of operational mode on potable water microfiltration*. Journal of Environmental Engineering, 1998. **124**(12): p. 1211–1219.

53. Chellam, S., J.G. Jacangelo, and T.P. Bonacquisti, *Modeling and experimental verification of pilot-scale hollow fiber, direct flow microfiltration with periodic backwashing*. Environmental Science & Technology, 1998. **32**(1): p. 75–81.

54. Chellam, S., and W. Xu, *Blocking laws analysis of dead-end constant flux microfiltration of compressible cakes*. Journal of Colloid and Interface Science, 2006. **301**(1): p. 248–257.

55. Tiller, F.M., and J.H. Kwon, *Role of porosity in filtration: XIII. Behavior of highly compactible cakes*. AIChE Journal, 1998. **44**(10): p. 2159–2167.

56. Tiller, F.M., C.S. Yeh, and W.F. Leu, *Compressibility of particulate structures in relation to thickening, filtration, and expression—a review*. Separation Science and Technology, 1987. **22**(2–3): p. 1037–1063.

57. Sørensen, B.L., and P.B. Sorensen, *Applying cake filtration theory on membrane filtration data*. Water Research, 1997. **31**(3): p. 665–670.

58. Lee, S.A., A.G. Fane, R. Amal, and T.D. Waite, *The effect of floc size and structure on specific cake resistance and compressibility in dead-end microfiltration*. Separation Science and Technology, 2003. **38**(4): p. 869–887.

59. Lee, S.A., A.G. Fane, and T.D. Waite, *Impact of natural organic matter on floc size and structure effects in membrane filtration*. Environmental Science & Technology, 2005. 39(17): p. 6477–6486.

60. Waite, T.D., A.I. Schäfer, A.G. Fane, and A. Heuer, *Colloidal fouling of ultrafiltration membranes: Impact of aggregate structure and size*. Journal of Colloid and Interface Science, 1999. **212**(2): p. 264–274.

61. Park, P.-K., C.-H. Lee, and S. Lee, *Permeability of collapsed cakes formed by deposition of fractal aggregates upon membrane filtration*. Environmental Science & Technology, 2006. **40**(8): p. 2699–2705.

62. Antelmi, D., B. Cabane, M. Meireles, and P. Aimar, *Cake collapse in pressure filtration*. Langmuir, 2001. **17**(22): p. 7137–7144.

63. Wang, J., J. Guan, S.R. Santiwong, and T.D. Waite, *Effect of aggregate characteristics under different coagulation mechanisms on microfiltration membrane fouling*. Desalination, 2010. **258**(1–3): p. 19–27.

64. Lee, J.-D., S.-H. Lee, M.-H. Jo, P.-K. Park, C.-H. Lee, and J.-W. Kwak, *Effect of coagulation conditions on membrane filtration characteristics in coagulation−microfiltration process for water treatment*. Environmental Science & Technology, 2000. **34**(17): p. 3780–3788.

65. Van der Bruggen, B., K. Everaert, D. Wilms, and C. Vandecasteele, *Application of nanofiltration for removal of pesticides, nitrate and hardness*

from ground water: Rejection properties and economic evaluation. Journal of Membrane Science, 2001. **193**(2): p. 239–248.

66. Semião, A.J.C., and A.I. Schäfer, *Xenobiotics removal by membrane technology: An overview*, in *Xenobiotics in the Urban Water Cycle: Mass Flows, Environmental Processes and Mitigation Strategies*, K. Bester, K. Kümmerer, and D. Fatta-Kassinos, Editors. 2012, Springer: Berlin, Germany.

67. Yangali-Quintanilla, V., S.K. Maeng, T. Fujioka, M. Kennedy, and G. Amy, *Proposing nanofiltration as acceptable barrier for organic contaminants in water reuse*. Journal of Membrane Science, 2012. **362**(1–2): p. 334–345.

68. Chellam, S., J.G. Jacangelo, T.P. Bonacquisti, and B.A. Schauer, *Effect of pretreatment on surface water nanofiltration*. Journal of American Water Works Association, 1997. **89**(10): p. 77–89.

69. Nederlof, M.M., J.C. Kruithof, J.S. Taylor, D. van der Kooij, and J.C. Schippers, *Comparison of NF/RO membrane performance in integrated membrane systems*. Desalination, 2000. **131**(1–3): p. 257–269.

70. Van der Bruggen, B., D. Segers, C. Vandecasteele, L. Braeken, a. Volodin, and C. Van Haesendonck, *How a microfiltration pretreatment affects the performance in nanofiltration*. Separation Science and Technology, 2005. **39**(7): p. 1443–1459.

71. Wiesner, M.R., and J.-M. Laine, *Coagulation and Membrane Separation, in Water Treatment Membrane Processes*, J. Mallevialle, P.E. Odendaal, and M.R. Wiesner, Editors. 1996, New York: McGraw Hill. p. 16,1–16,12.

72. Mansouri, K., K. Ibrik, N. Bensalah, and A. Abdel-Wahab, Anodic *Dissolution of pure aluminum during electrocoagulation process: Influence of supporting electrolyte, initial pH, and current density*. Industrial & Engineering Chemistry Research, 2011. **50**(23): p. 13362–13372.

73. Xu, P., C. Bellona, and J.E. Drewes, *Fouling of nanofiltration and reverse osmosis membranes during municipal wastewater reclamation: Membrane autopsy results from pilot-scale investigations*. Journal of Membrane Science, 2010. **353**(1–2): p. 111–121.

74. Park, N., B. Kwon, S.-D. Kim, and J. Cho, *Characterizations of the colloidal and microbial organic matters with respect to membrane foulants*. Journal of Membrane Science, 2006. **275**(1–2): p. 29–36.

75. Xu, P., J.E. Drewes, T.-U. Kim, C. Bellona, and G. Amy, *Effect of membrane fouling on transport of organic contaminants in NF/RO membrane applications*. Journal of Membrane Science, 2006. **279**(1–2): p. 165–175.

76. Chang, E.E., Y.-W. Chen, Y.-L. Lin, and P.-C. Chiang, *Reduction of natural organic matter by nanofiltration process*. Chemosphere, 2009. **76**(9): p. 1265–72.

77. Madaeni, S.S., *The application of membrane technology for water disinfection*. Water Research, 1999. **33**(2): p. 301–308.

78. Ramani, S., and G. Kang, *Viruses causing childhood diarrhoea in the developing world*. Current Opinion in Infectious Diseases, 2009. **22**(5): p. 477–482.

79. Environmental Protection Agency, *National Primary Drinking Water Regulations: Ground Water Rule; Final Rule*, 2006, Federal Register, 40 CFR Parts 9, 141, and 142. p. 65574–65660.

80. Urase, T., K. Yamamoto, and S. Ohgaki, *Effect of pore structure of membranes and module configuration on virus retention*. Journal of Membrane Science, 1996. **115**(1): p. 21–29.

81. Jacangelo, J.G., S.S. Adham, and J.-M. Laîné, *Mechanism of Cryptosporidium, Giardia, and MS2 virus removal by MF and UF*. Journal American Water Works Association, 1995. **87**(9): p. 107–121.

82. Madaeni, S.S., A.G. Fane, and G.S. Grohmann, *Virus removal from water and wastewater using membranes*. Journal of Membrane Science, 1995. **102**: p. 65–75.

83. Mi, B., B.J. Marinas, J. Curl, S. Sethi, G. Crozes, and D. Hugaboom, *Microbial passage in low pressure membrane elements with compromised integrity*. Environmental Science & Technology, 2005. **39**(11): p. 4270–4279.

84. Pontius, F.W., G.L. Amy, and M.T. Hernandez, *Fluorescent microspheres as virion surrogates in low-pressure membrane studies*. Journal of Membrane Science, 2009. **335**(1–2): p. 43–50.

85. van Voorthuizen, E.M., N.J. Ashbolt, and A.I. Schäfer, *Role of hydrophobic and electrostatic interactions for initial enteric virus retention by MF membranes*. Journal of Membrane Science, 2001. **194**(1): p. 69–79.

86. Fiksdal, L., and T. Leiknes, *The effect of coagulation with MF/UF membrane filtration for the removal of virus in drinking water*. Journal of Membrane Science, 2006. **279**(1–2): p. 364–371.

87. Zhu, B., D.A. Clifford, and S. Chellam, *Virus removal by iron coagulation-microfiltration*. Water Research, 2005. **39**(20): p. 5153–5161.

88. Shirasaki, N., T. Matsushita, Y. Matsui, M. Kobuke, and K. Ohno, *Comparison of removal performance of two surrogates for pathogenic waterborne viruses, bacteriophage Qb and MS2, in a coagulation-ceramic microfiltration system*. Journal of Membrane Science, 2009. **326**(2): p. 564–571.

89. Mayer, B.K., H. Ryu, and M. Abbaszadegan, *Treatability of U.S. Environmental Protection Agency contaminant candidate list viruses: Removal of Coxsackievirus and Echovirus using enhanced coagulation*. Environmental Science & Technology, 2008. **42**(18): p. 6890–6896.

90. Havelaar, A.H., M. Olphen van, and Y.C. Drost, *F-specific RNA bacteriophages are adequate model organisms for enteric viruses in fresh water*. Applied and Environmental Microbiology, 1993. **59**(9): p. 2956–2962.

91. Grabow, W.O.K., *Bacteriophages: Update on application as models for viruses in water*. Water SA, 2001. 27(2): p. 251–268.

92. Meyn, T., T.O. Leiknes, and A. König, *MS2 removal from high NOM content surface water by coagulation—Ceramic microfiltration for potable water production*. AIChE Journal, 2012. **58**(7): p. 2270–2281.

93. Shirasaki, N., T. Matsushita, Y. Matsui, M. Kobuke, and K. Ohno, *Comparison of removal performance of two surrogates for pathogenic waterborne viruses, bacteriophage Qb and MS2 in a coagulation-ceramic microfiltration system*. Journal of Membrane Science, 2009. **326**(2): p. 564–571.

94. Jacangelo, J.G., S.S. Adham, and J.M. Laine, *Mechanism of Cryptosporidium, Giardia, and MS2 virus removal by MF and UF*. Journal of the American Water Works Association, 1995. **87**(10): p. 107–121.

95. Hendricks, D.W., W.F. Clunie, G.D. Sturbaum, D.A. Klein, T.L. Champlin, P. Kugrens, J. Hirsch, B. McCourt, G.R. Nordby, M.D. Sobsey, D.J. Hunt, and M.J. Allen, *Filtration removals of microorganisms and particles*. Journal of Environmental Engineering, 2005. **131**(12): p. 1621–1632.

96. Harrington, G.W., I. Xagoraraki, P. Assavasilavasukul, and J.H. Stanridge, *Effect of filtration conditions on removal of emerging waterborne pathogens*. Journal of the American Water Works Association, 2003. **95**(12): p. 95–104.

97. Abbaszadegan, M., B.K. Mayer, H. Ryu, and N. Nwachuku, *Efficacy of removal of CCL viruses under enhanced coagulation conditions*. Environmental Science & Technology, 2007. **41**(3): p. 971–977.

98. Mayer, B.K., H. Ryu, and M. Abbaszadegan, *Treatability of US Environmental Protection Agency contaminant candidate list viruses: Removal of coxsackievirus and echovirus using enhanced coagulation*. Environmental Science & Technology, 2008. **42**(18): p. 6890–6896.

99. Attinti, R., J. Wei, K. Kniel, J.T. Sims, and Y. Jin, *Virus (MS2, fX174, and Aichi) attachment on sand measured by atomic force microscopy and their transport through sand columns*. Environmental Science & Technology, 2010. **44**(7): p. 2426–2432.

100. Badireddy, A.R., S. Chellam, P.L. Gassman, M.H. Engelhard, A.S. Lea, and K.M. Rosso, *Role of extracellular polymeric substances in bioflocculation of activated sludge microorganisms under glucose-controlled conditions*. Water Research, 2010. **44**(15): p. 4505–4516.

101. Kimura, K., Y. Hane, Y. Watanabe, G. Amy, and N. Ohkuma, *Irreversible membrane fouling during ultrafiltration of surface water*. Water Research, 2004. **38**(14–15): p. 3431–3441.

102. Kimura, K., T. Maeda, H. Yamamura, and Y. Watanabe, *Irreversible membrane fouling in microfiltration membranes filtering coagulated surface water*. Journal of Membrane Science, 2008. **320**(1–2): p. 356–362.

103. Sharma, R.R., R. Agrawal, and S. Chellam, *Temperature effects on sieving characteristics of thin-film composite nanofiltration membranes: Pore size distributions and transport parameters*. Journal of Membrane Science, 2003. **223**: p. 69–87.

104. DiGiano, F.A., S. Arweiler, and J.A. Riddick, Jr., *Alternative tests for evaluating NF fouling*. Journal of American Water Works Association, 2000. **92**(2): p. 103–115.

105. Bushell, G.C., Y.D. Yan, D. Woodfield, J. Raper, and R. Amal, *On techniques for the measurement of the mass fractal dimension of aggregates*. Advances in Colloid and Interface Science, 2002. **95**(1): p. 1–50.

106. Jarvis, P., B. Jefferson, and S. Parsons, *Measuring floc structural characteristics*. Reviews in Environmental Science and Biotechnology, 2005. **4**(1): p. 1–18.

107. Harif, T., and A. Adin, *Size and structure evolution of kaolin-Al(OH)$_3$ flocs in the electroflocculation process: A study using static light scattering*. Water Research, 2011. **45**(18): p. 6195–6206.

108. Amal, R., J.A. Raper, and T.D. Waite, *Fractal structure of hematite aggregates*. Journal of Colloid and Interface Science, 1990. **140**(1): p. 158–168.

109. Guan, J., T.D. Waite, and R. Amal, *Rapid structure characterization of bacterial aggregates*. Environmental Science & Technology, 1998. **32**(23): p. 3735–3742.

110. Roček, J., K.H. Heeg, U. Steinike, and K. Jirátová, *Porous structure of aluminium hydroxide and its content of pseudoboehmite*. Applied Catalysis, 1991. **74**(1): p. 29–36.

111. Kim, J.Y., C. Lee, D.C. Love, D.L. Sedlak, J. Yoon, and K.L. Nelson, *Inactivation of MS2 coliphage by ferrous ion and zero-valent iron nanoparticles*. Environmental Science & Technology, 2011. **45**(16): p. 6978–6984.

112. Langlet, J., L. Ogorzaly, J.-C. Schrotter, C. Machinal, F. Gaboriaud, J.F.L. Duval, and C. Gantzer, *Efficiency of MS2 phage and Qb phage removal by membrane filtration in water treatment: Applicability of real-time RT-PCR method*. Journal of Membrane Science, 2009. **326**(1): p. 111–116.

113. Anders, R., and C.V. Chrysikopoulos, *Evaluation of the factors controlling the time-dependent inactivation rate coefficients of bacteriophage MS2 and PRD1*. Environmental Science & Technology, 2006. **40**(10): p. 3237–3242.

114. Shen, C., M.S. Phanikumar, T.T. Fong, I. Aslam, S.P. McElmurry, S.L. Molloy, and J.B. Rose, *Evaluating bacteriophage P22 as a tracer in a complex surface water system: The Grand River, Michigan*. Environmental Science & Technology, 2008. **42**(7): p. 2426–2431.

115. O'Melia, C.R., *Chapter 2. Coagulation and Flocculation, in Physicochemical Processes for Water Quality Control*, W.J. Weber, Editor 1972, New York: Wiley-Interscience. p. 61–109.

116. Duan, J., and J. Gregory, *Coagulation by hydrolysing metal salts*. Advances in Colloid and Interface Science, 2003. **100–102**: p. 475–502.

117. Gomes, J.A.G., P. Daida, M. Kesmez, M. Weir, H. Moreno, J.R. Parga, G. Irwin, H. McWhinney, T. Grady, E. Peterson, and D.L. Cocke, *Arsenic removal by electrocoagulation using combined Al-Fe electrode system and characterization of products*. Journal of Hazardous Materials, 2007. **139**(2): p. 220–231.

118. Emamjomeh, M.M., and M. Sivakumar, *Denitrification using a monopolar electrocoagulation/flotation (ECF) process*. Journal of Environmental Management, 2009. **91**(2): p. 516–522.

119. Berkowitz, J., M.A. Anderson, and R.C. Graham, *Laboratory investigation of aluminum solubility and solid-phase properties following alum treatment of lake waters*. Water Research, 2005. **39**(16): p. 3918–3928.

120. Mollah, M.Y.A., J.A.G. Gomes, K.K. Das, and D.L. Cocke, *Electro-chemical treatment of Orange II dye solution—Use of aluminum sacrificial electrodes and floc characterization*. Journal of Hazardous Materials, 2010. **174**(1–3): p. 851–858.

121. Masion, A., J.Y. Bottero, F. Thomas, and D. Tchoubar, *Chemistry and Structure of Al(OH)/Organics Precipitates. A Small-Angle X-ray Scattering Study. 2. Speciation and Structure of the Aggregates*. Langmuir, 1994. **10**(11): p. 4349–4352.

122. Violante, A., and P.M. Huang, *Influence of inorganic and organic ligands on the formation of aluminum hydroxides and oxyhydroxides*. Clays and Clay Minerals, 1985. **33**(3): p. 181–192.

123. Al-Malack, M.H., A.A. Bukhari, and N.S. Abuzaid, *Crossflow microfiltration of electrocoagulated kaolin suspension: Fouling mechanism*. Journal of Membrane Science, 2004. **243**(1–2): p. 143–153.

124. Zhao, B., D. Wang, T. Li, C.W.K. Chow, and C. Huang, *Influence of floc structure on coagulation-microfiltration performance: Effect of Al speciation characteristics of PACls*. Separation and Purification Technology, 2010. **72**(1): p. 22–27.

125. Belfort, G., R.H. Davis, and A.L. Zydney, *The Behavior of Suspensions and Macromolecular Solutions in Crossflow Microfiltration*. Journal of Membrane Science, 1994. **96**: p. 1–58.

126. Tiller, F.M., C.S. Yeh, and W.F. Leu, *Compressibility of particulate suspensions in relation to thickening, filtration, and expression - A review*. Separation Science and Technology, 1987. **22**(2–3): p. 1037–1063.

127. Chellam, S., and J.G. Jacangelo, *Existence of critical recovery and impacts of operational mode on potable water microfiltration*. Journal of Environmental Engineering, 1998. **124**(12): p. 1211–1219.

128. Tarabara, V.V., R.M. Hovinga, and M.R. Wiesner, *Constant transmembrane pressure vs. constant permeate flux: Effect of particle size on crossflow membrane filtration*. Environmental Engineering Science, 2002. **19**(6): p. 343–355.

129. Badireddy, A.R., B.R. Korpol, S. Chellam, P.L. Gassman, M.H. Engelhard, A.S. Lea, and K.M. Rosso, *Spectroscopic characterization of extracellular polymeric substances from Escherichia coli and Serratia marcescens: Suppression using sub-inhibitory concentrations of bismuth thiols*. Biomacromolecules, 2008. **9**(11): p. 3079–3089.

130. Tipping, E., *The adsorption of aquatic humic substances by iron oxides*. Geochimica et Cosmochimica Acta, 1981. **45**(2): p. 191–199.

131. Tesson, B., M.J. Genet, V. Fernandez, S. Degand, P.G. Rouxhet, and V. Martin-Jézéquel, *Surface chemical composition of diatoms*. ChemBioChem, 2009. **10**(12): p. 2011–2024.

132. Cao, Z., J. Liu, and H. Liu, *Transparent fused silica to model natural sand*, in *Pan-Am CGS Geotechnical Conference.* 2011.

133. Crist, V.B., *Handbook of Monochromatic XPS Spectra*, v. 2. 2005, California: XPS International LLC.

134. Kloprogge, J.T., L.V. Duong, B.J. Wood, and R.L. Frost, *XPS study of the major minerals in bauxite: Gibbsite, bayerite and (pseudo-)boehmite*. Journal of Colloid and Interface Science, 2006. **296**(2): p. 572–576.

135. Guan, X.-h., G.-h. Chen, and C. Shang, *ATR-FTIR and XPS study on the structure of complexes formed upon the adsorption of simple organic acids on aluminum hydroxide*. Journal of Environmental Sciences, 2007. **19**(4): p. 438–443.

136. Vahedi, A., and B. Gorczyca, *Application of fractal dimensions to study the structure of flocs formed in lime softening process*. Water Research, 2010. **45**(2): p. 545–556.

137. Bagga, A., S. Chellam, and D.A. Clifford, *Evaluation of iron chemical coagulation and electrocoagulation pretreatment for surface water microfiltration*. Journal of Membrane Science, 2008. **309**(1–2): p. 82–93.

138. Hermia, J., *Constant Pressure Blocking Filtration Laws - Application to Power-Law Non-Newtonian Fluids*. Transactions of the Institution of Chemical Engineers, 1982. **60**(3): p. 183–187.

139. Xu, W.D., and S. Chellam, *Initial stages of bacterial fouling during dead-end microfiltration*. Environmental Science & Technology, 2005. **39**(17): p. 6470–6476.

140. Tiller, F.M., C.S. Yeh, and W.F. Leu, *Compressibility of particulate structures in relation to thickening, filtration, and expression—A review* 1987. Separation Science and Technology, 1987. **22**(2&3), 1037–1063.

141. Riviáere, J.C., and S. Myhra, *Handbook of Surface and Interface Analysis: Methods for Problem-Solving*. 1998, New York: Marcel Dekker.

142. Ratner, B.D., and S.C. Porter, *Chapter 3: Surfaces in Biology and Biomaterials: Description and Characterization, in Interfacial Phenomena and Bioproducts*, J.L. Brash and P.W. Wojciechowski, Editors. 1996, New York: Marcel-Dekker.

143. Lee, N., G. Amy, and J.-P. Croué, *Low-pressure membrane (MF/UF) fouling associated with allochthonous versus autochthonous natural organic matter*. Water Research, 2006. **40**(12): p. 2357–2368.

144. Thurman, E.M., *Organic Geochemistry of Natural Waters. Developments in Biogeochemistry*. 1985, Boston and Hingham, MA: M. Nijhoff; Distributors for the U.S. and Canada, Kluwer Academic. 497.

145. Her, N., G. Amy, D. Foss, J. Cho, Y. Yoon, and P. Kosenka, *Optimization of Method for Detecting and Characterizing NOM by HPLC−Size Exclusion Chromatography with UV and On-Line DOC Detection*. Environmental Science & Technology, 2002. **36**(5): p. 1069–1076.

146. Wang, L., R. Miao, X. Wang, Y. Lv, X. Meng, Y. Yang, D. Huang, L. Feng, Z. Liu, and K. Ju, *Fouling Behavior of Typical Organic Foulants in Polyvinylidene Fluoride Ultrafiltration Membranes: Characterization from Microforces*. Environmental Science & Technology, 2013. **47**(8): p. 3708–3714.

147. Collins, M.R., G.L. Amy, and C. Steelink, *Molecular weight distribution, carboxylic acidity, and humic substances content of aquatic organic matter: implications for removal during water treatment*. Environmental Science & Technology, 1986. **20**(10): p. 1028–1032.

148. Omoike, A.I., and G.W. vanLoon, *Removal of phosphorus and organic matter removal by alum during wastewater treatment*. Water Research, 1999. **33**(17): p. 3617–3627.

149. Biber, M.V., and W. Stumm, *An in situ ATR-FTIR study: The surface coordination of salicylic acid on aluminum and iron(III) oxides*. Environmental Science & Technology, 1994. **28**(5): p. 763–768.

150. Gao, X., D.W. Metge, C. Ray, R.W. Harvey, and J. Chorover, *Surface complexation of carboxylate adheres Cryptosporidium parvum öocysts to the hematite-water interface*. Environmental Science & Technology, 2009. **43**(19): p. 7423–7429.

151. Mouvenchery, Y.K., J. Kucerik, D. Diehl, and G.E. Schaumann, *Cation-mediated cross-linking in natural organic matter: A review*. Reviews in Environmental Science and Bio-Technology, 2012. **11**(1): p. 41–54.

152. Nakamoto, K., *Infrared and Raman Spectra of Inorganic and Coordination Compounds, Part. B: Applications in Coordination, Organometallic, and Bioinorganic Chemistry*. 2009, Hoboken, NJ: Wiley.

153. Sposito, G., *The Environmental Chemistry of Aluminum*, 2d ed. 1996, Boca Raton, FL: Lewis Publishers.

154. Ahn, W.-Y., A.G. Kalinichev, and M.M. Clark, *Effects of background cations on the fouling of polyethersulfone membranes by natural organic matter: Experimental and molecular modeling study*. Journal of Membrane Science, 2008. **309**(1–2): p. 128–140.

155. Kim, H.-C., and B.A. Dempsey, *Removal of organic acids from EfOM using anion exchange resins and consequent reduction of fouling in UF and MF*. Journal of Membrane Science, 2010. **364**(1–2): p. 325–330.

156. Alexander, M.R., G. Beamson, C.J. Blomfield, G. Leggett, and T.M. Duc, *Interaction of carboxylic acids with the oxyhydroxide surface of aluminium: poly(acrylic acid), acetic acid and propionic acid on pseudoboehmite*. Journal of Electron Spectroscopy and Related Phenomena, 2001. **121**(1–3): p. 19–32.

157. Lu, X., Z. Chen, and X. Yang, *Spectroscopic study of aluminium speciation in removing humic substances by Al coagulation*. Water Research, 1999. **33**(15): p. 3271–3280.

158. Stumm, W., *Chemistry of the Solid-Water Interface: Processes at the Mineral-Water and Particle-Water Interface in Natural Systems*. 1992, New York: Wiley.

159. Adu-Wusu, K., and W.R. Wilcox, *Sorption and desorption isotherms for silicate on gibbsite*. Journal of Colloid and Interface Science, 1991. **143**(1): p. 139–145.

160. Tanneru, C.T., J.D. Rimer, and S. Chellam, *Sweep flocculation and adsorption of viruses on aluminum flocs during electrochemical treatment prior to surface water microfiltration*. Environmental Science & Technology, 2013. **47**(9): p. 4612–4618.

161. Howe, K.J., and M.M. Clark, *Effect of coagulation pretreatment on membrane filtration performance*. Journal of the American Water Works Association, 2006. **98**(4): p. 133–146.

162. Klug, H.P., and L.E. Alexander, *X-Ray Diffraction Procedures: For Polycrystalline and Amorphous Materials*, second ed. 1974, New York: Wiley-Interscience. 992.

163. Newcombe, G., and D. Dixon, *Interface Science In Drinking Water Treatment: Theory and Applications*. 2006, London, Academic Press (Elsevier Ltd.). Interface Science and Technology, v.10. 365 p.

164. Letterman, R.D., and S.G. Vanderbrook, *Effect of solution chemistry on coagulation with hydrolyzed Al(III): Significance of sulfate ion and pH*. Water Research, 1983. **17**(2): p. 195–204.

165. Sato, T., *The thermal transformation of gelatinous aluminium hydroxide*. Zeitschrift für anorganische und allgemeine Chemie, 1972. **391**(2): p. 167–173.

166. Hwang, K.-J., Y.-T. Wang, E. Iritani, and N. Katagiri, *Effects of porous gel particle compression properties on microfiltration characteristics*. Journal of Membrane Science, 2009. **341**(1–2): p. 286–293.

167. Gamage, N.P., J.D. Rimer, and S. Chellam, *Improvements in permeate flux by aluminum electroflotation pretreatment during microfiltration of surface water*. Journal of Membrane Science, 2012. **411–412**: p. 45–53.

168. Wiesner, M.R., *Morphology of particle deposits*. Journal of Environmental Engineering-ASCE, 1999. **125**(12): p. 1124–1132.

169. Xu, W.D., S. Chellam, and D.A. Clifford, *Indirect evidence for deposit rearrangement during dead-end microfiltration of iron coagulated suspensions*. Journal of Membrane Science, 2004. **239**(2): p. 243–254.

170. Echlin, P., *Analysis of Organic and Biological Surfaces*. 1984, New York: Wiley.

171. Naumkin, A.V., A. Kraut-Vass, S.W. Gaarenstroom, and C.J. Powell, *NIST X-ray Photoelectron Spectroscopy Database*. 2012, National Institute of Standards and Technology (NIST).

172. Watts, J.F., and J. Wolstenholme, *An Introduction to Surface Analysis by XPS and AES*. 2003, Chichester, West Sussex, England: J. Wiley.

173. Chung, Y.-w., *Practical Guide to Surface Science and Spectroscopy*. 2001, San Diego, CA: Academic Press.

174. Moulder, J.F., W.F. Stickle, P.E. Sobol, and K.D. Bomben, in *Handbook of X-ray Photoelectron Spectroscopy: A Reference Book of Standard Spectra for Identification and Interpretation of XPS Data*, ed. J. Chastain and R.C. King. 1995, Eden Prairie, MN: Physical Electronics. 261.

175. Tanford, C., *The Hydrophobic Effect: Formation of Micelles and Biological Membranes*, 2d ed. 1991, Malabar, FL: Krieger.

176. Stumm, W., L. Sigg, and B. Sulzberger, *Chemistry of the Solid-Water Interface: Processes at the Mineral-Water and Particle-Water Interface in Natural Systems*. 1992, New York: Wiley.

177. Gamage, N.P., and S. Chellam, *Mechanisms of physically irreversible fouling during surface water microfiltration and mitigation by aluminum electroflotation pretreatment*. Environmental Science & Technology, 2014. **48**(2): p. 1148–1157.

178. Lee, S., B. Kwon, M. Sun, and J. Cho, *Characterizations of NOM included in NF and UF membrane permeates*. Desalination, 2005. **173**(2): p. 131–142.

179. Shon, H.K., S. Vigneswaran, I.S. Kim, J. Cho, and H.H. Ngo, *Fouling of ultrafiltration membrane by effluent organic matter: A detailed characterization using different organic fractions in wastewater*. Journal of Membrane Science, 2006. **278**(1–2): p. 232–238.

180. Song, W., V. Ravindran, B.E. Koel, and M. Pirbazari, *Nanofiltration of natural organic matter with H_2O_2/UV pretreatment: Fouling mitigation and membrane surface characterization*. Journal of Membrane Science, 2004. **241**(1): p. 143–160.

181. Tang, C.Y., Y.-N. Kwon, and J.O. Leckie, *Effect of membrane chemistry and coating layer on physiochemical properties of thin film composite polyamide RO and NF membranes*. Desalination, 2009. **242**(1–3): p. 149–167.

182. Mantsch, H.H., and D. Chapman, *Infrared Spectroscopy of Biomolecules*. 1996, New York: John Wiley & Sons, Inc. p. 2–3, 262–263, 283–285.

183. Cho, J., G. Amy, J. Pellegrino, and Y. Yoon, *Characterization of clean and natural organic matter (NOM) fouled NF and UF membranes, and foulants characterization*. Desalination, 1998. **118**(1–3): p. 101–108.

184. Her, N., G. Amy, A. Plottu-Pecheux, and Y. Yoon, *Identification of nanofiltration membrane foulants*. Water Research, 2007. **41**(17): p. 3936–47.

185. Kong, J., and S. Yu, *Fourier transform infrared spectroscopic analysis of protein secondary structures protein FTIR data analysis and band assignment*. Acta Biochimica et Biophysica Sinica, 2007. **39**(8): p. 549–559.

186. Badireddy, A.R., B.R. Korpol, S. Chellam, P.L. Gassman, M.H. Engelhard, A.S. Lea, and K.M. Rosso, *Spectroscopic characterization of extracellular polymeric substances from Escherichia coli and Serratia marcescens: Suppression using sub-inhibitory concentrations of bismuth thiols*. Biomacromolecules, 2008. **9**(11): p. 3079–89.

187. Pihlajamaki, A., P. Vaisanen, and M. Nystro, *Characterization of clean and fouled polymeric ultrafiltration membranes by Fourier transform IR spectroscopy – attenuated total reflection*. Colloids and Surfaces A: Physicochemical and Engineering Aspects, 1998. **138**(2–3): p. 323–333.

188. Stuart, B.H., *Infrared Spectroscopy: Fundamentals and Applications*. 2004, Chichester, West Sussex: John Wiley & Sons Ltd. p. 144.

189. Zhang, L., and J. Hermans, *Helix Versus a-Helix: A Molecular Dynamics Study of Conformational Preferences of Aib and Alanine*. Journal of the American Chemical Society, 1994. **116**(14): p. 11915–11921.

190. Villacorte, L.O., M.D. Kennedy, G.L. Amy, and J.C. Schippers, *The fate of transparent exopolymer particles (TEP) in integrated membrane systems: removal through pre-treatment processes and deposition on reverse osmosis membranes*. Water Research, 2009. **43**(20): p. 5039–52.

191. Van Nevel, S., T. Hennebel, K. De Beuf, G. Du Laing, W. Verstraete, and N. Boon, *Transparent exopolymer particle removal in different drinking water production centers*. Water Research, 2012. **46**(11): p. 3603–11.

192. Boussu, K., A. Belpaire, A. Volodin, C. Van Haesendonck, P. Van der Meeren, C. Vandecasteele, and B. Van der Bruggen, *Influence of membrane and colloid characteristics on fouling of nanofiltration membranes*. Journal of Membrane Science, 2007. **289**(1–2): p. 220–230.

193. Comerton, A.M., R.C. Andrews, and D.M. Bagley, *The influence of natural organic matter and cations on fouled nanofiltration membrane effective molecular weight cut-off*. Journal of Membrane Science, 2009. **327**(1–2): p. 155–163.

194. Hong, S., and M. Elimelech, *Chemical and physical aspects of natural organic matter (NOM) fouling of nanofiltration membranes*. Journal of Membrane Science, 1997. **132**(2): p. 159–181.

195. Sasson, M.B., W. Calmano, and A. Adin, *Iron-oxidation processes in an electroflocculation (electrocoagulation) cell*. Journal of Hazardous Materials, 2009. **171**(1–3): p. 704–709.

196. Lakshmanan, D., D.A. Clifford, and G. Samanta, *Ferrous and ferric ion generation during iron electrocoagulation*. Environmental Science & Technology, 2009. **43**(10): p. 3853–3859.

197. Morgan, B., and O. Lahav, *The effect of pH on the kinetics of spontaneous Fe(II) oxidation by O_2 in aqueous solution—Basic principles and a simple heuristic description*. Chemosphere, 2007. **68**(11): p. 2080–2084.

198. Stumm, W., and J.J. Morgan, *Aquatic Chemistry*. 3rd ed. 1996, New York: John Wiley & Sons.

199. Matsui, Y., T. Matsushita, S. Sakuma, T. Gojo, T. Mamiya, H. Suzuoki, and T. Inoue, *Virus inactivation in aluminum and polyaluminum coagulation*. Environmental Science & Technology, 2003. **37**(22): p. 5175–5180.

200. Liu, W.-K., M.R.W. Brown, and T.S.J. Elliott, *Mechanisms of the bactericidal activity of low amperage electric current (DC)*. Journal of Antimicrobial Chemotherapy, 1997. **39**: p. 687–695.

201. Jeong, J., J.-Y. Kim, and J. Yoon, *The role of reactive oxygen species in the electrochemical inactivation of microorganisms*. Environmental Science & Technology, 2006. **40**: p. 6117–6122.

202. Drees, K.P., M. Abbaszadegan, and R.M. Maier, *Comparative electro-chemical inactivation of bacteria and bacteriophage*. Water Research, 2003. **37**(10): p. 2291–2300.

203. Hotze, E.M., A.R. Badireddy, S. Chellam, and M.R. Wiesner, *Mechanisms of bacteriophage inactivation via singlet oxygen generation in UV illuminated fullerol suspensions*. Environmental Science & Technology, 2009. **43**(17): p. 6639–6645.

204. Tarr, M.A., and M.E. Lindsey, *Mechanistic factors affecting Fenton oxidation in natural waters*, in *Emerging Technologies in Hazardous Waste Management 8*, D.W. Tedder and F.G. Pohland, Editors. 2000, New York: Kluwer Academic/Plenum Publishers. p. 81–92.

205. Theis, T.L., and P.C. Singer, *Complexation of iron(II) by organic matter and its effect on iron(II) oxygenation*. Environmental Science and Technology, 1974. **8**(6): p. 569–573.

206. Brady-Estévez, A.S., T.H. Nguyen, L. Gutierrez, and M. Elimelech, *Impact of solution chemistry on viral removal by a single-walled carbon nanotube filter*. Water Research, 2010. **44**(13): p. 3773–3780.

207. Langlet, J., F. Gaboriaud, J.F.L. Duval, and C. Gantzer, *Aggregation and surface properties of F-specific RNA phages: Implication for membrane filtration processes*. Water Research, 2008. **42**(10–11): p. 2769–2777.

208. Choi, K.Y.-j., and B.A. Dempsey, *In-line coagulation with low-pressure membrane filtration*. Water Research, 2004. **38**(19): p. 4271–4281.

209. Bellona, C., M. Marts, and J.E. Drewes, *The effect of organic membrane fouling on the properties and rejection characteristics of nanofiltration membranes*. Separation and Purification Technology, 2010. **74**(1): p. 44–54.

210. Kobya, M., F. Ulu, U. Gebologlu, E. Demirbas, and M.S. Oncel, *Treatment of potable water containing low concentration of arsenic with electro-coagulation: Different connection modes and Fe-Al electrodes*. Separation and Purification Technology, 2011. **77**(3): p. 283–293.

211. Staehelin, J., and J. Hoigne, *Decomposition of ozone in water in the presence of organic solutes acting as promoters and inhibitors of radical chain reactions*. Environmental Science & Technology, 1985. **19**(12): p. 1206–1213.

212. Lindsey, M.E., and M.A. Tarr, I*nhibited hydroxyl radical degradation of aromatic hydrocarbons in the presence of dissolved fulvic acid*. Water Research, 2000. **34**(8): p. 2385–2389.

213. Singer, P.C., and D.A. Reckhow, *Chemical oxidation*, in *Water Quality and Treatment: A Handbook of Community Water Supplies*, R.D. Letterman, Editor. 1999, New York: McGraw Hill. p. 12.1–12.51.

214. Kim, J.Y., C. Lee, D.L. Sedlak, J. Yoon, and K.L. Nelson, *Inactivation of MS2 coliphage by Fenton's reagent*. Water Research, 2010. **44**: p. 2647–2653.

215. Tanneru, C.T., and S. Chellam, *Mechanisms of virus control during iron electrocoagulation-microfiltration of surface water*. Water Research, 2012. **46**: p. 2111–2120.

216. Matsushita, T., N. Shirasaki, Y. Matsui, and K. Ohno, *Virus inactivation during coagulation with aluminum coagulants*. Chemosphere, 2011. **85**(4): p. 571–576.

217. Matsui, Y., T. Matsushita, S. Sakuma, T. Gojo, T. Mamiya, H. Suzuoki, and T. Inoue, *Virus inactivation in aluminum and polyaluminum coagulation*. Environmental Science and Technology, 2003. 37: p. 5175–5180.

218. Liang, W., J. Qu, L. Chen, H. Liu, and P. Lei, *Inactivation of Microcystis aeruginosa by continuous electrochemical cycling process in tube using Ti/RuO_2 electrodes*. Environmental Science & Technology, 2005. **39**: p. 4633–4639.

219. Baes, C.F., and R.E. Mesmer, *The Hydrolysis of Cations*. 1976, New York: John Wiley & Sons. 489.

220. Shirasaki, N., T. Matsushita, Y. Matsui, and K. Ohno, *Effects of reversible and irreversible membrane fouling on virus removal by a coagulation-microfiltration system*. Journal of Water Supply Research and Technology-Aqua, 2008. **57**(7): p. 501–506.

221. Clesceri, L.S., A.E. Greenberg, and A.D. Eaton, eds. *Standard Methods for the Examination of Water and Wastewater*, 20th ed. 1998, Washington: APHA, AWWA, and WEF.

222. Engel, A., and D.J. Müller, *Observing single biomolecules at work with the atomic force microscope*. Nature Structural Biology, 2000. **7**(9): p. 715–718.

223. Oroudjev, E., J. Soares, S. Arcidiacono, J.B. Thompson, S.A. Fossey, and H.G. Hansma, *Segmented nanofibers of spider dragline silk: Atomic force microscopy and single-molecule force spectroscopy*. Proceedings of the National Academy of Sciences, 2002. **99**(Suppl 2): p. 6460–6465.

224. Chrisey, L.A., R.J. Colton, and G.U. Lee, *Direct measurement of the forces between complementary strands of DNA*. Science, 1994. **266**: p. 771–773.

225. Gutierrez, L., and T.H. Nguyen, *Interactions between Rotavirus and Suwannee River Organic Matter: Aggregation, deposition, and adhesion force measurement*. Environmental Science & Technology, 2012. **46**(16): p. 8705–8713.

226. Dempsey, B.A., R.M. Ganho, and C.R. O'Melia, *The coagulation of humic substances by means of aluminum salts*. Journal of the American Water Works Association, 1984. **76**(4): p. 141–150.

227. White, M.C., J.D. Thompson, G.W. Harrington, and P.C. Singer, *Evaluating criteria for enhanced coagulation compliance*. Journal of the American Water Works Association, 1997. **89**(5): p. 64–77.

228. Lee, S.-Y., J.S. Lim, J.N. Culver, and M.T. Harris, *Coagulation of tobacco mosaic virus in alcohol-water-LiCl solutions*. Journal of Colloid and Interface Science, 2008. **324**(1–2): p. 92–98.

229. Cañizares, P., M. Carmona, J. Lobato, F. Martínez, and M.A. Rodrigo, *Electrodissolution of aluminum electrodes in electrocoagulation processes*. Industrial & Engineering Chemistry Research, 2005. **44**(12): p. 4178–4185.

230. Gao, S., J. Yang, J. Tian, F. Ma, G. Tu, and M. Du, *Electro-coagulation-flotation process for algae removal*. Journal of Hazardous Materials, 2010. **177**(1–3): p. 336–343.

231. Braghetta, A., J.G. Jacangelo, S. Chellam, M.L. Hotaling, and B.A. Utne, *DAF pretreatment: Its effect on MF Performance*. Journal of the American Water Works Association, 1997. **89**(10): p. 90–101.

232. Lahoussine-Turcaud, V., M.R. Wiesner, and J.Y. Bottero, *Fouling in tangential flow ultrafiltration: The effect of colloid size and coagulation pretreatment*. Journal of Membrane Science, 1990. **52**: p. 173–190.

233. Yamamura, H., K. Kimura, T. Okajima, H. Tokumoto, and Y. Watanabe, *Affinity of functional groups for membrane surfaces: Implications for physically irreversible fouling*. Environmental Science & Technology, 2008. **42**(14): p. 5310–5315.

234. Contreras, A.E., Z. Steiner, J. Miao, R. Kasher, and Q. Li, *Studying the role of common membrane surface functionalities on adsorption and cleaning of organic foulants using QCM-D*. Environmental Science & Technology, 2011. **45**(15): p. 6309–6315.

235. Jucker, C., and M.M. Clark, *Adsorption of aquatic humic substances on hydrophobic ultrafiltration membranes*. Journal of Membrane Science, 1994. **97**: p. 37–52.

236. Chen, J., B. Gu, E.J. LeBoeuf, H. Pan, and S. Dai, S*pectroscopic characterization of the structural and functional properties of natural organic matter fractions*. Chemosphere, 2002. **48**(1): p. 59–68.

237. Tang, C.Y., Q.S. Fu, C.S. Criddle, and J.O. Leckie, *Effect of flux (transmembrane pressure) and membrane properties on fouling and rejection of reverse osmosis and nanofiltration membranes treating perfluorooctane sulfonate containing wastewater*. Environmental Science & Technology, 2007. 41(6): p. 2008–2014.

238. Vrijenhoek, E.M., S. Hong, and M. Elimelech, *Influence of membrane surface properties on initial rate of colloidal fouling of reverse osmosis and nanofiltration membranes*. Journal of Membrane Science, 2001. **188**(1): p. 115–128.

239. Urban, M.W., *Vibrational Spectroscopy of Molecules and Macromolecules on Surfaces*. 1993, New York: Wiley. 384.

240. Little, L.H., *Infrared Spectra of Adsorbed Species*. 1966, London, New York: Academic Press. xii, 428 p.

241. Schmidt, P., J. Dybal, and M. Trchová, *Investigations of the hydrophobic and hydrophilic interactions in polymer–water systems by ATR FTIR and Raman spectroscopy*. Vibrational Spectroscopy, 2006. **42**(2): p. 278–283.

242. Nyquist, R.A., *Interpreting infrared, Raman, and nuclear magnetic resonance spectra*, v. 1. 2001, San Diego: Academic Press.

243. Tambo, N., and Y. Watanabe, *Physical characteristics of flocs-1. The floc density-function and aluminum floc*. Water Research, 1979. **13**(5): p. 409–419.

244. Davis, C.C., and M. Edwards, *Coagulation with hydrolyzing metal salts: mechanisms and water quality impacts*. Critical Reviews in Environmental Science and Technology, 2014. **44**(4): p. 303–347.

245. Singer, P.C., *Control of disinfection by-products in drinking water*. Journal of Environmental Engineering-ASCE, 1994. **120**(4): p. 727–744.

246. Aleman, C., J.J. Navas, and S. Munoz-Guerra, *Study of the amide···ester hydrogen bond in small molecules and its influence on the conformation of polypeptides and related polymers*. The Journal of Physical Chemistry, 1995. **99**(49): p. 17653–17661.

247. Grabowski, S.J., ed., *Hydrogen Bonding—New Insights* (*Challenges and Advances in Computational Chemistry and Physics*, v. 3). 2006, Netherlands: Springer.

248. Karshikoff, A., *Non-covalent interactions in proteins*. 2006, London, Singapore: Imperial College Press; World Scientific [distributor]. xii, 333 p.

249. Erbil, H.Y., *Surface Chemistry of Solid and Liquid Interfaces*. 2006, Oxford, UK: Blackwell Pub.

250. Tarabara, V.V., I. Koyuncu, and M.R. Wiesner, *Effect of hydrodynamics and solution ionic strength on permeate flux in cross-flow filtration: Direct experimental observation of filter cake cross-sections*. Journal of Membrane Science, 2004. **241**(1): p. 65–78.

251. Cabane, B., M. Meireles, and P. Aimar, *Cake collapse in frontal filtration of colloidal aggregates: Mechanisms and consequences*. Desalination, 2002. **146**(1–3): p. 155–161.